Institute for Computational and Applied Mechanics (ICAM)

A STUDY OF FLOW SEPARATION IN TRANSONIC FLOW USING INVISCID AND VISCOUS CFD SCHEMES

By

J.A. Rhodes, S.N. Tiwari, and E. von Lavante

OCT 2 8

ODU/ICAM Report 88-102
April 1988

Old Dominion University
Norfolk, Virginia 23508-8546

OLD DOMINION UNIVERSITY

College of Engineering
Department of Mechanical Engineering and Mechanics
Norfolk, Virginia 23529-0247
804-683-3720

August 8, 1988

Dr. Samuel E. Massenberg
University Affairs Officer
Mail Stop 105 A
NASA Langley Research Center
Hampton, VA 23665-5225

Dear Dr. Massenberg:

Reference NASA Grant NAG-1-363, Institute for
Computational and Applied Mechanics (ICAM)

Enclosed is a report entitled, "A Study of Flow Separation in
Transonic Flow Using Inviscid and Viscous CFD Schemes" for the
research work performed during the period June 1983 to December 1987
under the ICAM program.

Copies of this report are being forwarded to appropriate NASA and ODU
advisors. If you have any questions concerning this report, please
contact me. Thank you.

Sincerely yours,
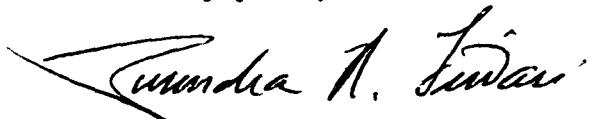
Surendra N. Tiwari
Eminent Professor and ICAM Director

SNT/rbp

Distr.
NASA Sci & Tech Info Facility, 2 copies.

Institute for Computational and Applied Mechanics (ICAM)

A STUDY OF FLOW SEPARATION IN TRANSONIC FLOW USING INVISCID AND VISCOUS CFD SCHEMES

By

J.A. Rhodes, S.N. Tiwari, and E. von Lavante

N88-26618

A STUDY OF FLOW SEPARATION IN TRANSONIC FLOW
USING INVISCID AND VISCOUS CFD SCHEMES

By

J. A. Rhodes[1], S. N. Tiwari[2] and E. von Lavante[3]
Old Dominion University, Norfolk, Virginia 23529-0247

SUMMARY

A comparison of flow separation in transonic flows is made using various computational schemes which solve the Euler and the Navier-Stokes equations of fluid mechanics. The flows examined are computed using several simple two-dimensional configurations including a backward facing step and a bump in a channel. Comparison of the results obtained using shock fitting and flux vector splitting methods are presented and the results obtained using the Euler codes are compared to results on the same configurations using a code which solves the Navier-Stokes equations.

---

[1]Graduate Research Assistant (ICAM Fellow), Dept. of Mechanical Engineering and Mechanics; present affiliation, Senior Engineer, Dept. of Propulsion and Thermodynamics, McDonnell Aircraft Company, St. Louis, MO 63166.

[2]Eminent Professor, Dept. of Mechanical Engineering and Mechanics; Director of ICAM.

[3]Associate Professor of Mechanical Engineering and Mechanics.

ACKNOWLEGEMENTS

TABLE OF CONTENTS

LIST OF TABLES

LIST OF FIGURES

LIST OF SYMBOLS

A	Jacobian matrix
a	speed of sound, nondimensionalized by a_0
B	Jacobian matrix
E	Total energy
e	total energy, nondimensionalized by $\rho_0 \, a_0^2$
F	flux vector in x or ξ direction
G	flux vector in y or η direction
h	enthalpy, nondimensionalized by $\rho_0 \, a_0^2$
I	identify matrix
i	internal energy, nondimensionalized by a_0^2
J	Jacobian of transformation
k	coefficient of thermal conductivity
M, N	eigenvector matrices corresponding to A and B matrices
P	logarithm of p
p	pressure, nondimensionalized by $\rho_0 \, a_0^2$
Q	vector of conserved quantities
q	mass flux
R	gas constant
S	entropy
T	temperature
t	time
U, V	contravarient velocity components in ξ and η directions

u, v	Cartesian velocity components in x and y directions
x, y	Cartesian coordinates
z	$x + iy$, complex physical plane

Greek symbols

γ	ratio of specific heats
ξ, η	general coordinates
κ	von Karman's constant
λ, Ω	eigenvalues
ρ	density nondimensionalized by ρ_0
μ	coefficient of molecular viscosity
σ_{ij}	shear stress tensor
τ_{ij}	deviatoric stress tensor
ω	vorticity

Subscripts

x, y	indicates differentiation with respect to Cartesian coordinates
ξ, η	indicates differentiation with respect to general coordinates
s	indicates source term, also variable at shock
0	indicates stagnation conditions
∞	indicates conditions at infinity

Superscripts

n	time level
$\pm$	indicates direction of characteristic eigenvalues or differentiation

Chapter 1

INTRODUCTION

Although much progress has been made in the field of computational fluid dynamics (CFD), the computation of transonic flows containing shock waves and of flows exhibiting separation is still a challenge. The most commonly used methods to compute such flows solve either the time-dependent Euler or Navier-Stokes equations on a fixed grid. The Euler equations allow for rotational flows but neglect viscous effects, whereas the Navier-Stokes equations take into account viscous effects. Both sets of equations, when expressed in integral form, are correct even when discontinuities in the flow field are present. The compressible potential equation, which has been used extensively for aerodynamic prediction, does not allow for rotational flows and viscous effects and is therefore not considered in this study. However, when shock waves are weak and flow separation is not expected, the potential model may provide a good approximation. Furthermore, when coupled with boundary layer equations, viscous-inviscid methods have been successfully used to compute flows with separation.

The development of CFD and, more specifically, methods to solve compressible flow problems extends back into the 1950's and a complete history is beyond the scope of this introduction. The mathematical theory of these numerical approximations has been developing rapidly as has been the mathematical theory of hyperbolic conservation laws and

1

shock waves. The 1948 book by Courant and Friedrichs [1]* and the 1973 SIAM publication by Lax [2] were important contributions to the literature which provide much of the basic theory. The 1967 text by Richtmeyer and Morton [3] is now considered a classic text on the application of difference methods to initial value problems. More recently, the books by Smoller [4] and Majda [5] provide up-to-date exposition of the mathematical theory. While there have been many books on CFD published, the recent text by Anderson, Pletcher and Tannehill [6] is one of the most popular. Finally, the 1986 survey article by Roe contains an excellent discussion of the development and fairly recent state of affairs in numerical schemes for the Euler equations [7].

Early schemes were relatively simple explicit methods such as the Lax-Wendroff scheme [8] and its derivative, the two-step MacCormack Scheme [9]. These schemes are essentially central-difference schemes and have the undesirable property of being oscillatory near shocks. In order to stabilize them, artificial dissipation terms must be added which tend to smear out the discontinuities over several mesh intervals. Early upwind schemes include the CIR (Courant-Isaacson-Rees [10]) and the Godunov [11] methods. These schemes are both first order accurate and are not used today but were important advances and prepared the way for more advanced schemes. Upwind schemes are purported to be more physically correct since they are based on the way characteristic information propagates. They are also more stable near shocks and it has been shown that upwind difference schemes are the equivalent of

---

*Numbers in brackets indicate references.

central difference schemes plus artificial dissipation [12]. The finite volume schemes popularized by Jameson [13] are also explicit central difference schemes which must include dissipative terms in order to stabilize the scheme and avoid odd-even decoupling of the mesh points.

All of the explicit schemes are restricted to rather low CFL (Courant-Friedrichs-Lewy) numbers which restricts the maximum allowable time step they can take. This means that the number of iterations required to achieve a given level of convergence is larger than would be the case if the schemes could run at a higher CFL number. To overcome this limitation, implicit schemes were developed. There have been many such schemes developed of which one of the most significant is the Beam-Warming approximate factorization algorithm [14]. This scheme was a major advance and many later schemes were, at least in part, based on it. Since this scheme solves the governing equations in conservation form, the converged solutions satisfy the Rankine-Hugoniot jump relations if shocks are present. However, as is the case with all of the schemes discussed up to now, artificial dissipation must be present to stabilize the scheme near discontinuities.

Since the numerical algorithms typically begin with an initial guess and then iterate towards a converged solution which must satisfy the specified boundary conditions, the problems to which they are applied are mathematically described as initial-boundary value problems. The discontinuities that are computed and resolved arise during the course of the computations and the location of these discontinuities is generally not known beforehand. Thus the schemes are frequently described as "shock capturing." Another approach that has proven successful is referred to a "shock fitting." In this approach,

the location of the discontinuity is at least approximately known beforehand and the appropriate mathematical relations are used to relate the flow conditions an each side of the discontinuity, thus providing a much better resolution of the discontinuity. In this study, both shock capturing and shock fitting methods are used and the results are compared.

Separated flow has, in the past, almost always been associated with boundary layer separation and thus is usually regarded as a viscous effect. Several years ago, however, Salas [15] and others noticed that inviscid compressible flow past a circular cylinder computed using the Euler equations can separate when the free stream Mach number is greater than 0.4. Salas pointed out that earlier analytical investigations by Fraenkel [16] proved that exact solutions of the incompressible Euler equations, for flow past a circular cylinder, can show separation bubbles in front of and behind the cylinder, the size of which are controlled by the free stream vorticity. Salas also deduced that flow through a curved shock could produce sufficient vorticity to cause the flow to separate in some cases. He raised several questions concerning the validity of the computed solutions. First, are the converged solutions unique? Second, what is the relation between the computed Euler solutions to the solution of the Navier-Stokes equations, especially in the limit as the Reynolds number goes to infinity?

Kumar and Salas later compared Euler and Navier-Stokes solutions for supersonic shear flow past a circular cylinder [17]. The impinging supersonic flow contained vorticity and the separation occurred along a symmetry line ahead of the cylinder. The investigators found that while the overall size of the separation zone computed using both sets of

equations was similar, the internal structure was quite different which they attributed to viscous effects. The inviscid solution showed only one vortex, whereas the viscous solution showed an inner and an outer vortex. As the Reynolds number was increased, the inner vortex decreased in size and the Navier-Stokes solution became similar to the Euler solution.

Barton and Pulliam also compared Euler and Navier-Stokes solutions for flow past a NACA 0012 airfoil at high angles of attack [18]. They used an implicit approximate factorization scheme which solved either the Euler equations or the Navier-Stokes equations in thin layer form with an algebraic Baldwin-Lomax turbulence model. The authors first describe the inviscid results for $M_\infty = 0.25$ and 0.4 on a coarse 249 x 41 grid and a fine 249 x 67 grid with an $\alpha = 15^0$. At $M_\infty = 0.25$ on the coarse grid, there was no leading edge shock but the flow separated and an unsteady oscillatory behavior was observed in the solution. On the fine grid, there was a shock but no flow separation and the solution converged to a steady state. At $M_\infty = 0.4$, there was a leading edge shock and the solution exhibited an oscillatory separated flow which did not depend on the grid. Viscous and inviscid calculations were carried out for $M_\infty = 0.301$ and $\alpha = 13.5^0$. The Reynolds number in the viscous calculation was 3.91×10^6. While both the inviscid and viscous calculations yielded a separated solution, in the inviscid case, no steady state solution was reached and an oscillatory behavior was noted, whereas the computations using the viscous equations converged to a steady state. The authors concluded that in this case the Euler solution was not a good approximation to the Navier-Stokes solution. They also concluded that while in some cases the separated flow computed

was the correct solution to the inviscid equations, in other cases numerical errors due to the use of a very coarse mesh caused the flow to separate and the solution was not valid.

Separated flow on the leeside of conical delta wings at high angles of attack has been the subject of several investigations. Marconi studied supersonic conical separation using a the lambda scheme with shock fitting to solve the Euler equations [19]. It was assumed that the flow is invariant in the axial direction and therefore the three-dimensonal equations can be solved using a two-dimensional grid. A shock wave emanating from the leeside of the body produced a significant vorticity gradient which resulted in flow separation. The separated flow spirals up and does not form a closed recirculation eddy as in the case of flow past a cylinder. Grid refinement was done without any significant change in the results.

Newsome and Thomas computed and compared Euler and Navier-Stokes solutions for a conical delta wing at a M_∞ equal to 2.0 and α equal to 10° [20]. The conical assumption was also used allowing the calculations to be done on two-dimensional grids. The viscous solutions were obtained using both a central difference scheme based on MacCormack's explicit unsplit algorithm and also a flux vector splitting scheme developed by Thomas. The viscous solutions obtained with both schemes on a 151 x 65 grid agreed closely and showed a separated vortical flow on the leeside of the wing with a primary vortex due to leading edge separation and a secondary crossflow separation vortex.

The Euler solutions were obtained using the same schemes after dropping the viscous terms and the surface no-slip boundary condition.

Two grids, a coarse 75 x 55 grid and the same viscous grid as before, were used. On the coarse grid, the MacCormack scheme solution showed a separation vortex similar to the viscous results. Entropy was produced at the leading edge although there was only a small shock evident. The upwind flux vector splitting scheme produced solutions with no such separation on the coarse grid. The authors concluded that the flow separation obtained on the coarse grid was due to the artificial damping added to the central difference scheme so that the results were considered incorrect. Using the fine grid, both schemes produced similar results and the solutions showed a small vortex downstream of the crossflow shock.

Chakravarthy did further calculations on the same problem using a TVD scheme to study the issue of inviscid separation [21]. He concluded that one possible explanation for the different results that Newsome and Thomas had obtained was the use of spatially varying time steps. He stated that this practice may result in unphysical transients which does not occur when a global time step is used.

However, Kandil and Chuang performed a careful investigation of supersonic vortex dominated flows about sharp and round-edge conical delta wings and concluded that for the round-edge wings the damping coefficients used in the finite-volume code controls whether attached or separated solutions are obtained [22]. In addition, their computations indicated that the solutions obtained did not depend on whether global or local time stepping was used, in contrast to the hypothesis of Chakravarthy.

In view of the findings of the various investigations just discussed, it is clear that numerical solutions of the Euler equations which exhibit separated flow must be carefully evaluated to determine whether or not the results are realistic. This investigation therefore is an attempt to provide further insight into the inviscid separation phenomenon and specifically an attempt is made to relate the inviscid separation case to the viscous case. Various codes were used in the course of this study and the general investigation procedure is described in the next chapter.

Chapter 2

PHYSICAL MODELS AND GRID GENERATION

In this chapter, investigation procedures for different physical systems are presented and various techniques of grid generation are discussed.

2.1   Investigation Procedure

Several simple two-dimensional configurations were chosen which could be used to test the various schemes used to solve the Euler and Navier-Stokes equations for transonic flow. The first configuration is flow past a rearward facing step. It is known from experiment that incompressible flow past such a step separates at a Reynolds number, based on step height, less than 500 to form one or more recirculation vortices downstream of the step [23, 24]. The incompressible flow case has been computed numerically by several investigators and the results are contained in the proceedings of a recent GAMM workshop [25]. The compressible case for $M_\infty = 0.5$ has been computed by Schmidt and Jameson using the Euler equations and a finite volume scheme [26].

The step used in this investigation differs from these cases in that a conformal transformation was used to generate the grid. This resulted in the requirement that in order to avoid singularities in the tranformation metrics, a sharp corner had to be avoided and instead, a rounded expansion corner was used. The conformal transformation was

used to control the location of the physical boundaries and the resulting suddenness of the expansion. It was found that for very gradual expansions the flow in most cases did not separate. Whereas, when the expansion corner was brought closer to a sharp corner, separation occurred. An example of this configuration is shown in Fig. 2.1a.

A second conformal transformation was used to produce a configuration which could be taken to represent a bump in a channel as shown in Fig. 2.1b. In the limit, the "bump" would become a semi-circle as will be discussed further in the next section on grid generation. The third configuration chosen for study is a circular arc inside a channel as shown in Fig. 2.1c. This geometry was chosen as other investigators have used it and it was thought desirable to be able to compare the results obtained in this investigation with the results obtained by others. Finally, a NACA 0012 airfoil with $\alpha = 0^0$ as shown in Fig. 2.1d was chosen as an external flow problem.

Three computational techniques were used to solve the Euler equations. The first is a Gabutti shock capturing scheme which is a variation of the lamda scheme developed earlier by Moretti [27, 28]. Computer codes applied by the writer to all four test problem were executed on the NASA Langley computer system; some of these codes were vectorized to speed up the execution time.

The second method is a shock fitting version of the first method. In this method, the jump conditions through the shock are explicitly enforced and the grid is forced to adapt to the moving shock. A vectorized version was developed for the rearward facing step and conformal bump in channel problems and used to perform grid refinement

(a) Backward Facing Step   (b) Bump in Channel
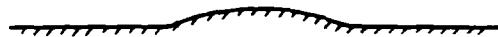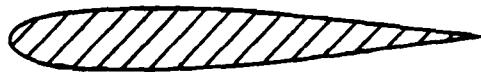
(c) Circular Arc   (d) NACA 0012 Airfoil

Fig. 2.1 Configurations Used for Study.

studies. The third Euler solver used was an implicit flux vector splitting scheme which was originally developed by von Lavante with modifications subsequently made by the writer [47]. These schemes are described in subsequent chapters.

The full Navier-Stokes equations were solved using an implicit upwind approximate factorization scheme developed by Rumsey [29]. The computer code is fully vectorized and has been shown to give accurate solutions for unsteady flow cases. The code was applied to test problems one and two as these cases showed flow separation using the inviscid equations. Test problems three and four showed no such separation and hence the viscous code was not used.

2.2 Grid Generation

Problems in fluid dynamics are classified as field problems since the solutions are represented by variables such as density, pressure, velocity, etc. which are functions of one or more spatial dimensions as well as of time. Since computers have finite memories, they can only solve the governing equations at a finite number of representative spatial locations. The equations must therefore be discretized and solved numerically at these locations. The purpose of grid generation is therefore to distribute the points at which the solution is desired over the spatial domain in some "optimum" sense to facilitate the solution.

Usually this involves a transformation of coordinates from cartesian to a body fitted coordinate system. Thus the original (x,y) cartesian coordinates are replaced by curvilinear (ξ,η) coordinates which wrap around the configuration to be studied. The main advantage

in doing this is that it is usually possible to take advantage of computer array data structures which is generally not the case if cartesian coordinates are used. However, the governing equations must also be transformed and additional computer memory is often required for the storage of metric terms and Jacobians. The transformation must be one-to-one and the new curvilinear coordinates are frequently assigned integer values such $\xi = 0, 1, 2, \ldots, I_{max}$.

Various grid generation techniques have been devised and the ones which were used in this investigation include conformal mapping, algebraic, and elliptic methods. These will be discussed in relation to the specific grid generation requirements of each test problem.

2.2.1 Conformal Mapping Technique

For the rearward facing step test problem, the transformation from the computational plane to the physical plane is shown in Fig. 2.2 and the transformation equation is [30]

$$z = \frac{1}{\pi} [(\zeta^2 - 1)^{1/2} + \ln (\zeta + (\zeta^2 - 1)^{1/2})] \qquad (2.1)$$

where

$$\zeta = \xi + i\eta$$

$$z = x + iy .$$

The metrics x_ξ, x_η, y_ξ, y_η are easily obtained from Eq. (2.1) as follows. First $dz/d\zeta$ is found as

$$dz/d\zeta = \frac{1}{\pi} [(\zeta + 1)/(\zeta - 1)]^{1/2} \qquad (2.2)$$

Then x_ξ and y_ξ are found from

$$(x + iy)_\xi = \frac{dz}{d\xi} = \frac{dz}{d\zeta}\frac{d\zeta}{d\xi} = \frac{1}{\pi}\frac{\zeta+1}{\zeta-1} \tag{2.3}$$

Finally from the Cauchy-Riemann equations, we have

$$x_\xi = y_\eta \qquad \text{and} \qquad y_\xi = -x_\eta$$

The Jacobian of the transformation is given by

$$J = \frac{\partial(\xi,\eta)}{\partial(x,y)} = \xi_x\,\eta_y - \eta_x\,\xi_y \tag{2.4}$$

$$\xi_x = J\,y_\eta$$

$$\xi_y = -J\,x_\eta$$

$$\eta_x = -J\,y_\xi$$

$$\eta_y = J\,x_\xi$$

For the conformal bump test problem, the transformation is shown in Fig. 2.3 and the transformation equation is [30]

$$\zeta = z + \frac{1}{z}. \tag{2.5}$$

Equation (2.4) can be solved for z in terms of ζ and the result is

$$z = \frac{1}{2}\left[\zeta + (\zeta^2 - 4)^{1/2}\right] \tag{2.6}$$

The metric terms are then found from

$$\frac{dz}{d\zeta} = \frac{1}{2}\left[1 + \zeta/(\zeta^2 - 4)^{1/2}\right]$$
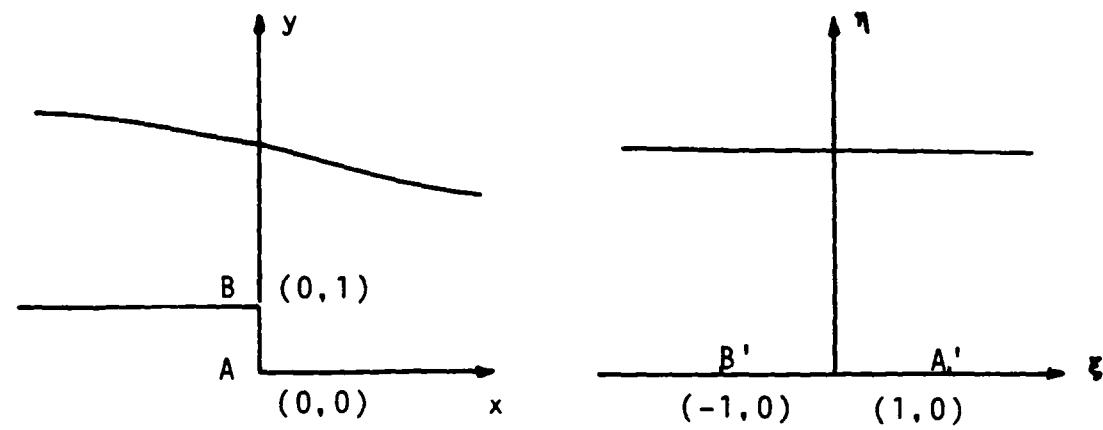
Fig. 2.2 Transformation for Backward Facing Step
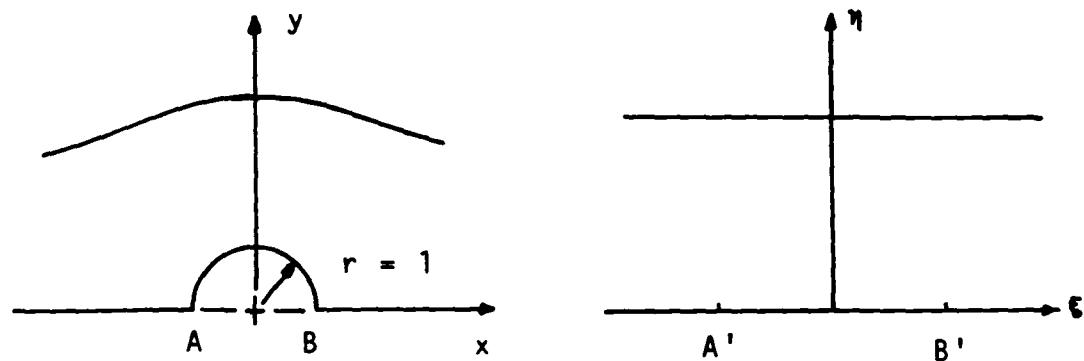
Fig. 2.3 Transformation for Bump in Channel.

For the circular arc test problem, the conformal transformation is a degenerate case of a Karman-Trefftz airfoil [31]. The transformation is shown in Fig. 2.4 and is

where

$$\frac{z-1}{z+1} = \left[\frac{(\zeta-2) + (\zeta^2-4)^{1/2}}{(\zeta+2) + (\zeta^2-4)^{1/2}}\right]^n \tag{2.7}$$

$$n = 2\left(1 - \frac{\alpha}{\pi}\right) \tag{2.8}$$

$$\alpha = 2\tan^{-1}(t)$$

and t is the thickness of the airfoil. The boundaries of the computational and physical domains are specified according to lines of constant ξ and η. The distribution of points along the boundaries was specified using simple polynomial and exponential stretching functions. In the ξ direction, a third degree polynomial was found to be sufficient:

$$\xi = \xi_0 + (\xi_1 - \xi_0)(a_1 X + a_2 X^2 + a_3 X^3) \tag{2.9}$$

where ξ_0 and ξ_1 are the minimum and maximum values of ξ respectively, and a_1, a_2, and a_3 are coefficients which are chosen to satisfy

$$X = 0 \quad \text{at} \quad \xi = \xi_0$$

$$X = IM-1 \quad \text{at} \quad \xi = \xi_1$$

$$X = IS \quad \text{at} \quad \xi = \xi_s$$

$$d\xi/dX = a_1(\xi_1 - \xi_0) \quad \text{at} \quad X = 0$$

where IM is the number of points in the ξ direction and IS is chosen to be X at $\xi = \xi_s$. The variable X becomes the new computational coordinate in the ξ direction.

In the η coordinate direction, either a second order polynomial similar to Eq. (2.9) or an exponential stretching function

$$\eta = \eta_0 + (\eta_1 - \eta_0) \frac{\exp(ks) - 1}{\exp(k) - 1} \qquad (2.10)$$

was used where η_0 and η_1 are the minimum and maximum values of η, k is a stretching coefficient, and s is given by

$$s = Y/(JM - 1) . \qquad (2.11)$$

Y is the new computational coordinate in the η direction and JM is the number of points in the η direction. The polynomial stretching in the η direction was used to generate grids used in the inviscid calculations and the exponential stretching was used to generate grids for the viscous calculations. The coefficient k was calculated using an iterative Newton routine to satisfy a prespecified $d\eta/dY$ at $\eta = 0$ given by

$$\frac{d\eta}{dY} = \frac{(\eta_1 - \eta_0)}{JM - 1} \frac{k \exp(ks)}{\exp(k) - 1} \qquad (2.12)$$

2.2.2 Algebraic Grid Generation

Bilinear interpolation [32] was used to develop an alternate non-conformal grid for the circular arc test problem and the two-boundary technique of Smith [33] was used to develop the grid for the NACA 0012 test problem. Both techniques require that the boundaries be initially specified by a distribution of points. Elliptic smoothing, as described in Sec. 2.2.3, was used to produce the final grids in both cases.

The general coordinates ξ and η along the boundaries of the circular arc was related to the arc length along the boundaries by

simple polynomial and exponential-stretching functions similar to those given in Sec. 2.2.1. The grid was made symmetric about a line passing normal to and through the top of the circular arc and the stretching function was made to satisfy the requirement that one of the lines of constant ξ begin at the corner of the arc and the straight lower boundary.

Once the (x,y) locations of the boundary points have been established, bilinear interpolation can be used to locate the interior points. For example, the x coordinate of the interior points is given by

$$x(\xi,\eta) = (1 - r) x(0,\eta) + r x(1,\eta)$$

$$+ (1 - s) x(\xi,0) + s x(\xi,1)$$

$$- (1 - r) [(1 - s) x(0,0) + s x(0,1)]$$

$$- r [(1 - s) x(1,0) + s x(1,1)] \tag{2.13}$$

where ξ, ζ, r and s all vary between 0 and 1, and r and s are normalized arc lengths weighted by their relative proximities to the top and bottom boundaries (in the case of r) and to the left and right side boundaries (in the case of s). A similar equation is used to get the y coordinates of the interior points. Note that this method does not enforce orthogonality along the boundaries. However, this is later achieved when the elliptic technique is employed in the smoothing operation.

The computational region for the NACA 0012 airfoil was designed for a "C" type grid for half the airfoil only as shown in Fig. 2.5. The airfoil surface is given by the following equation [34].
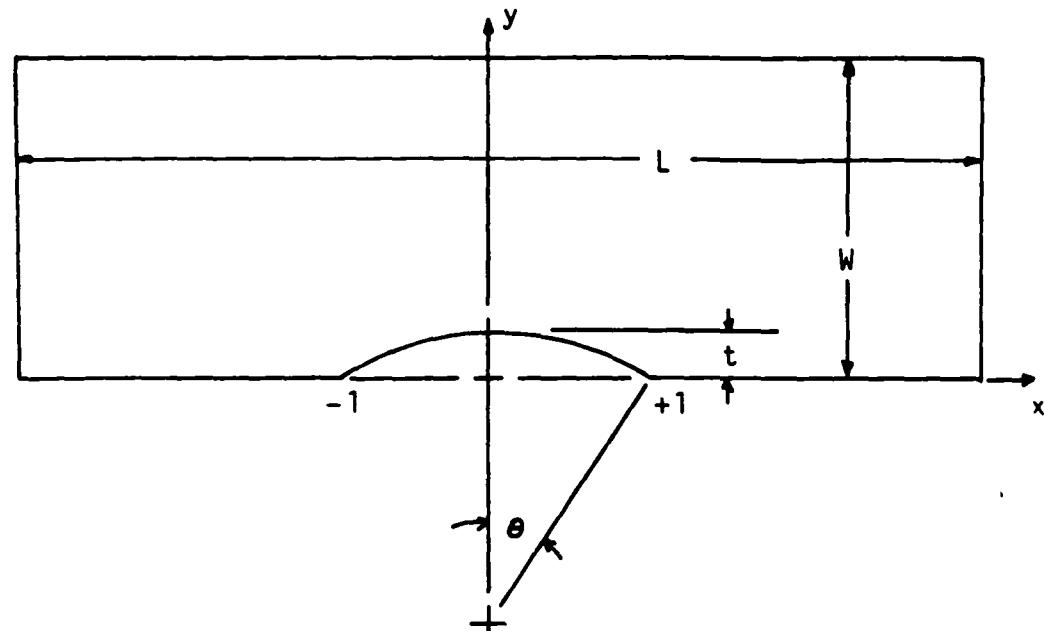
Fig. 2.4 Circular Arc Computational Domain
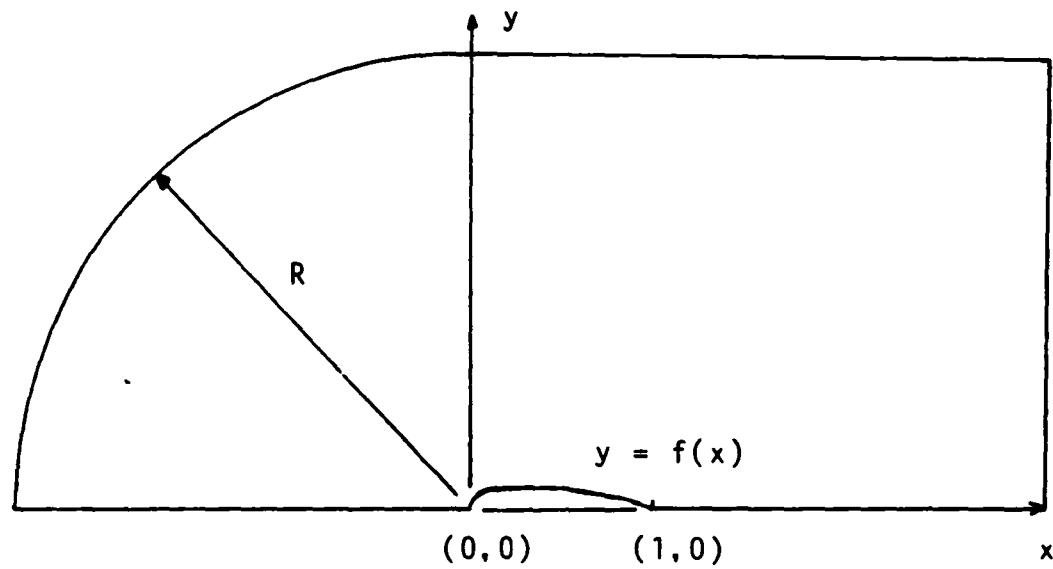
Fig. 2.5 NACA 0012 Computational Domain.

$$y = 0.6 \left[.2969\ x^{1/2} - .126\ x - .3516\ x^2 \right.$$

$$\left. + .2843\ x^3 - .1015\ x^4 \right] \tag{2.14}$$

This equation does not give $y = 0$ at $x = 1$ and it was therefore modified slightly and put into nested form to give $y = 0$ at $x = 1$ as follows

$$y = .1781\ x^{1/2} - x\ [.0756 + x\ \{.2110 - x\ (.1706$$

$$- .0621\ x)\}] \tag{2.15}$$

The points on the boundary were distributed first from A to B usihg a fifth order polynomial

$$r = a_1\ \xi + a_2\ \xi^3 + a_3\ \xi^4 + a_4\ \xi^5 \tag{2.16}$$

where r is the arc length and ξ the computational coordinate and a_1, a_2, a_3, and a_4 are found after specifying the first derivative $dr/d\xi$ at A and B, setting $d^2r/d\xi^2 = 0$ at B, and requiring r to be equal to the total arc length from A to B at a specified value of ξ. This leads to a system of four equations in four unknowns which can be easily solved. Note that since the term in ξ^2 is not present in Eq. (2.16) that $d^2r/d\xi^2 = 0$ at $r = 0$ as well.

An exponential stretching function was used to distribute the points from B to C such that $dr/d\xi$ was matched at B. Along the outer boundary, a third order polynomial was used to distribute the points. Once the distribution of points along the outer boundary from D to E and along the airfoil surface and the symmetry line A to B to C was made, the two boundary technique was used to locate the points in between.

Referring to Fig. 2.6, the ~~two~~ points a and b are first connected by a straight line and the points (x_i, y_i) along it are found by linear interpolation

$$x_i = x_a + t(\eta) \, (x_b - x_a)$$

$$y_i = y_a + t(\eta) \, (y_b - y_a) \qquad (2.17)$$

$$0 < t(\eta) < 1$$

Next, the slopes of the boundaries at a and b are computed as m_b and m_t and the slopes at the intermediate points x_i are found by linear interpolation as m_i in the same manner as above. Straight lines passing through the points x_i with slopes m_i are then constructed and their equations are

$$y = y_i + m_i \, (x - x_i) \qquad (2.18)$$

Lines passing through a and b normal to the boundaries are then constructed which have as their equations

$$y = y_b - \frac{1}{m_b} \, (x - x_b) \quad , \quad y = y_t - \frac{1}{m_t} \, (x - x_t) \qquad (2.19)$$

The points of intersection of these lines with the lines through x_i are then easily computed as $\tilde{x}_b, \tilde{y}_b$ and $\tilde{x}_t, \tilde{y}_t$. Finally the grid points from a to b are found as

$$x = x_i + \alpha_3 \, (\tilde{x}_b - x_i) + \alpha_4 \, (\tilde{x}_t - x_i)$$

$$y = y_i + \alpha_3 \, (\tilde{y}_b - y_i) + \alpha_4 \, (\tilde{y}_t - y_i) \qquad (2.20)$$

Different functions α_3 and α_4 have been experimented. One possible choice is

$$y = y_a - \frac{1}{m_a}(x - x_a)$$

$$y = y_1 + m_1(x - x_1)$$

$$y = y_b - \frac{1}{m_b}(x - x_b)$$
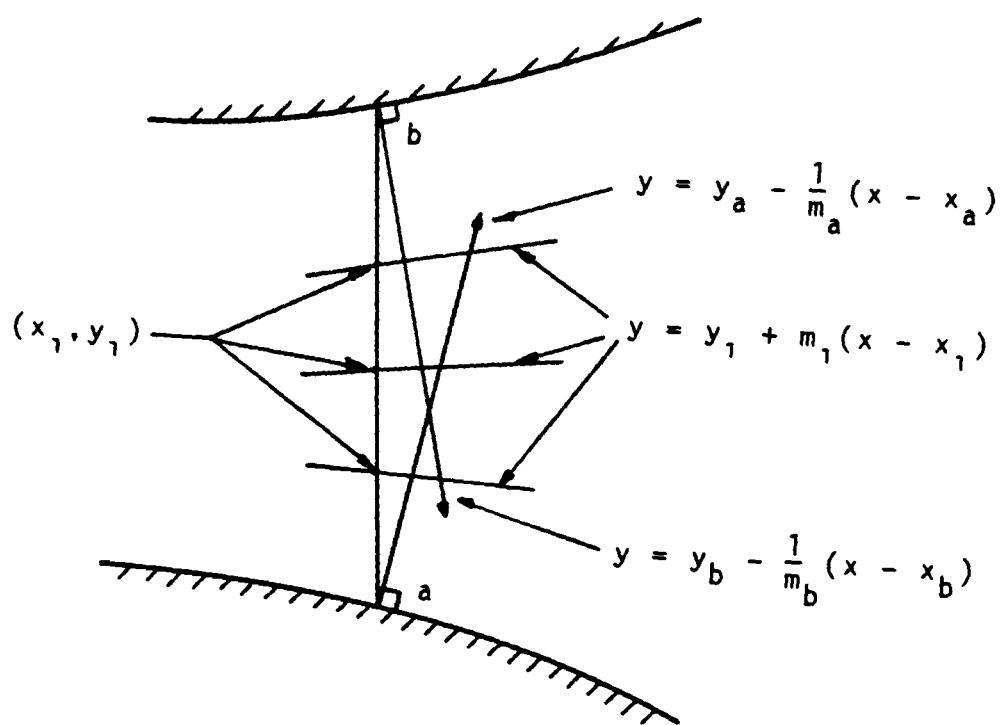
Fig. 2.6 Construction of Connecting Lines.

$$\alpha_3 = K_b^- (1 - n)^2$$

$$\alpha_4 = K_t \, n^2$$

(2.21)

where K_b and K_t are constants.

As long as K_b and K_t are finite, orthogonality will be achieved at least on the two opposing boundaries and this technique can be extended to the side boundaries as well.

2.2.3 Elliptic Smoothing

This technique is based on the following set of Poisson's equations [6]

$$\xi_{xx} + \xi_{yy} = P(x,y)$$

$$n_{xx} + n_{yy} = Q(x,y)$$

(2.22)

where ξ and n are the computational coordinates and P and Q are the source terms that control the resulting grid. Since in most cases x and y as functions of ξ and n are required, the above equations are transformed to

$$\alpha \, x_{\xi\xi} - 2\beta \, x_{\xi n} + \gamma \, x_{nn} = - (P \, x_\xi + Q \, x_n)/J^2$$

$$\alpha \, y_{\xi\xi} - 2\beta \, y_{\xi n} + \gamma \, y_{nn} = - (P \, y_\xi + Q \, y_n)/J^2$$

(2.23)

where the Jacobian $J = x_\xi \, y_n - x_n \, y_\xi$ and

$$\alpha = x_n^2 + y_n^2$$

$$\beta = x_\xi \, x_n + y_\xi \, y_n$$

$$\gamma = x_\xi^2 + y_\xi^2$$

Note that if the grid is orthogonal then

$$\nabla \xi \cdot \nabla \eta = 0$$

which implies that β is zero.

A transformation introduced by Middlecoff and Thomas replaces P and Q by two new function ϕ and ψ as follows [35]:

$$\phi = -\frac{P}{\alpha} \left(\frac{1}{J}\right)^2$$

$$\psi = -\frac{Q}{\gamma} \left(\frac{1}{J}\right)^2$$

(2.24)

with this transformation, Eqs. (2.19) become

$$\alpha \, x_{\xi\xi} - 2\beta \, x_{\xi\eta} + \gamma \, x_{\eta\eta} = \alpha \, \phi \, x_\xi + \gamma \, \psi \, x_\eta$$

$$\alpha \, y_{\xi\xi} - 2\beta \, y_{\xi\eta} + \gamma \, y_{\eta\eta} = \alpha \, \phi \, y_\xi + \gamma \, \psi \, y_\eta$$

(2.25)

The terms on the right are commonly called "source terms" and they are related to the mesh orthogonality and spacing. Equations (2.21) are solved by a SLOR (single line over-relaxation) technique which sweeps alternatively in each of the ξ and η directions. The source terms ϕ and ψ are initially set to zero and are then slowly changed to achieve the required angles and spacing of the grid along the boundaries.

The function ϕ along the boundaries η = constant is varied according to

$$\phi^{n+1} = \phi^n + c_1 \tan\theta$$

(2.26)

where c_1 is some constant and θ is the angle at which the lines of constant ξ intersect the boundary as shown in Fig. 2.7. Along the boundaries ξ = constant, the control function ϕ is varied according to the spacing ds as shown in Fig. 2.8 as given by Eq. (2.27).

$$\phi^{n+1} = \phi^n + c_2 (ds - ds') \tag{2.27}$$

where ds' is the desired spacing and ds is the actual spacing.

The source term ψ is controlled along the boundaries ξ = constant using a procedure similar to ϕ along the η = contant boundary. Along the boundaries η = constant, ψ could be varied to obtain the required spacing in a similar fashion as ϕ along ξ = constant boundaries.

In the interior, ϕ and ψ are determined by bilinear interpolation similar to Eq. (2.13). In this case the variables r and s are related to ξ and η by the following third order polynomial blending functions.

$$r = (3 - 2\xi) \xi^2$$
$$s = (3 - 2\eta) \eta^2 \tag{2.28}$$

This insures that ϕ and ψ blend smoothly from the boundaries into the interior.
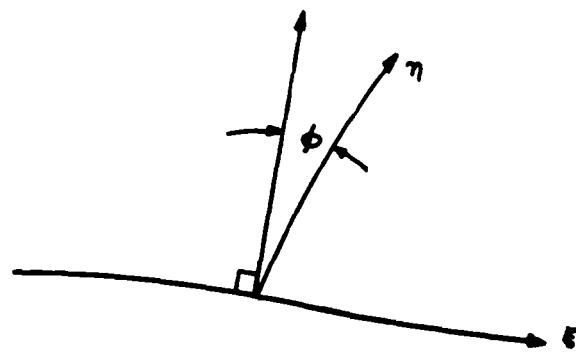
Fig. 2.7   Control of ϕ along η = constant boundary.
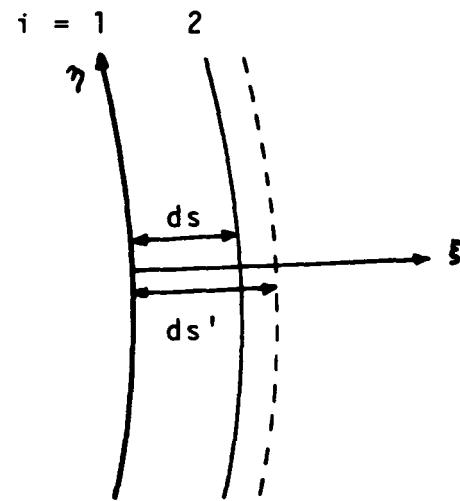
Fig. 2.8   Control of ϕ along ξ = constant boundary.

Chapter 3

GOVERNING EQUATIONS OF FLUID DYNAMICS

3.1 Introduction

In this chapter, the complete governing equations of fluid dynamics in various forms as will be used later are derived. While such a derivation can be found in various books on the subject, the presentation which is given usually depends, to some extent, on the author's background and orientation. For example, the classic book by Batchelor, which gives an excellent derivation of the Navier-Stokes equations, barely discusses compressible flows [36]. Furthermore, advanced topics such as turbulence or weak solutions to the Euler equations are covered in only sketchy detail in most of the introductory texts currently in use. This undoubtedly reflects the fact that fluid dynamics is an extremely broad and interdisciplinary subject which is both highly mathematical and also has applications in many different areas.

The equations which are used in this study are the compressible Euler and Navier-Stokes equations in both conservative and non-conservative form. The viscous equations which are used are for laminar flow and, therefore, the topic of turbulence is not discussed herein. The assumptions which are made are discussed in the appropriate sections. The assumption that the fluid behaves as a continuem is made throughout.

27

3.2 Mass Conservation Equation

The principal of mass conservation states that mass is neither created or destroyed. Therefore, a given differential "fluid element" of density ρ and volume δV moving along with the fluid can be described from the Lagrangian point of view by the equation

$$\frac{D}{Dt} (\rho\ \delta V) = 0 \qquad (3.1)$$

since the mass of the fluid element remains constant. It is now more customary to derive the governing equations from the Eulerian point of view using a control volume fixed in space. Consider a control volume δV with a total mass given by

$$\int_V \rho\ dV = \text{mass inside } \delta V$$

The rate of change of the mass inside δV is then related to the integrated mass flux through the boundaries of δV which is

$$\int_\rho \vec{V} \cdot n\ dA = \text{net mass flux}$$

and therefore the mass conservation law in

$$\frac{\partial}{\partial t} \int_V \rho\ dV = -\int_A \rho\ \vec{V} \cdot n\ dA \qquad (3.2)$$

Equation (3.2) is the integral form of the mass conservation law and applies even when p and $\vec{V}$ are not differentiable.

Using the divergence theorem and assuming the control volume to be fixed, this can be written as

$$\int_V [\frac{\partial \rho}{\partial t} + \text{div}\ (\rho\ \vec{V})]\ dV = 0$$

Since this equation must hold for all V, it can be written in differential form as

$$\rho_t + \nabla \cdot (\rho \, \vec{V}) = 0 \qquad (3.3)$$

It can be shown that Eq. (3.3) is equivalent to Eq. (3.1), for example see Karamcheti [31]. In two-dimensions, Eq. (3.3) can also be written as

$$\rho_t + (\rho u)_x + (\rho v)_y = 0 \qquad (3.4)$$

3.3 Momentum Equation

The principal of conservation of momentum follows from Newton's second law which is valid for non-relatavistic masses and states that

$$\vec{F} = \frac{d}{dt} (m \, \vec{V}) \qquad (3.5)$$

where $\vec{F}$ is the applied force, m is the mass and $\vec{V}$ is the velocity. For a moving infinitesimal fluid element this can be written as

$$\vec{F} = \frac{D}{Dt} (\rho \, \vec{V} \, \delta \, V) \qquad (3.6)$$

where D/Dt is the substantial (or material) derivative and δV is the elemental volume

The force in the left side of Eq. (3.6) is usually considered to consist of body forces which are the result of gravitational or magnetic fields and surface forces which only act on surfaces and which are pressure and viscous stresses. Normally in aerodynamic analyses the body forces are neglected since they are negligible due to the fact that a moving body of air has a much larger kinetic energy than a potential energy.

It can be shown that the surface forces on a fluid element can be collectively and completely described by a second order stress tensor σ_{ij} (The derivation of this fact is contained in most fluid dynamic textbooks and will not be repeated herein). The interpretation of the individual components of this tensor is that σ_{ij} is the force in the ith direction on an element of area whose normal is in the jth direction. It can also be shown that the stress tensor is symmetric so that $\sigma_{ij} = \sigma_{ji}$. This is due to the fact that an infinitesimal fluid element cannot support moment forces as the volume goes to zero faster than the rotational forces which would otherwise lead to infinite rotational moment forces per unit volume. When referred to the principal axes, it is found that the off-diagonal components of the stress tensor are zero and that the sum of the diagonal elements, referred to as the principal stresses, is an invariant sum under changes of direction of the orthogonal axis of reference.

The stress tensor in reference to the principal axes can be split and expressed as the sum of two tensors

$$\frac{1}{3}\begin{bmatrix} \tau_{ii} & & \\ & \tau_{ii} & \\ & & \tau_{ii} \end{bmatrix} + \begin{bmatrix} \sigma_{11} - \frac{1}{3}\tau_{ii} & & \\ & \sigma_{22} - \frac{1}{3}\tau_{ii} & \\ & & \sigma_{33} - \frac{1}{3}\tau_{ii} \end{bmatrix} \quad (3.7)$$

where σ_{11}, σ_{22}, and σ_{33} are the principal stresses. The first part of Eq. (3.7) is an isotropic tensor and the second part is referred to as the deviatoric stress tensor. In a fluid at rest, all of the components of the deviatoric stress are zero so the isotropic stress is simply due to hydrostatic pressure and

$$\sigma_{ij} = -p\,\delta_{ij}$$

where p is the uniform hydrostatic pressure. In a moving fluid, the isotropic stress tensor is still considered to be due to hydrostatic pressure and the components of the deviatoric sress are nonzero. Thus, in general, the stress tensor can be written as

$$\sigma_{ij} = -p \, \delta_{ij} + \tau_{ij} \qquad (3.8)$$

where τ_{ij} is the deviatoric stress. The deviatoric stress is related to the motion of the fluid and in particular to the local velocity gradients $\partial u_i / \partial x_j$. If it is assumed that τ_{ij} is a linear function of $\partial u_i / \partial x_j$, then

$$\tau_{ij} = A_{ijk\ell} \, \partial u_k / \partial x_\ell \qquad (3.9)$$

where $A_{ijk\ell}$ is a fourth order tensor coefficient. The tensor of the local velocity gradient can also be written as the sum of a symmetrical tensor, called the rate-of-strain tensor and an anti-symmetrical tensor which represents pure rotation. Thus

$$\frac{\partial u_k}{\partial x_\ell} = \frac{1}{2} \left(\frac{\partial u_k}{\partial x_\ell} + \frac{\partial u_\ell}{\partial x_k} \right) + \frac{1}{2} \left(\frac{\partial u_k}{\partial x_\ell} - \frac{\partial u_\ell}{\partial x_k} \right)$$

$$= e_{k\ell} + \xi_{k\ell}$$

$$= e_{k\ell} - \frac{1}{2} \epsilon_{k\ell m} \omega_m \qquad (3.10)$$

where ω_m is the angular vorticity. Thus

$$\tau_{ij} = A_{ijk\ell} \left(e_{k\ell} - \frac{1}{2} \epsilon_{k\ell m} \omega_m \right). \qquad (3.11)$$

If $A_{ijk\ell}$ is also assumed to be an istropic tensor, then the fluid is said to be "Newtonian" and $A_{ijk\ell}$ can be expressed as the sum of the product of delta tensors

$$A_{ijk\ell} = \mu \, \delta_{ik} \, \delta_{j\ell} + \mu_1 \, \delta_{i\ell} \, \delta_{jk} + \mu_2 \, \delta_{ij} \, \delta_{k\ell} \tag{3.12}$$

where μ, μ_1, and μ_2 are scalar coefficients. It turns out that μ is the molecular viscosity of the fluid which is frequently regarded simply as a constant but which is a function of the state of the fluid. Since the stress tensor is symmetric, it must be true that $A_{ijk\ell}$ is also symmetric in i and j and that $\mu = \mu_1$. $A_{ijk\ell}$ must also be symmetrical in k and ℓ with the result that the vorticity term in Eq. (3.11) must be zero and therefore

$$\tau_{ij} = 2\mu \, e_{ij} + \mu_2 \, e_{kk} \, \delta_{ij} \tag{3.13}$$

where $e_{kk} = \nabla \cdot \vec{V}$ is the divergence of $\vec{V}$.

The coefficient μ_2 is frequently called the second coefficient of viscosity or Lame's constant and given the symbol λ. Since in a fluid at rest, it must be true that τ_{ij} is zero so that the mean normal stress is just equal to $-p \, \delta_{ij}$, Stoke's theorem assumes

$$\lambda = -\frac{2}{3} \mu \tag{3.14}$$

The stress tensor is finally given by

$$\sigma_{ij} = -p \, \delta_{ij} + 2\mu \left(e_{ij} - \frac{1}{3} \nabla \cdot \vec{V} \, \delta_{ij} \right) \tag{3.15}$$

The rate of change of momentum inside a control volume δV is equal to the sum of the net momentum flux through the boundaries of δV plus the change of momentum inside δV due to the forces acting on δV. The net change of momentum inside δV is

$$\frac{d}{dt} \int_V \rho \, \vec{V} \, dV$$

The net momentum flux in through the boundaries of δV is

$$\int_{\partial V} \rho \, \vec{V} \vec{V} \cdot d\vec{A}$$

where $\rho \, \vec{V} \vec{V}$ is a dyadic called the momentum flux tensor. The integrated force due to pressure and the viscous stresses is

$$\int_{\partial V} (-p \cdot \vec{n} + \tau_{ij} \cdot n) \, dA$$

The momentum equation is then

$$\frac{d}{dt} \int_V \rho \, \vec{V} \, dV + \int_{\partial V} \rho \, \vec{V} \vec{V} \cdot d\vec{A} = \int_{\partial V} (-p + \tau_{ij}) \cdot d\vec{A} \qquad (3.16)$$

Equation (3.16) is the momentum equation in integral form and applies even when there are discontinuties in the fluid. By making use of the generalized divergence theorem and assumming that ρ, p, and $\vec{V}$ are sufficiently smooth, Eq. (3.16) becomes

$$\int_V \left\{ \frac{\partial}{\partial t} (\rho \, \vec{V}) + \nabla \cdot (\rho \, \vec{V} \vec{V} + p - \tau_{ij}) \right\} dV = 0 \qquad (3.17)$$

Equation (3.17) must apply to all parts of the control volume and can also be written simply as

$$\frac{\partial}{\partial t} (\rho \, \vec{V}) + \nabla \cdot (\rho \, \vec{V} \vec{V} + p) = \nabla \cdot \tau_{ij} \qquad (3.18)$$

Equation (3.18) is the Navier-Stokes equation in conservation form. If the viscous stresses are assumed to be zero, then Eq. (3.18) becomes

$$\frac{\partial}{\partial t} (\rho \, \vec{V}) + \nabla \cdot (\rho \, \vec{V} \vec{V} + p) = 0 \qquad (3.19)$$

which is the Euler equation governing inviscid fluids. Equations (3.18) and (3.19) can be written in what is called non-conservation form by subtracting out the mass conservation equation which occurs in them. The result is

$$\rho \, \frac{D\vec{V}}{Dt} = \nabla \cdot \sigma_{ij} \qquad (3.20)$$

which is a very compact form of the Navier-Stokes equations but which is still valid in general.

3.4 Energy Conservation Equation

The full three-dimensional mass and momentum conservation equations contain the five variables ρ, p, μ, v, and w. Since there are only four equations thus far, another equation is needed to close the set and this is the energy conservation equation. In the chapters which follow, the energy equation will be used in different forms so a unified derivation is presented here. The energy equation is obtained by application of the first law of thermodynamics which relates the rate of change of the energy inside a control volume to the energy flux through the boundaries of the control volume and to the rate at which work is done on the fluid.

The total energy of the flow field is the sum of the internal energy, kinetic energy, and potential energy. The potential energy is normally neglected in aerodynamic flows since the density of air is very low. Thus the rate of change of the total energy inside the control volume δV is

$$\frac{dE_t}{dt} = \frac{d}{dt} \int_V \rho \, (e + q^2/2) \, dV$$

where E_t is the total energy, e is the internal energy and $q^2/2$ is the kinetic energy.

The energy flux in through the boundaries, due to convective flux of internal and kinetic energy, is given by

$$- \int_{\partial V} \rho (e + q^2/2) \, \vec{V} \cdot d\vec{A} \quad .$$

The conductive heat flux is given by

$$- \int_{\partial V} \vec{q} \cdot d\vec{A}$$

The heat flux $\vec{q}$ is related to the gradient of the temperature by Fourier's law which is

$$\vec{q} = - k \nabla T$$

where k is the thermal conductivity. In many derivations of the energy equation, a term is added to account for the heat added per unit mass such as would occur from an exothermic chemically reacting flow. This term is usually given by the following volume integral

$$\int_V \rho \, \dot{q} \, dV$$

where $\dot{q}$ is the rate of heat addition per unit mass. In this investigation, no such flows are considered and, therefore, this term is not included.

The work done on the fluid inside δV is due to the stress tensor and is given by

$$\int_{\partial V} (\sigma_{ij} \, \vec{V}) \cdot d\vec{A} = \int_{\partial V} [(- p + \tau_{ij}) \vec{V}] \cdot d\vec{A}$$

Combining the above expressions, the integral form of the energy conservation equation is

$$\frac{d}{dt} \int_V \rho (e + q^2/2) \, dV = \int_{\partial V} [-\rho (e + q^2/2) \, \vec{V} + k \nabla T + (-p + \tau_{ij}) \vec{V}] \cdot d\vec{A}$$

$$(3.21)$$

Equation (3.21) is very general and applies even when there are discontinuties in the flow. By making use of the divergence theorem, Eq. (3.21) can also be written in differential form as

$$\frac{\partial}{\partial t} E_t + \nabla \cdot [E_t \vec{V} - k \nabla T + (\rho - \tau_{ij}) \vec{V}] = 0 \tag{3.22}$$

If the fluid is considered to be inviscid and non-conductive, then Eq. (3.22) reduces to

$$\frac{\partial}{\partial t} E_t + \nabla \cdot [(E_t + p)\vec{V}] = 0 \tag{3.23}$$

Equation (3.23) can be expanded to

$$\rho \frac{\partial (e + q^2/2)}{\partial t} + (e + \frac{q^2}{2}) \frac{\partial \rho}{\partial t} + (e + \frac{q^2}{2}) \nabla \cdot (\rho \vec{V})$$

$$+ \rho \vec{V} \cdot \nabla (e + \frac{q^2}{2}) + \nabla \cdot (p \vec{V}) = 0$$

the second and third terms can be dropped since they include the mass conservation equation to yield

$$\rho \frac{D (e + q^2/2)}{Dt} + \nabla \cdot (p \vec{V}) = 0 \tag{3.24}$$

Equation (3.24) can be split into two equations as follows. First, Eq. (3.20) can be written for an invicid fluid as

$$\rho \frac{D\vec{V}}{Dt} + \nabla p = 0$$

This equation can be dotted with $\vec{V}$ to form a scaler equation

$$\rho V \cdot \frac{D\vec{V}}{Dt} + V \cdot \nabla p = 0 \tag{3.25}$$

Equation (3.25) can be subtracted from Eq. (3.24) to yield

$$\rho \frac{De}{Dt} + p \nabla \cdot \vec{V} = 0 \tag{3.26}$$

which expresses the rate of change of internal energy of a moving fluid element. Equation (3.26) can be put in terms of the enthalpy using the definition of enthalpy

$$h = e + pv = e + p/\rho \qquad (3.27)$$

Substituting Eq. (3.27) in Eq. (3.26) and by making use of the mass conservation equation, it can be shown that the following equation holds.

$$\rho \frac{Dh}{Dt} + \frac{Dp}{Dt} = 0 \qquad (3.28)$$

Furthermore, by adding together Eqs. (3.28) and (3.24), subtracting Eq. (3.26), and by making use of the defintion of total enthalpy, namely, $h_0 = h + q^2/2$, we obtain the following energy equation in terms of the total enthalpy.

$$\rho \frac{Dh_0}{Dt} + \frac{\partial p}{\partial t} = 0 \qquad (3.29)$$

If the flow is steady, Eq. (3.29) reduces to

$$\frac{Dh_0}{Dt} = 0 \qquad (3.30)$$

Equation (3.30) expresses the fact that the total enthalpy along a fluid streamline is constant for invicid flows.

3.5 Two-Dimensional Form of Equations

Since the problems studied in this investigation were two-dimensional in nature, this section contains a summary of the governing equations in two dimensions and in various forms. The most compact way of expressing the Navier Stokes equations is in the vector conservation form given below

$$Q_t + F_x + G_y = R_x + S_y \tag{3.31}$$

where Q is the vector of the conserved variables given as

$$Q = [\rho, \rho u, \rho v, e]^T$$

and F and G are the convective flux vectors given as

$$F = \begin{bmatrix} \rho u \\ \rho u^2 + p \\ \rho uv \\ (e + p) u - kT_x \end{bmatrix}$$

$$G = \begin{bmatrix} \rho v \\ \rho uv \\ \rho v^2 + p \\ (e + p) v - kT_y \end{bmatrix}$$

and R and S are the viscous flux terms which are

$$R = \begin{bmatrix} 0 \\ \tau_{xx} \\ \tau_{xy} \\ u\tau_{xx} + v\tau_{xy} \end{bmatrix}$$

$$S = \begin{bmatrix} 0 \\ \tau_{xy} \\ \tau_{yy} \\ u\tau_{xy} + v\tau_{yy} \end{bmatrix}$$

The viscous stress terms in Eq. (3.31) are

$$\tau_{xx} = \frac{2}{3} \mu \left(2 \frac{\partial u}{\partial x} - \frac{\partial v}{\partial y} \right)$$

$$\tau_{yy} = \frac{2}{3} \bar{\mu} \left(2 \frac{\partial v}{\partial y} - \frac{\partial u}{\partial x} \right) \qquad (3.32)$$

$$\tau_{xy} = \mu \left(\frac{\partial u}{\partial y} + \frac{\partial v}{\partial x} \right)$$

The total energy per unit mass is the sum of the internal energy and the kinetic energy as follows:

$$e = i + \frac{u^2 + v^2}{2} \qquad (3.33)$$

Equations (3.31), (3.32) and (3.33) together contain five scalar equations in the nine quantities ρ, u, v, p, e, i, t, k, and μ. In the model being used, the thermal conductivity k and the molecular viscosity μ are considered constant so two additional equations are needed to close the system. The first is the perfect gas equation of state

$$p = \rho R T \qquad (3.34)$$

where R is the gas constant. If the fluid is assumed to be calorically perfect, then

$$i = c_v T \qquad (3.35)$$

and consquently by Eq. (3.34) and the relation

$$c_v = \frac{R}{\gamma - 1} \qquad (3.36)$$

it holds that

$$i = p/[(\gamma - 1)\rho]. \qquad (3.37)$$

The governing equations can be nondimensionalized by referring them to suitable reference quantities as follows:

$$x' = x/\ell_0 \qquad y' = y/\ell_0 \qquad t' = t\, a_0/\ell_0$$

$$u' = u/a_0 \qquad v' = v/a_0 \qquad \rho' = \rho/\rho_0 \qquad (3.38)$$

$$p' = p/(\rho_0 \, a_0^2) \qquad e' = e/(\rho_0 \, a_0^2) \qquad \mu' = \mu/\mu_0$$

$$i' = i/a_0^2 \qquad T' = T/T_0$$

The resulting equations after nondimensionalizing are:

$$\frac{\partial Q'}{\partial t'} + \frac{\partial F'}{\partial x'} + \frac{\partial G'}{\partial y'} = \frac{1}{Re}\left(\frac{\partial R'}{\partial x'} + \frac{\partial S'}{\partial y'}\right) \qquad (3.39)$$

where

$$Q' = [\rho', \rho'u', \rho'v', e']^T$$

$$F' = \begin{bmatrix} \rho'u' \\ \rho'u'^2 + p' \\ \rho'u'v' \\ (e' + p')u' + q'_x \end{bmatrix}$$

$$G' = \begin{bmatrix} \rho'v' \\ \rho'u'v' \\ \rho'v'^2 + p' \\ (e' + p')v' + q'_y \end{bmatrix}$$

$$R' = \begin{bmatrix} 0 \\ \tau'_{xx} \\ \tau'_{xy} \\ u'\tau'_{xx} + v'\tau'_{xy} \end{bmatrix}$$

$$S' = \begin{bmatrix} 0 \\ \tau'_{xy} \\ \tau'_{yy} \\ u'\tau'_{xy} + v'\tau'_{yy} \end{bmatrix}$$

and

$$\tau'_{xx} = \frac{2}{3} \mu' \left(2 \frac{\partial u'}{\partial x'} - \frac{\partial v'}{\partial y'}\right)$$

$$\tau'_{yy} = \frac{2}{3} \mu' \left(2 \frac{\partial v'}{\partial y'} - \frac{\partial u'}{\partial x'}\right)$$

$$\tau'_{yy} = \left(\frac{\partial u'}{\partial y'} + \frac{\partial v'}{\partial x'}\right)$$

The reference Reynolds number is given by

$$Re_0 = \frac{a_0 \, \rho_0 \, \ell_0}{\mu_0}$$

The equation for the total energy, Eq. (3.33), becomes, after nondimensionalizing,

$$e' = i' + \frac{u'^2 + v'^2}{2} \tag{3.40}$$

and the equation of state, Eq. (3.37), becomes

$$i' = p'/[(\gamma - 1) \, \rho'] \tag{3.41}$$

Thus the original equations are replaced by equations which have the same form but which now include the reference Reynolds number in the momentum equations and the reference Peclet number $(Re_0 \, Pr_0)$ in the energy equation.

The Euler equations for inviscid fluids are obtained from Eqs. (3.31) and (3.39) by dropping the viscous flux terms R and S. Thus we have

$$Q_t + F_x + G_y = 0 \tag{3.42}$$

Equation (3.42) is written out as

$$\rho_t + (\rho u)_x + (\rho v)_y = 0$$

$$(\rho u)_t + (\rho u^2 + p)_x + (\rho uv)_y = 0$$

$$(\rho v)_t + (\rho uv)_x + (\rho v^2 + p)_y = 0 \qquad (3.43)$$

$$e_t + [(e + p)u - kT]_x + [(e + p)v - kT]_y = 0$$

Equation (3.43) are in conservation form and include an energy equation in terms of the internal energy. In the three schemes used to solve the Euler equations, this form of the energy equation was not used. Instead, energy equations in terms of either the enthalpy or entropy were used.

In the following discussion and derivation, the primes are dropped for convenience and it should be understood that all quantities are non-dimensional.

The next step is to transform the equations to general curvilinear coordinates in conservation law form. Equation (3.39) is transformed to

$$\tilde{Q}_\tau + \tilde{F}_\xi + \tilde{G}_\eta = \tilde{R}_\xi + \tilde{S}_\eta \qquad (3.44)$$

where

$$\tilde{Q} = Q/J$$

$$\tilde{F} = (F \xi_x + G \xi_y)/J$$

$$\tilde{G} = (F \eta_x + G \eta_y)/J$$

$$\tilde{R} = (R\xi_x + S\xi_y)/J$$

$$\tilde{S} = (R\eta_x + S\eta_y)/J$$

Chapter 4

SCHEME 1 - SHOCK CAPTURING GABUTTI

4.1 Introduction

The first computational scheme used in this study is the Gabutti scheme which is a refinement of the λ-scheme developed earlier by Moretti [28]. The scheme solves the time dependent compressible Euler equations in non conservation form by an explicit predictor-corrector method. Gabutti's method improves upon the λ-scheme by extending the stability range substantially and also by enabling it to satisfy the shift condition for a CFL of one which is

$$u_i^{n+1} = u_{i-1}^n .$$

The scheme has good shock capturing properties in that the discontinuity is usually spread over no more than two or three mesh points. The jumps in density, pressure, and velocity through the shock are not correct due to the nonconservative nature of the scheme, however, and shock fitting must be used to get the correct jump relations. The scheme solves the mass conservation, and x and y momentum equations in non-conservative form as

$$\rho_t + u\rho_x + v\rho_y + \rho\,(u_x + v_y) = 0$$

$$u_t + uu_x + vu_y + \frac{1}{\rho}\,p_x = 0 \qquad (4.1)$$

$$v_t + uv_x + vv_y + \frac{1}{\rho} p_y \qquad = 0 .$$

If the flow is assumed isentropic along streamlines, and if we use the change of variables $P = \ell n\ p$, then the above equations can be written as

$$P_t + uP_x + vP_y + \gamma (u_x + v_y) = 0$$

$$u_t + uu_x + vu_y + \frac{a^2}{\gamma} P_x \qquad = 0 \qquad\qquad (4.2)$$

$$v_t + uv_x + vv_y + \frac{a^2}{\gamma} P_y \qquad = 0 .$$

The energy equation in its usual differential form is not used, but rather the assumption is made that the flow is isenthalpic. In this case, the square of the speed of sound a^2 is related to the velocities by the steady state energy equation

$$\frac{a^2}{\gamma-1} + \frac{u^2 + v^2}{2} = h_o \qquad\qquad (4.3)$$

where h_o is the total enthalpy. If the pressure p and the density ρ are nondimensionalized by dividing by their stagnation values p_0 and ρ_0, then

$$h_o = \frac{a_o^2}{\gamma-1} = \frac{\gamma}{\gamma-1} . \qquad\qquad (4.4)$$

4.2 Transformation of Equations

In order to use the governing equations, it is first desirable to transform them to (ξ,η) coordinates. Using Eqs. (2.4) and the chain rule, the mass conservation equation becomes

$$P_t + UP_\xi + VP_\eta + \gamma [U_\xi + V_\eta] = P_s \qquad\qquad (4.6).$$

where U and V are the contravariant velocities

$$U = \xi_x u + \xi_y v \tag{4.7a}$$

$$V = \eta_x u + \eta_y v \tag{4.7b}$$

and
$$P_s = -\gamma \, J \, [g_4 U + g_5 V] \; . \tag{4.7c}$$

The terms g_4 and g_5 are two of 11 transformation terms that appear in the governing equations after transformation and these are given by

$$g_1 = x_\xi^2 + y_\xi^2$$

$$g_2 = x_\eta^2 + y_\eta^2$$

$$g_3 = x_\xi \, x_\eta + y_\xi \, y_\eta$$

$$g_4 = x_{\xi\xi} \, y_\eta - x_{\xi\eta} \, y_\xi - y_{\xi\xi} \, x_\eta + y_{\xi\eta} \, x_\xi$$

$$g_5 = x_{\xi\eta} \, y_\xi - x_{\eta\eta} \, y_\xi - y_{\xi\eta} \, x_\eta + y_{\eta\eta} \, x_\xi$$

$$g_6 = y_\eta \, x_{\xi\xi} - x_\eta \, y_{\xi\xi}$$

$$g_7 = y_\eta \, x_{\eta\eta} - x_\eta \, y_{\eta\eta}$$

$$g_8 = 2 \, (y_\eta \, x_{\xi\eta} - x_\eta \, y_{\xi\eta})$$

$$g_9 = x_\xi \, y_{\xi\xi} - y_\xi \, x_{\xi\xi}$$

$$g_{10} = x_\xi \, y_{\eta\eta} - y_\xi \, x_{\eta\eta}$$

$$g_{11} = 2 \, (x_\xi \, y_{\xi\eta} - y_\xi \, x_{\xi\eta}) \; . \tag{4.8}$$

The transformation of the two momentum equations is somewhat more complicated. First, they are written in vector form as

$$Q_t + u Q_x + v Q_y + S = 0 \tag{4.9}$$

where $\qquad Q = [u, v]^T$ and $S = \dfrac{a^2}{\gamma} [P_x, P_y]^T$.

The vector Q can also be written as

$$Q = \begin{bmatrix} u \\ v \end{bmatrix} = \begin{bmatrix} x_\xi & x_\eta \\ y_\xi & y_\eta \end{bmatrix} \begin{bmatrix} U \\ V \end{bmatrix} = \tilde{T} \tilde{Q} \qquad (4.10)$$

where $\qquad \tilde{T} = \begin{bmatrix} x_\xi & x_\eta \\ y_\xi & y_\eta \end{bmatrix}$

$$\tilde{Q} = \begin{bmatrix} U \\ V \end{bmatrix} \quad .$$

Multiplying Eq. (4.10) by $\tilde{T}^{-1}$ gives

$$\tilde{Q}_t + \tilde{T}^{-1} [u\,(\tilde{T}\,\tilde{Q})_x + v\,(\tilde{T}\,\tilde{Q})_y] + \tilde{T}^{-1} S = 0 \quad .$$

Note it is assumed that $\tilde{T}$ is independent of time. The previous equation is equivalent to

$$\tilde{Q}_t + \tilde{T}^{-1} [U(\tilde{T}\,\tilde{Q})_\xi + V(\tilde{T}\,\tilde{Q})_\eta] + \tilde{T}^{-1} S = 0$$

which can be manipulated to get

$$\tilde{Q}_t + U\,\tilde{Q}_\xi + V\,\tilde{Q}_\eta + \tilde{S} = 0 \qquad (4.11)$$

where
$$\tilde{S} = \tilde{T}^{-1} [U\,\tilde{T}_\xi\,\tilde{Q} + V\,\tilde{T}_\eta\,\tilde{Q}] + T^{-1} S \quad .$$

Equation (4.11) written out is

$$U_t + UU_\xi + VU_\eta + \frac{(Ja)^2}{\gamma} [g_2 P_\xi - g_3 P_\eta] = U_s \qquad (4.12a)$$

$$V_t + UV_\xi + VV_\eta + \frac{(Ja)^2}{\gamma} [g_1 P_\eta - g_3 P_\xi] = V_s \qquad (4.12b)$$

where

$$U_s = -J (g_6 U^2 + \bar{g_7} V^2 + g_8 UV) \qquad (4.12c)$$

$$V_s = -J (g_9 U^2 + g_{10} V^2 + g_{11} UV) \quad . \qquad (4.12d)$$

If the transformation from (x,y) to (ξ,η) is conformal, then the above two equations can be reduced using the Cauchy-Riemann equations to

$$U_t + UU_\xi + VU_\eta + \frac{Ja^2}{\gamma} P_\xi - \frac{U^2 + V^2}{2} J_1 - UV J_2 = 0 \qquad (4.13a)$$

$$V_t + UV_\xi + VV_\eta + \frac{Ja^2}{\gamma} P_\eta - UV J_1 - \frac{U^2 + V^2}{2} J_2 = 0 \qquad (4.13b)$$

where

$$J_1 = J_\xi / J$$

$$J_2 = J_\eta / J \quad .$$

The λ-scheme introduced by Moretti is next used to put Eqs. (4.6) and (4.12) into a quasi-characteristic form. First, the time derivative of P is split into two parts P_t^ξ and P_t^η such that

$$P_t^\xi + U P_\xi + \gamma U_\xi = \frac{1}{2} P_s \qquad (4.14)$$

$$P_t^\eta + V P_\eta + \gamma V_\eta = \frac{1}{2} P_s \quad . \qquad (4.15)$$

Equations (4.12a) and (4.14) can be written as

$$\tilde{Q}_t^\xi + A \tilde{Q}_\xi^\xi = S_1 \qquad (4.16)$$

where

$$A = \begin{bmatrix} U & \gamma \\ \tilde{a}_1^2/\gamma & U \end{bmatrix}$$

$$\tilde{a}_1 = [(Ja)^2 (x_\eta^2 + y_\eta^2)]^{1/2}$$

and S_1 is the vector of the remaining terms put on the right side of Eq. (4.16). The eigenvalues of matrix A are

$$\lambda^{\pm} = U \pm \tilde{a}_1 .$$

Equation (4.16) can be diagonalized as

$$\tilde{Q}_t^{\xi} + [S] [\lambda] [S]^{-1} \tilde{Q}_{\xi}^{\xi} = S_1 \qquad (4.17)$$

where [S] is the matrix of the eigenvectors. If [λ] is split into its positive and negative eigenvalues, Eq. (4.17) becomes

$$\tilde{Q}_t^{\xi} + [S] [\lambda^{+}] [S]^{-1} \tilde{Q}_s^{\xi^+} + [S] [\lambda^{-}] [S]^{-1} \tilde{Q}_{\xi}^{\xi^-} = S_1 . \qquad (4.18)$$

Similary, Eqs. (4.12b) and (4.15) can be written as

$$\tilde{Q}_t^{\eta} + B \tilde{Q}_{\eta}^{\eta} = S_2 \qquad (4.19)$$

where

$$B = \begin{bmatrix} V & \gamma \\ \tilde{a}_2^2/\gamma & V \end{bmatrix}$$

$$\tilde{a}_2 = [(Ja)^2 (x_{\xi}^2 + y_{\xi}^2)]^{1/2} .$$

The eigenvalues of Eq. (4.19) are

$$\Omega^{\pm} = V \pm \tilde{a}_2 .$$

Equation (4.19) can be diagonalized and split into positive and negative components. The result is

$$\tilde{Q}_t^{\eta} + [R] [\Omega^{+}] [R]^{-1} \tilde{P}_{\eta}^{\eta^+} + [R] [\Omega^{-}] [R]^{-1} \tilde{Q}_{\eta}^{\eta^-} = S_2 . \qquad (4.20)$$

Equations (4.18) and (4.20) can be added together to get the final set of equations which are given below

$$P_t + \frac{1}{2}[\lambda^+ P_\xi^+ + \lambda^- P_\xi^- + \Omega^+ P_\eta^+ + \Omega^- P_\eta^- + \frac{\gamma}{aJ_2}(\lambda^+ U_\xi^+ - \lambda^- U_\xi^-)]$$

$$+ \frac{\gamma}{aJ_1}(\Omega^+ V_\eta^+ - \Omega^- V_\eta^-) \qquad = P_s$$

$$U_t + \frac{1}{2}[\lambda^+ U_\xi^+ + \lambda^- U_\xi^- + \frac{aJ_2}{\gamma}(\lambda^+ P_\xi^+ - \lambda^- P_\xi^-)]$$

$$+ VU_\eta - \frac{(Ja)^2}{\gamma} g_3 P_\eta \qquad = U_s$$

$$V_t + \frac{1}{2}[\Omega^+ V_\eta^+ + \Omega^- V_\eta^- + \frac{aJ_1}{\gamma}(\Omega^+ P_\eta^+ - \Omega^- P_\eta^-)]$$

$$+ UV_\eta - \frac{(Ja)^2}{\gamma} g_3 P_\xi \qquad = V_s \qquad (4.21)$$

where P_s, U_s and V_s are unchanged but

$$J_1 = J\sqrt{x_\xi^2 + y_\xi^2}$$

$$J_2 = J\sqrt{x_\eta^2 + y_\eta^2} \ .$$

4.3 Discretization of Equations

Equation (4.22) is now in a form that allows a proper discretization of the spatial derivatives according to the signs of the eigenvalues multiplying them by taking into account the domain of dependence. In two-dimensional unsteady flow, the governing Euler equations are hyperbolic in time and the solution at any point $\underline{X}$ at time $t + \Delta t$ depends on the solution at time t within the area dA as shown in Fig. 4.1. The conoid from the solution surface at time t to point $\underline{X}$ at

t + Δt   is called a Monge cone—and it depicts the way the solution propagates in time [37]. The numerical algorithm should model the way information propagates which means it must take into account the proper domain of dependence. Therefore, the information used to update each mesh point should be taken from adjacent mesh points in a manner that reflects the physical propagation of information. In supersonic flow, for example, pressure waves do not propagate upstream and no information from downstream points should be used to update the solution at a given mesh point.

The Courant-Frederick-Lewy, or CFL, stability condition reflects the requirement that the region of dependence must be at least as large as the analytical domain of dependence [6]. In addition, Moretti also refers to the "law of forbidden signals" and states that in addition to satisfying the CFL stability condition, a numerical scheme should also satisfy this law [28]. What this means in practice is that in supersonic flow, the information that is used to generate the updated solution at a particular mesh point should not come from points downstream of it. This is not always possible but the present scheme does attempt to follow this principal as closely as possible.

Equations (4.21) are solved using the three-step predictor-corrector scheme [27]. The scheme will be described using the one-dimensional linear wave equation as a model problem

$$u_t + a\, u_x = 0 \ . \tag{4.22}$$

In step 1 of the scheme, the spatial derivative u_x is evaluated by either a two point backward or forward difference, depending on the sign of the characteristics as
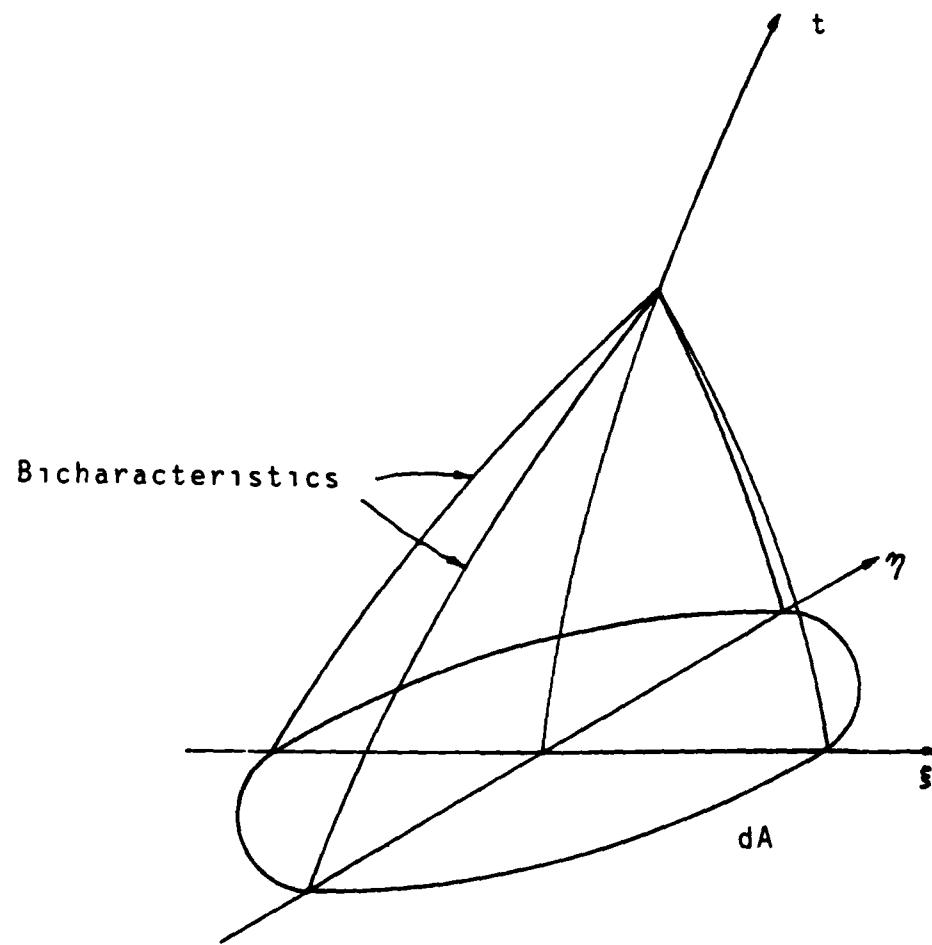
Fig. 4.1   Characteristic Monge Cone.

$$u_x = \nabla u_i = \frac{u_i - u_{i-1}}{\Delta x} \qquad \text{if } a < 0$$

$$u_x = \Delta u_i = \frac{u_{i+1} - u_i}{\Delta x} \qquad \text{if } a > 0 \ . \tag{4.23}$$

A predicted value $\tilde{u}_i$ is then calculated using the u_t that results from Eq. (4.22). For example, if the wave speed a is positive then

$$\tilde{u}_i = u_i^n + u_t \Delta t \tag{4.24}$$

where $\qquad\qquad u_t = - a \ u_x$

In step two of the scheme, the values of u_i at time level n are used again to compute u_t. Depending on the wave speed a, u_x is computed as

$$u_x = \frac{2u_i^n - 3u_{i-1}^n + u_{i-2}^n}{\Delta x} \ , \ a > 0. \tag{4.25}$$

$$u_x = - \frac{2u_i^n - 3u_{i+1}^n + u_{i+2}^u}{\Delta x} \ , \ a < 0. \tag{4.26}$$

Then, compute u_t as

$$u_t = - a \ u_x$$

In step three of the scheme, the predicted values $\tilde{u}_i$ are used to compute a predicted $\tilde{u}_t$ with two step backward or forward differences, depending as in Eq. (4.23) again on the sign of the characteristic speed a. The final update is then made using both the u_t computed in step two and $\tilde{u}_t$ as follows

$$u_i^{n+1} = u_i^n + \frac{1}{2} (u_t + \tilde{u}_t) \Delta t \ . \tag{4.27}$$

In this example, the sign of the wave speed a determines the direction in which the spatial derivatives are taken. In Eqs. (4.21), the characteristics λ^+ and λ^-, and Ω^+ and Ω^- perform this function. The scheme satisfies the so-called "shift" condition for $\nu = 1$ which is

$$u_i^{n+1} = u_{i-1}^n \ .$$

Thus, for $\nu = 1$, the scheme properly convects waves along the characteristic dx/dt = a.

4.4 Stability Analyses

The stability of the scheme was analyzed using the classical von Neumann method [38]. In this method, the error is expressed as a Fourier series and the growth of the error in time is examined. The total error in a numerical calculation consists of both discretization error and round-off error. The discretization error arises from the fact that what one is actually solving in a numerical calculation is not a differential equation but a difference equation. If U(x,t) is taken to be the exact solution to the governing PDE and if $u(i\Delta x, n\Delta t)$ is the solution to the approximating difference equation carried out to infinite precision, then (U - u) is the discretization error. If this difference goes to zero as Δx goes to zero, then the difference equation is said to be consistent with the PDE.

Roundoff error arises from the fact that the calculations cannot, in practice, be carried out with infinite precision and the calculations must be rounded-off to some finite number of decimal places. If N is called the actual finite precision numerical solution, then (u - N) is the roundoff error and U - N is the sum of the discretization error and

the round-off error. The numerical calculations will be stable if the inevitable errors which are introduced are damped out (i.e. decay with time).

Although the von Neumann stability analyses is not the most rigorous method, since it ignores the boundary conditions, it is used frequently because one is usually interested in the stability of the basic scheme as boundary conditions may change. To examine the effect of the boundary conditions, the matrix method may be used [39]. In this method, it is necessary to define an amplification matrix A as

$$\underline{u}^{n+1} = A \underline{u}^{u}$$

where $\underline{u}^{n+1}$ and $\underline{u}^{n}$ are the vectors of the solution. Then the eigenvalues of A are examined, and for stability, it is necessary that the modulus of all the eigenvalues be less than one.

Stability analyses of the scheme were done in both one- and two-dimensions. For the one-dimensional analyses, the model Eq. (4.22) was used. For the two-dimensional stability analyses, the following model equation was used.

$$u_t + a u_x + b u_y = 0 \qquad\qquad (4.28)$$

It turns out that the maximum CFL number for which the scheme is stable is two for the one-dimensional equation and one for the two-dimensional model equation. The steps in the analyses will only be shown for the two-dimensional analyses.

The first step in the analyses is to combine the three steps of the Gabutti scheme into a single step so that $u_{i,j}^{n+1}$ is expressed in terms of the $u_{i,j}$ at time step n. When this is done, the result is

$$
\begin{aligned}
u_{i,j}^{n+1} = u_{i,j}^{n} - \frac{1}{2} [& \alpha(3 u_{i,j}^{n} - 4 u_{i-1,j}^{n} + u_{i-2,j}^{n}) \\
& + \beta(3 u_{i,j}^{n} - 4 u_{i,j-1}^{n} + u_{i,j-2}^{n}) \\
& + \alpha^2 (u_{i,j}^{n} - 2 u_{i-1,j}^{n} + u_{i-2,j}^{n}) \\
& + \beta^2 (u_{i,j}^{n} - 2 u_{i,j-1}^{n} + u_{i,j-2}) \\
& 2 \alpha \beta(u_{i,j} - u_{i-1,j} - u_{i,j-1} + u_{i-1,j-1})]
\end{aligned} \quad (4.29)
$$

where

$$\alpha = a \, \Delta x / \Delta t$$

$$\beta = b \, \Delta y / \Delta t$$

If e_i^n is assumed to be an initial error distribution and N_i^n is the solution to the difference equation which satisfies Eq. (4.29) exactly, then the error at time level n+1 must also satisfy Eq. (2.29). Thus, the error will not grow provided the solution to the difference equation is stable and bounded.

Next, assume that

$$u_i^n = r^n \exp [I (k_x i \, \Delta x + k_y j \, \Delta y)] \quad (4.30)$$

$$I = \sqrt{-1}$$

is a periodic representation of the solution with r^n as the amplitude, k_x and k_y as the wavenumbers, and $\theta_x = k_x \Delta_x$ and $\theta_y = k_y \Delta y$ as the phase angles. Substituting Eq. (4.30) into Eq. (4.29), is found that

$$r = \left| 1 - \frac{1}{2} \left[\alpha (3 - 3 \exp(-I\theta_x) + \exp(-2I\theta_x)) \right. \right.$$

$$+ \beta(3 - 3 \exp(-I\theta_y) + \exp(-2I\theta_y))$$

$$+ \alpha^2(1 - 2 \exp(-I\theta_x) + \exp(2I\theta_x))$$

$$+ \beta^2(1 - 2 \exp(-I\theta_y) + \exp(2I\theta_y))$$

$$+ \alpha \beta(2 - 2 \exp(-I\theta_x) - 2 \exp(-I\theta_y)$$

$$\left. \left. + \exp(-I(\theta_x + \theta_y)))\right]\right| . \tag{4.31}$$

Define the amplification factor as

$$u_i^{n+1} = G u_i^n \tag{4.32}$$

from which it is apparent that G is the same as r. The maximum amplification factor G for values of α and β ranging from .5 to 1.5 was found by solving Eq. (4.31) on a computer for values of α and β ranging from 0 to 360 degrees. The results are shown in Table 4.1. From this, it is seen that the scheme has a maximum CFL number for stability of one in two-dimensions.

Table 4.1 Results from Stability Analyses

α	β	G
.5	.5	1.0
.5	1.0	1.0
.5	1.5	1.0
1.0	1.0	1.0
1.0	1.5	3.5
1.5	1.5	7.0

Chapter 5

SCHEME 2 - SHOCK FITTING GABUTTI

5.1 Introduction

Shock fitting, in contrast to shock capturing, does not attempt to apply finite differencing across shock waves and instead imposes the correct Rankine-Hugoniot jump relations at the discontinuities, the location of which is assumed known. Shock fitting methods seem to have evolved alongside and in conjunction with shock capturing methods. Shock fitting is still frequently used in supersonic problems where a bow shock wave develops ahead of the body. The flow ahead of the shock is usually taken to be freestream uniform flow and so there is no need to apply the time-dependent method to this region. The jump relations are applied at the shock, which is fitted as a computational boundary. If all of the shocks in the flow field are fitted, then it can be argued that the governing equations can be solved numerically in either conservation or nonconservation form in the smooth regions of the flow field.

Thus, the use of shock fitting can lead to a reduction in computer time from (1) the elimination of the need to apply finite differencing to the freestream uniform flow ahead of the bow shock in supersonic problems and (2) the use of the primitive variable form of the governing equations which may be somewhat less expensive to solve numerically. However, the subsequent development of implicit methods has, to some

degree, removed the advantage of—solving the non-conservative equations because ultimately one is after the solution to the problem in the least amount of computer time and convergence rates are perhaps more relevant to this quest than the cost to do a single iteration.

In this study, the shock which develops, is embedded in the flow field and shock fitting is used on a grid which has the shock aligned with one of the lines of constant X (in the computational domain). The shock is allowed to move and adjust its position and characteristics to the evolving flow field. Recently, Moretti has shown that it is possible to do shock fitting on a grid which is stationary such that the shock is not aligned with any of the mesh lines [40]. This method has also been referred to as "front tracking" and is used to describe methods for handling discontinuities such as weather fronts and oil flow in porous media [41].

The shock fitting scheme developed for use in this investigation treats the embedded shock which develops as a discontinuity aligned with a line of constant X and the Rankine-Hugoniot relations are used to relate the upstream and downstream flows through the shock.

This scheme is identical to the scheme described in Chap. 4 with five exceptions. First, the initial conditions are the converged results of a previous run of scheme 1. Second, the grid is aligned with the embedded shock that forms in the initial run. Third, the governing equations along with the Rankine-Hugoniot relations are used to calculate the shock velocity and acceleration at each point on the shock front and the grid is dynamically adapted as the shock changes its position. Fourth, the Rankin-Hugoniot relations are used to calculate

the jumps in pressure, density, velocity and entropy through the shock, and fifth, the equation describing the convection of entropy is included with the set of equations to be solved

$$\frac{DS}{Dt} = S_t + u \, S_x + v \, S_y = 0 \; . \tag{5.1}$$

When Eq. (5.1) is transformed to (ξ, η) coordinates, it becomes

$$S_t + US_\xi + VS_\eta = 0 \tag{5.2}$$

where U and V are the contravarient velocity components. The entropy is related to the nondimensional pressure and density by Eq. (5.3)

$$S = \ell n \, p - \gamma \, \ell n \, \rho \; . \tag{5.3}$$

The unknowns in the final set of equations are the log of the pressure P, the velocity components U and V, and the entropy S. Since there are four equations, the system is closed.

5.2 Transformation to Shock Fitted Coordinates

The solution to be used as the initial condition to the shock fitting calculations is associated with some curvilinear coordinates ξ and η which, in general, are not aligned with the shock. The solution must, therefore, be interpolated onto a new coordinate system which is aligned with the shock. These coordinates will be called X an Y herein and the transformation from the previous to the new coordinate system is given as

$$(t, \xi, \eta) \; \rightarrow \; (T, X, Y) \; .$$

The transformation relations to be used will have $X = X(t, \xi, \eta)$ and $Y = Y(t, \eta)$ and, therefore, by the chain rule.

$$\frac{\partial}{\partial t} = \frac{\partial}{\partial T} + \frac{\partial}{\partial X} X_t + \frac{\partial}{\partial Y} Y_t$$

$$\frac{\partial}{\partial \xi} = \frac{\partial}{\partial X} X_\xi \qquad\qquad (5.4)$$

$$\frac{\partial}{\partial \eta} = \frac{\partial}{\partial X} X_\eta + \frac{\partial}{\partial Y} Y_\eta \quad .$$

The system of governing equations which results is

$$P_T + \bar{U} P_X + \bar{V} P_Y + \gamma [U_X X_\xi + V_X X_\eta + Y_Y Y_\eta] = P_s$$

$$U_T + \bar{U} U_X + \bar{V} U_Y + \frac{(Ja)^2}{\gamma} [g_2 P_X X_\xi - g_3 (P_X X_\eta + P_Y Y_\eta)] = U_s \qquad (5.5)$$

$$V_T + \bar{U} V_X + \bar{V} V_Y + \frac{(Ja)^2}{\gamma} [g_1 (P_X X_\eta + P_Y Y_\eta) - g_3 P_X X_\xi] = V_s$$

$$S_T + \bar{U} S_X + \bar{V} S_y = 0$$

where

$$\bar{U} = X_t + U X_\xi + V X_\eta$$

$$\bar{V} = Y_t + V Y_\eta$$

and P_s, U_s and V_s are as previously defined in Eqs. (4.7c) and (4.12c and d).

The desired coordinate transformation in the ξ direction is

$$X = X(\xi_s)$$

where ξ_s is the location of the shock which is function of η and t. A second degree polynomial given as

$$\xi = \xi_0 + (\xi_1 - \xi_0)(a_1 X + a_2 X^2) \tag{5.6}$$

was used where ξ_0 and ξ_1 represent the minimum and maximum values of ξ and a_1 and a_2 are coefficients determined such that

$$\xi = \xi_s \quad \text{when} \quad X = X_s$$

$$\xi = \xi_1 \quad \text{when} \quad X = X_1 .$$

It is easily found that

$$a_1 = b_1 + b_2 f$$

$$\tag{5.7}$$

$$a_2 = b_3 + b_4 f$$

where

$$b_1 = -X_s/(X_1 D)$$

$$b_2 = X_1/(X_s D)$$

$$b_3 = -b_1/X_s$$

$$b_4 = -b_2/X_1$$

$$D = X_1 - X_s$$

$$f = \frac{\xi_s - \xi_0}{\xi_1 - \xi_0} .$$

Using the above expressions, the transformation Eqs. (5.8) are determined as

$$X_\xi = 1/[(\xi_1 - \xi_0)(a_1 + 2 a_2 X)]$$

$$X_\eta = -(b_2 X + b_4 X^2) X_\xi f_\eta \tag{5.8}$$

$$X_t = -(b_2 X + b_4 X^2) X_\xi f_t .$$

A transformation from η to Y was done for problems 1, 2, and 3. Since ξ and η are conformal coordinates and are independent of the stretchings used to produce the original grid, then it is necessary to use some sort of transformation from η to Y if it is desired to have $\Delta Y = 1$. A second order stretching was used as follows

$$\eta = \eta_0 + (\eta_1 - \eta_0) (a_4 Y + a_5 Y^2) \qquad (5.9)$$

where η_0 and η_1 are the minimum and maximum values of η and a_4 and a_5 are coefficients chosen to achieve the desired stretching. In problem 1, η_0, a_4 and a_5 were made to be functions of time so that the position of the lower boundary as well as the degree of clustering near the lower boundary could be changed dynamically.

5.3 Calculation of Shock Acceleration[1]

To calculate the shock acceleration, the governing equations are used along with the Rankine-Hugoniot relations in a fairly straight forward manner. First, the governing equations are written in vector form as

$$0_t + A 0_x = R \qquad (5.10)$$

$$0 = [P, U, V]^T$$

---

[1]The writer is indebted to Mr. M. D. Salas for showing how to calculate the shock acceleration.

where

$$A = \begin{bmatrix} -\bar{U} & \gamma X_\xi & \gamma X_\eta \\ \frac{(Ja)^2}{\gamma}(g_2 X_\xi - g_3 X_\eta) & \bar{U} & 0 \\ \frac{(Ja)^2}{\gamma}(g_1 X_\eta - g_3 X_\xi) & 0 & \bar{U} \end{bmatrix}$$

$$R = [R_1, R_2, R_3]^T$$

$$R_1 = P_s - V P_\gamma - \gamma U_\gamma$$

$$R_2 = U_s - V U_\gamma + \frac{(Ja)^2}{\gamma} g_3 P_\gamma$$

$$P_3 = V_s - V V_\gamma - \frac{(Ja)^2}{\gamma} g_1 P_\gamma \; .$$

The matrix A has the eigenvalues

$$\lambda_1 = \bar{U} - \tilde{a}$$

$$\lambda_2 = \bar{U} + \tilde{a}$$

$$\lambda_3 = \bar{U}$$

$$\tilde{a} = Ja \left[g_1 X_\eta^2 - 2 g_3 X_\xi X_\eta + g_2 X_\xi^2 \right]^{1/2}$$

$$= Ja \left[SQ \right]^{1/2}$$

and can be diagonalized as

$$A = S \Lambda S^{-1}$$

where

$$S = \begin{bmatrix} \frac{\gamma}{Ja} SQ & \frac{\gamma}{Ja} SQ & 0 \\ g_3 X_\eta - g_2 X_\xi & g_2 X_\xi - g_3 X_\eta & X_\eta \\ g_3 X_\xi - g_1 X_\eta & g_1 X_\eta - g_3 X_\xi & -X_\xi \end{bmatrix}$$

and SQ is the quantity in square -foots. Equation (5.10) can be put into characteristic form as

$$S^{-1} Q_t + \Lambda S^{-1} Q_X = S^{-1} R \quad .$$

<div align="right">(5.11)</div>

The equation corresponding to λ_1 is then

$$P_t + P_X^- + \beta_2 (U_T + \lambda^- U_X^-) + \beta_3 (V_T + \lambda^- V_X^-)$$

$$= R_1 + \beta_2 R_2 + \beta_3 = R_4$$

<div align="right">(5.12)</div>

where

$$\beta_2 = -\gamma X_3 / \tilde{a}$$

$$\beta_3 = -\gamma X_\eta / \tilde{a}$$

and P_X^-, U_X^- and V_X^- are forward differences.

Figure 5.1 shows the shock in the (ξ, η) coordinate system with unit normal and tangent vectors. The covariant base vectors are

$$\vec{e}_\xi = X_\xi \, \bar{i} + y_\xi \, \bar{j}$$

$$\vec{e}_\eta = X_\eta \, \bar{i} + Y_\eta \, \bar{j} \quad .$$

<div align="right">(5.13)</div>

The contravariant base vectors are

$$\vec{e}^\xi = \xi_x \, \bar{i} + \xi_y \, \bar{j}$$

$$\vec{e}^\eta = \eta_x \, \bar{i} + \eta_y \, \bar{j} \quad .$$

<div align="right">(5.14)</div>

The unit normal at the shock is given by
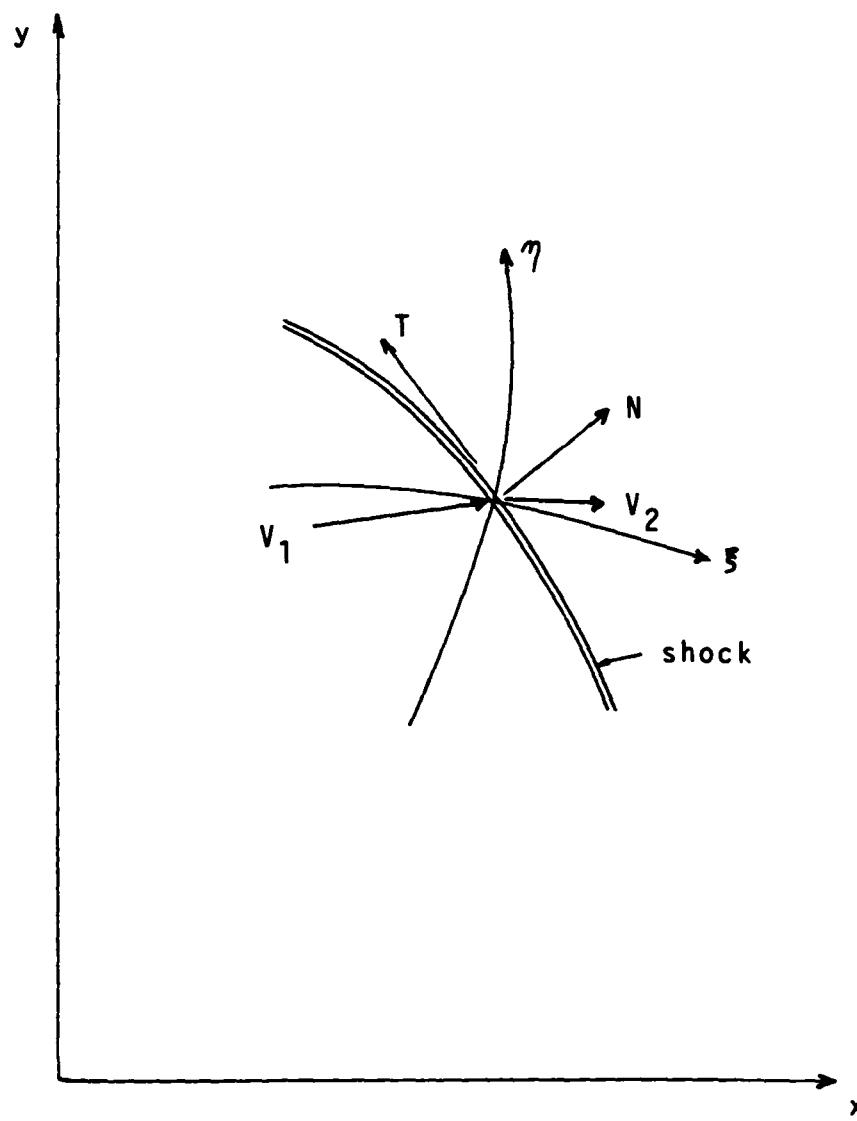
Fig. 5.1 Vector Relations at the Shock.

$$\bar{N} = \frac{\nabla f}{|\nabla f|}$$

$$= \frac{f_x \vec{i} + f_y \vec{j}}{\sqrt{f_x^2 + f_y^2}}$$

$$= \frac{f_\xi \vec{e}^\xi + f_\eta \vec{e}^\eta}{\sqrt{\nabla f \cdot \nabla f}} \qquad (5.15)$$

where

$$f = \xi - \xi_s(\eta, t) = 0 \qquad (5.16)$$

and the length of grad f is

$$|\nabla f| = [f_\xi^2 \vec{e}^\xi \cdot \vec{e}^\xi + 2 f_\xi f_\eta \vec{e}^\xi \cdot \vec{e}^\eta + f_\eta^2 \vec{e}^\eta \cdot \vec{e}^\eta]^{1/2}$$

$$= h_n .$$

The unit tangent vector is defined by

$$\bar{N} \cdot \bar{T} = 0$$

and therefore it is found that

$$\bar{T} = \frac{- f_\eta \vec{e}_\xi + f_\eta \vec{e}_\eta}{[f_\eta^2 \vec{e}_\xi \cdot \vec{e}_\xi - 2 f_\xi f_\eta \vec{e}_\xi \cdot \vec{e}_\eta + f_\xi^2 \vec{e}_\eta \cdot \vec{e}_\eta]^{1/2}}$$

$$= \frac{\xi_{s_\eta} \vec{e}_\xi + \vec{e}_\eta}{h_t} \qquad (5.16)$$

where ξ_{s_η} is the shock slope and h_t is the square root term above.

The velocity relations at the shock are obtained using these equations. The flowfield velocity is

$$\vec{V} = u\,\vec{i} + v\,\vec{j}$$

$$= U\,\vec{e}_\xi + V\,\vec{e}_\eta . \tag{5.17}$$

Letting the contravariant velocity of the shock be U_s, the velocity relative to the shock is

$$\vec{V}_s = (U - U_s)\,\vec{e}_\xi + V\,\vec{e}_\eta . \tag{5.18}$$

Note that U and V are different on each side of the shock. The velocity component normal to the shock is

$$\vec{V}_s \cdot \vec{N} = \frac{(U - U_s) - \xi_{s_\eta} V}{h_n} .$$

$$= V_n \tag{5.19}$$

The component tangent to the shock is

$$\vec{V}_s \cdot \vec{T} = \frac{\xi_{s_\eta}(U - U_s) + V}{h_t}$$

$$= V_t . \tag{5.20}$$

Since the tangential components of velocity must be equal on both sides of the shock, we have

$$U_1\,\xi_{s_\eta} + V_1 = U_2\,\xi_{s_\eta} + V_2 \tag{5.21}$$

where the subscripts 1 and 2 denote the upstream and downstream sides of the shock respectively. Equations (5.19) and (5.20) can be solved for U and V to get

$$U = U_s + \frac{V_n h_n + \xi_{s_\eta} V_t h_t}{1 + \xi_{s_\eta}^2} \tag{5.22}$$

$$V = \frac{V_t h_t - \xi_{s_\eta} V_n h_n}{1 + \xi_{s_\eta}^2} . \tag{5.23}$$

The jump in pressure through the shock is given by

$$\frac{p_2}{p_1} = 1 + \frac{2\gamma}{\gamma + 1}(M_1^2 - 1) = p_r \tag{5.24}$$

where M_1 is the Mach number relative to the shock and is given by

$$M_1 = \frac{\bar{V}_{s_1} \cdot \bar{N}}{a_1} = \frac{(U_1 - U_s) - \xi_{s_\eta} V_1}{a_1 h_n} . \tag{5.25}$$

Equation (5.24) can be expressed in terms of the log of p as

$$P_2 = P_1 + \ell n \, (p_r) .$$

The derivative of P_2 with respect to time is then

$$P_{2_t} = P_{1_t} + \frac{1}{p_r}\left(\frac{4\gamma}{\gamma + 1}\right) M_1 M_{1_t} . \tag{5.26}$$

The term M_{1_t} is equal to

$$M_{1_t} = c_1 + c_2 U_{s_t} \tag{5.27}$$

where U_{s_t} is the shock acceleration and c_1 and c_2 are coefficients found to be

$$c_1 = \frac{U_{1_t} - \xi_{s_n} V_1 - \xi_{s_n} V_{1_t}}{a_1 h_n} - M_1 \left(\frac{a_{1_t}}{a_1} + \frac{h_{n_t}}{h_n} \right)$$

$$c_2 = - \frac{1}{a_1 h_n} .$$

Substituting Eq. (5.27) into Eq. (5.26) and rearranging gives

$$P_{2_t} = b_1 + b_2 U_{s_t} \tag{5.28}$$

where

$$b_1 = P_{1_t} + \frac{1}{P_r} \left(\frac{4\gamma}{\gamma + 1} \right) M_1 C_1$$

$$b_2 = \frac{1}{P_r} \left(\frac{4\gamma}{\gamma + 1} \right) M_1 c_2 .$$

The jump in the normal component of velocity relative to the shock is given by

$$\frac{\vec{V}_{s_1} \cdot \bar{N}}{\vec{V}_{s_2} \cdot N} = u_r = \frac{U_2 - U_s - \xi_{s_n} V_2}{U_1 - U_s - \xi_{s_n} V_1} . \tag{5.29}$$

Using Eqs. (5.21) and (5.29), the contravariant component U_2 is found to be

$$U_2 = \frac{U_s + V_1 \xi_{s_n} + U_1 \xi_{s_n}^2 + u_r (U_1 - U_s - V_1 \xi_{s_n})}{1 + \xi_{s_n}^2} \tag{5.30}$$

where the jump in velocity through the shock u_r is given by

$$u_r = \frac{(\gamma - 1) M_1^2 + 2}{(\gamma + 1) M_1^2} \ . \tag{5.31}$$

The time derivative of Eq. (5.30) is then found to be

$$U_{2_t} = b_3 + b_4 U_{s_t} \tag{5.32}$$

where

$$b_3 = [V_{1_t} \xi_{s_n} + V_1 \xi_{s_{n_t}} + U_{1_t} \xi_{s_n}^2 + 2U_1 \xi_{s_n} \xi_{s_{n_t}}$$

$$+ c_3 (U_1 - U_s - V_1 \xi_{s_n}) + u_r(U_{1_t} - V_{1_t} - V_1 \xi_{s_{n_t}})$$

$$- 2U_2 \xi_{s_n} \xi_{s_{n_t}}]/(1 + \xi_{s_n}^2)$$

$$b_4 = [1 + c_4(U_1 - U_s - V_1 \xi_{s_n}) - u_r]/(1 + \xi_{s_n}^2)$$

$$c_3 = - 4 c_1/(\gamma + 1) M_1^3)$$

$$c_4 = c_3 c_2/c_1 \ .$$

In a similar manner, taking the time derivative of Eq. (5.21) leads to the following expression for V_{2_t}.

$$V_{2_t} = b_5 + b_6 U_{s_t} \tag{5.33}$$

where

$$b_5 = V_{1_t} + (U_1 - U_2) \xi_{s_{n_t}} + (U_{1_t} - b_3) \xi_{s_n}$$

$$b_6 = - b_4 \xi_{s_n} \ .$$

Finally, substituting all of these expressions into Eq. (5.12) and solving for U_{s_t} gives

$$U_{s_t} = \frac{R_4 - b_1 - \lambda^- P_x^- - \beta_2(b_3 + \lambda^- U_x^-) - \beta_3(b_5 + \lambda^- V_x^-)}{b_2 + \beta_2 b_4 + \beta_3 b_6} \ . \qquad (5.34)$$

Thus an expression has been obtained for the shock acceleration. The shock position is then updated using the shock acceleration to update the shock velocity as described next.

5.4 Updating the Shock Position

The method used to update the shock position was arrived at after extensive experimentation. It was discovered early that the calculation of shock acceleration and the jumps in fluid density, velocity, pressure, and energy through the shock are all very sensitive to the shock velocity and the slope of the shock with respect to the oncoming flow. If each point along the shock is computed independently of the others, wiggles and oscillations tended to develop in the shape of the shock which quickly destroyed the calculations. In order to prevent this from occurring, polynomial least squares smoothing was introduced.

A related problem which had to be addressed was how to update the grid above the shock. Since no acceleration is computed for the points above the shock along the line of constant ξ which aligns with the shock, some artificial means had to be introduced to move these points so the grid would not have a discontinuity in it.

The first step in updating the shock position is to smooth the computed shock accelerations computed from $J = 1$ to $J = JS$, the last

shock point. This was done by a weighted least squares approximation to the function values at the JS points using orthogonal polynomials [42]. Then, using the smoothed values of the shock acceleration, the updated shock velocities and positions were computed in a three-step predictor-corrector manner analogous to the Gabutti scheme.

In the first step, the following loop is executed

Do from $J = 1$ to $J = JS$

$$XSTN(J) = XST(J) + XSTT(J) * \Delta t$$

(5.35)

$$XSN(J) = XS(J) + XSTN(J) * \Delta t$$

where XS, XST, and XSTT are the shock position, velocity, and the acceleration at the beginning of the time step and XSN and XSTN are the predicted values of the shock position and acceleration. The predicted values of XSN are then smoothed using orthogonal polynomials up to degree three as shown in Fig. 5.2a.

The points above the shock along the connecting line from $J = JS + 1$ to $J = JMAX$ must now be computed and this was done as follows. First, XSN at the top boundary ($J = JM$) was determine as

$$XSN(JM) = .9 * XSO(JM) + .1 * XSN(JS) .$$

(5.36)

This insures that eventually XS(JM) will equal XS(JS) and that the top end of the connecting line will not move too rapidly. Next, the points in between XSN(JS) and XSN(JM) are calculated as

$$XSN(J) = (1 - 3H^2 - H^3) * XSN(JS)$$

$$+ (3H^2 - 2H^3) + XSN(JM)$$

(5.37)

where
$$H = (n_J - n_{JS})/(n_{JM} - n_{JS}) \;\;.$$

This insures that the slope of the connecting curve ξ_{s_n} is zero at $J =$ JS and $J = $ JM as shown in Fig. 5.2b. Finally, the points XSN from $J = 1$ to $J = $ JS are smoothed to blend the connecting curve with the shock as shown in Fig. 5.2c. The smoothing this time is done by orthogonal polynomials up to degree four.

In the second step of the Gabutti scheme, the shock accelerations are again calculated at each point then smoothed by second degree orthogonal polynomials and stored as XSTTS. The predicted values of the shock position and the points along the connecting curve are now substituted for the original values of XS.

In the third step, the same procedure is followed as in the first step except the calculated values of the shock acceleration are first smoothed and then combined with the predicted values from step two as follows

$$XSTT(J) = \frac{1}{2} (XSTT(J) + XSTTS(J)) \;\;.$$

This follows the same predictor-corrector sequence as the Gabutti scheme used in the updating routine and is thus consistent with the rest of the scheme. At the end of the third step, the newly corrected values of the shock (and connecting line) position and velocity, XS and XST, are substituted for the old values.
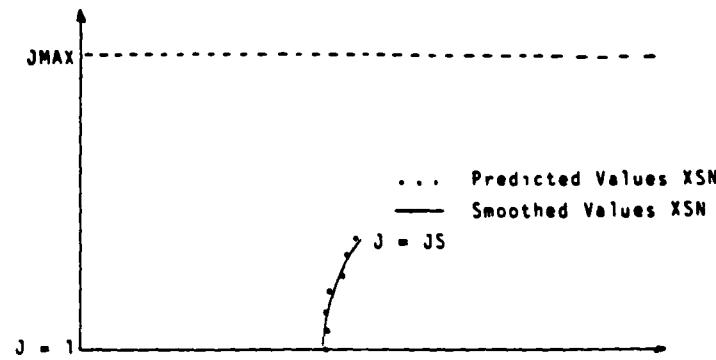
(a) Calculation of XSN to J = JS
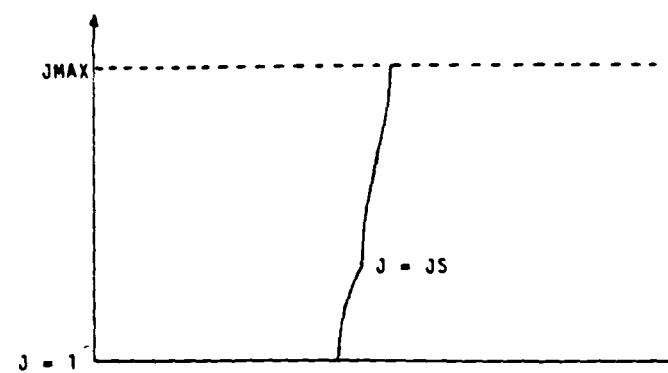
(b) Calculation of XSN from J = JS+1 to JMAX
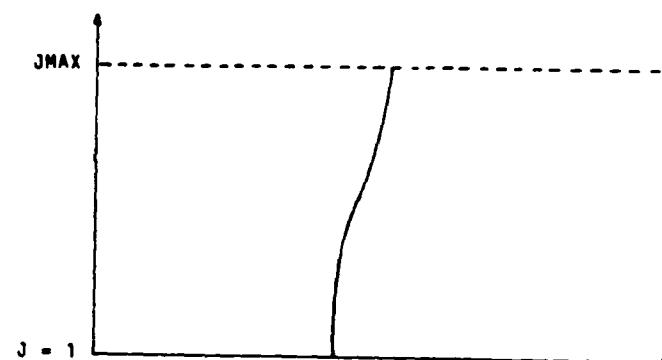
(c) Blending of XSN from JWALL to JMAX

Fig. 5.2 Construction of Line I = IS.

Chapter 6

SCHEME 3 - FLUX VECTOR SPLITTING EULER

6.1 Introduction

The schemes described in Chaps. 4 and 5, when used together, will produce an accurate resolution of the flow field and will give the correct jump relations through shock waves. However, the schemes have several disadvantages which limit their utility. First, shock fitting is not a technique which is easily implemented and the need for adaptive gridding adds to the computer run times and complicates the coding. Second, since the governing equations are not solved in conservation form, there is no guarantee that mass or momentum is conserved throughout the flowfield. Third, since the equations are solved explicitly, there is a restriction to low maximum allowable CFL numbers and as a result covergence to a steady state is slow. It was this restriction which applies to all explicit schemes which led to the development of implicit schemes in the late 1970's. The CFL restriction on the Lambda algorithm was removed several years ago with the introduction of implicit Lambda schemes by Dadone and Napolitano [43] and Dadone and Magi have developed a "quasi-conservative" Lambda formulation [44].

The scheme described in this chapter is an approximate factorization scheme which was developed by von Lavante. The scheme is implicit and solves the governing equations in conservation form. The

scheme is described in Ref. [45] as the "true Jacobian scheme" which refers to the implicit operator which is used.

6.2 Algorithm Development

The two-dimensional, unsteady, compressible Euler equations in conservation form are

$$Q_t + F_x + G_y = 0 \tag{6.1}$$

where

$$Q = [\rho, \rho u, \rho v]^T$$

$$F = [\rho u, \rho u^2 + p, \rho u v]^T$$

$$G = [\rho v, \rho u v, \rho v^2 + p]^T$$

As was the case in Scheme 1, the pressure is related to the density and the velocities by the steady state energy equation

$$\frac{a^2}{\gamma - 1} + \frac{u^2 + v^2}{2} = h_t \tag{6.2}$$

$$a^2 = \frac{\gamma p}{\rho} \tag{6.3}$$

These equations are nondimensionalized as follows

$$x' = x/L, \quad y' = u/L, \quad u' = u/a_0, \quad v' = v/a_0$$

$$\rho' = \rho/\rho_0, \quad p' = p/\gamma a_0^2, \quad h_t' = h_t/a_0^2$$

Equations (6.2) and (6.3) then become

$$\frac{a'^2}{\gamma-1} + \frac{u'^2 + v'^2}{2} = \frac{1}{\gamma-1} \tag{6.4}$$

$$a'^2 = \frac{\gamma p'}{\rho'}$$

The algorithm to solve Eq. (6.1) first does a time discretization of the vector Q by a truncated Taylor series as follows

$$Q^{n+1} = Q^n + \frac{\partial Q^{n+1}}{\partial t} \Delta t + 0 (\Delta t^2) \tag{6.5}$$

Let $\Delta Q = Q^{n+1} - Q^n$ and express the time derivative of Q^{n+1} by another Taylor approximation and Eq. (5.5) becomes

$$\Delta Q = \Delta t \left(\frac{\partial Q^n}{\partial t} + \Delta t \frac{\partial}{\partial t} \left(\frac{\partial Q^n}{\partial t}\right)\right) + 0 (\Delta t^2)$$

Using Eq. (6.1), this becomes

$$\Delta Q = -\Delta t \left[(F_x^n + G_y^n) + \Delta t \frac{\partial}{\partial t} (F_x^n + G_y^n)\right] \tag{6.6}$$

The conservation form of the Euler equations has the property that the flux vectors F and G are homogeneous functions of degree one of the vector Q. This means that

$$F = AQ \quad \text{and} \quad G = BQ \tag{6.7}$$

where A and B are the Jacobian matrices $\partial F/\partial Q$ and $\partial G/\partial Q$ respectively. These matrices are given below

$$A = \frac{1}{2\rho}\begin{bmatrix} 0 & 1 & 0 \\ (\beta v^2 - (\gamma+1)u^2) & \frac{\gamma+1}{\gamma} u & \frac{1-\gamma}{\gamma} v \\ -uv & v & u \end{bmatrix} \tag{6.8a}$$

$$B = \frac{1}{2\rho} \begin{bmatrix} 0 & 0 & 1 \\ -uv & v & u \\ (\beta u^2 - (\gamma+1)v^2) & \frac{1-\gamma}{\gamma} u & \frac{\gamma+1}{\gamma} v \end{bmatrix} \qquad (6.8b)$$

Equation (6.6), after some manipulation, can be expressed in operator form as

$$[I + \Delta t \left(\frac{\partial A}{\partial x} + \frac{\partial B}{\partial y}\right)] \Delta Q = -\Delta t \left(\frac{\partial F}{\partial x} + \frac{\partial G}{\partial y}\right) \qquad (6.9)$$

This equation can be approximately factored as

$$[I + \Delta t \frac{\partial A}{\partial x}] [I + \Delta t \frac{\partial B}{\partial y}] \Delta Q = -\Delta t \left(\frac{\partial F}{\partial x} + \frac{\partial G}{\partial y}\right)$$

$$= R^n \qquad (6.10)$$

Equation (6.10) is solved in three steps as follows. First, the right hand side of (6.10) is found using the flux-vector splitting as described in the next section. Then, ΔQ is found in two steps as follows

$$[I + \Delta t \frac{\partial A}{\partial x}] \tilde{Q} = R^n$$
$$[I + \Delta t \frac{\partial B}{\partial y}] \Delta Q = \tilde{Q} \qquad (6.11)$$

Finally, Q is updated.

$$Q^{n+1} = Q^n + \Delta Q$$

Generally, block tridiagonal matrix inversions must be used to solve Eq. (6.11). Equation (6.10) can also be transformed from cartesian to general coordinates

$$[I + \Delta t \frac{\partial \tilde{A}}{\partial \xi}] \ [I + \Delta t \frac{\partial \tilde{B}}{\partial \eta}] \ \Delta \tilde{Q} = -\Delta t (\tilde{F}_\xi + \tilde{G}_\eta) \tag{6.12}$$

where

$$\tilde{Q} = Q/J$$

$$\tilde{F} = \xi_x F + \xi_y G$$

$$\tilde{G} = \eta_x F + \eta_y G$$

$$\frac{1}{J} = x_\xi y_\eta - x_\eta y_\xi$$

Since the Euler equations are hyperbolic, the Jacobian matrices $\tilde{A}$ and $\tilde{B}$ can be diagonalized by the following similarity transformations

$$\tilde{A} = M \Lambda_A M^{-1}$$

$$\tilde{B} = N \Lambda_B N^{-1} \tag{6.13}$$

where M and and N are the right eigenvector matrices and Λ_A and Λ_B are the diagonal matrices of the eigenvalues. It can be shown by examining the equations in primitive variable form that the eigenvalues of A are

$$\lambda_1 = u$$

$$\lambda_2 = u(\gamma+1)/2\gamma + SQ \tag{6.14}$$

$$\lambda_3 = u(\gamma+1)/2\gamma - SQ$$

where

$$SQ = [(u(\gamma-1)/2\gamma)^2 + a^2/\gamma]^{1/2}$$

In Refs. 46 and 47, von Lavante describes how the Jacobian matrices can be diagonalized to permit even greater computational simplification.

6.3 Flux-Vector Splitting

The flux vectors F and G are each split into forward (+) and backward (-) fluxes by a method introduced by van Leer [48]. To use the flux vector F as an example (the requirements for G are the same), the flux F is split as

$$F(Q) = F^+(Q) + F^-(Q) \qquad (6.15)$$

The second requirement is that

$$A^+ = \partial F^+/\partial Q \quad \text{have all eigenvalues} > 0$$

$$A^- = \partial F^-/\partial Q \quad \text{have all eigenvalues} < 0$$

The flux-split components F^+ and F^- must be continuous and satisfy

$$F^+ = F \quad \text{for Mach No. } M > 1$$

$$F^- = F \quad \text{for} \qquad M < -1.$$

The components are further required to correctly model the symmetry of F with respect to the Mach No. M such that

$$F^+(M) = \pm F^-(-M) \quad \text{if} \quad F(M) = \pm F(-M)$$

The split Jacobian matrices A^+ and A^- must be continuous at sonic and stagnation points. This requirement is important as other types of splittings do not accomplish this and these splittings produce oscillations when the eigenvaluve change signs. Next, it is required that for subsonic flow, A^+ and A^- must each have one eigenvalue vanish. This requirement makes it possible to capture shocks with no more than two interior cells. Van Leer satisfies these requirements by appropriate choices of polynomials to represent F(M) and G(M).

6.4 Spatial Discretization

The right hand side of Eq. (6.12) can be integrated over a finite volume which consists of the interior of the quadrilateral cell with the grid points at (i, j), (i-1, j), (i, j-1), and (i-1, j-1). Thus, using Green's Theorem, we have

$$\Delta \tilde{Q}_e = -\Delta t \int_A (\tilde{F}_\xi + \tilde{G}_\eta) \, dA$$

$$= -\Delta t \int_C \tilde{F} \, d\eta - \tilde{G} \, d\xi \tag{6.16}$$

The line integral above can be approximated as

$$\Delta \tilde{Q}_e = -\Delta t \, \{\tilde{F}_{i,j-1/2} - \tilde{F}_{i-1,j-1/2}$$

$$+ \quad \tilde{G}_{i-1/2,j} - \tilde{G}_{i-1/2,j-1}\} \tag{6.17}$$

where, for example, $\tilde{F}_{i,j-1/2}$ is the flux of $\tilde{F}$ through the cell face with midpoint $(i,j-1/2)$. Since the flux F is split into F^+ and F^-, each component must be evaluated at the appropriate cell face. The method used to evaluate the fluxes is the MUSCL type differencing of van Leer [49]. In this approach, the fluxes are extrapolated to the cell faces according to the signs of the eigenvalues. Thus

$$F^+_{i+1/2} = (3 \, F^+_i - F^+_{i-1})/2$$

$$\tag{6.18}$$

$$F^-_{i+1/2} = (3 \, F^-_{i+1} - F^-_{i+2})/2$$

The values of Q, F and G in cell_(i,j) are considered as representative cell averages.

In the implicit operator (i.e the left hand side) of Eq. (6.12), the Jacobian matrices $\tilde{A}$ and $\tilde{B}$ are also split such that

$$\tilde{A}^+ = \partial\tilde{F}^+/\partial Q$$

$$\tilde{A}^- = \partial\tilde{F}^-/\partial Q$$

Equation (6.12) thus becomes

$$[I + \Delta t(\partial_\xi \tilde{A}^+ + \partial_\xi \tilde{A}^-)] \; [I + \Delta t(\partial_\eta \tilde{B}^+ + \partial_\eta \tilde{B}^-)] \; \Delta Q = RHS \quad (6.19)$$

The derivatives in Eq. (6.19) are taken as one-sided forward or backward differences depending upon the sign. Thus for example

$$[I + \Delta t(\partial_\eta \tilde{B}^+ + \partial_\eta \tilde{B}^-)] \; \Delta Q = \Delta Q_i + \Delta t(A_i^+ \Delta Q_i - A_{i-1}^+ \Delta Q_{i-1})$$
$$+ \Delta t(\bar{A}_{i+1} \Delta Q_{i+1} - \bar{A}_i \Delta Q_i) \quad (6.20)$$

The form of Eq. (6.20) results in block tridiagonal matrix inversions to solve. As the steady state is approached, both sides approach zero, the first order accuracy on the left hand side of (6.18) does not affect the accuracy of the right hand side which is second order.

Chapter 7

SCHEME 4 - UPWIND NAVIER-STOKES

7.1 Introduction

The full compressible Navier-Stokes equations were solved using an upwind approximate factorization scheme for test problems 1 and 2. The code developed by Rumsey of NASA Langley, is fully vectorized to run on the CDC VPS 32 supercomputer, and is accurate for unsteady flows [50]. Both the laminar and Reynolds averaged turbulent Navier-Stokes equations were solved. A Baldwin-Lomax turbulence model was used and the Reynolds number was varied from 10,000 to 100,000.

7.2 Governing Equations

The full set of conservation equations in two-dimensions includes conservation of mass, conservation of momentum and conservation of energy. The momentum equations are the compressible Navier-Stokes equations as derived in Chap. 3. In vector form, the equations are

$$\tilde{Q}_t + \tilde{F}_\xi + \tilde{G}_\eta = \frac{1}{R_e} (\tilde{R}_\xi + \tilde{S}_\eta) \tag{7.1}$$

where $\tilde{Q}$, $\tilde{F}$, $\tilde{G}$, $\tilde{R}$ and $\tilde{S}$ are

$$\tilde{Q} = Q/J$$

$$\tilde{F} = (\xi_x F + \xi_y G)/J$$

$$\tilde{G} = (n_x \bar{-F} + n_y \, G)/J$$

$$\tilde{R} = (\xi_x \, R + \xi_y \, S)/J$$

$$\tilde{S} = (n_x \, R + n_y \, S)/J$$

and Q, F and G are given by

$$Q = [\rho, \rho u, \rho v, e]^T$$

$$F = \begin{bmatrix} \rho u \\ \rho u^2 + p \\ \rho uv \\ (e + p) \, u - kT_x \end{bmatrix}$$

$$G = \begin{bmatrix} \rho v \\ \rho uv \\ \rho v^2 + p \\ (e + p) \, v - kT_y \end{bmatrix}$$

R and S are given below as

$$R = [0, \tau_{xx}, \tau_{xy}, R_4]^T$$

$$S = [0, \tau_{xy}, \tau_{yy}, S_4]^T$$

where the components of R and S are

$$\tau_{xx} = (\lambda + 2\mu) \, (\xi_x \, u_\xi + n_x \, u_n) + \lambda(\xi_y \, v_\xi + n_y \, v_n)$$

$$\tau_{yy} = (\lambda + 2\mu) \, (\xi_y \, v_\xi + n_y \, v_n) + \lambda(\xi_x \, u_\xi + n_x \, u_n)$$

$$\tau_{xy} = \mu(\xi_y \, u_\xi + n_y \, u_n + \xi_x \, v_\xi + n_x \, v_n)$$

$$R_4 = u \, \tau_{xx} + v \, \tau_{xy} + \mu(\xi_x \, T_\xi + n_x \, T_n)/[Pr(\gamma-1)]$$

$$S_4 = u \, \tau_{xy} + v \, \tau_{yy} + \mu(\xi_y \, T_\xi + n_y \, T_n)/[Pr(\gamma-1)]$$

The Stokes hypothesis that $-\lambda = -\frac{2}{3}\mu$ is assumed and the Prandtl numbers is taken as a constant.

7.3 Numerical Algorithm

Equation (7.1) is solved using upwind approximate factorization as described in references 29 and 50. The algorithm is given as

$$[I + \Delta t(\partial_\xi^- \tilde{A}^+ + \partial_\xi^+ \tilde{A}^-) - R_e^{-1} \Delta t \, \partial_\xi (\tilde{M}/J)]$$

$$\times [I + \Delta t(\partial_\eta^- \tilde{B}^+ + \partial_\eta^+ \tilde{B}^-) - R_e^{-1} \Delta t(\partial_\eta (\hat{N}/J)] \Delta \tilde{Q}^n \qquad (7.2)$$

$$= -\Delta t \, R^n$$

$$R^n = \partial_\xi^- \tilde{F}^+ + \partial_\xi^+ \tilde{F}^- + \partial_\eta^- \tilde{G}^+ + \partial_\eta^+ \tilde{G}^-$$

$$- R_e^{-1} (\partial_\xi \tilde{R} + \partial_\eta \tilde{S}) \qquad (7.3)$$

and where as before

$$A^\pm = \frac{\partial F^\pm}{\partial Q}$$

$$B^\pm = \frac{\partial G^\pm}{\partial Q}$$

A and B are the Jacobian matrices given as Eqs. (6.8a) and (6.8b) and

$$\tilde{A} = \xi_x A + \xi_y B$$

$$\tilde{B} = \eta_x A + \eta_y B$$

The (+) and (-) superscripts on the F and 6 terms indicates the flux splitting which is done according to van Leer [48]. The (+) and (-) supescripts on the partial derivatives terms denotes the direction of differentiation. Thus, for example, ∂_ξ^- is a backward difference,

while ∂_ξ^+ is a forward difference. All viscous terms are centrally differenced. The $\tilde{M}$ and $\tilde{N}$ matrices are linearized viscous terms and are given by Steger in reference [51]. The scheme is first order accurate in time and second order accurate in space.

7.4 Turbulence Model

The turbulence model that is used in this scheme is a two layer algebraic eddy viscosity model developed by Baldwin and Lomax [52]. The model computes an eddy viscosity μ_t which is then added to the molecular viscosity μ to get the total viscosity. The model follows from a previous model developed by Cebeci [53] but avoids the necessity for finding the edge of the boundary layer. It has been shown to give good results in separated flows and in wake regions.

In the inner layer μ_t is computed as

$$\mu_t = \rho \, \ell^2 \, |\omega| \tag{7.4}$$

The length ℓ is obtained using the van Driest formulation as follows

$$\ell = \kappa_y [1 - \exp(- y^+/A^+)] \tag{7.5}$$

κ is the von Karman constant equal to .4, y^+ is the non-dimensional wall unit

$$y^+ = y(\tau_w \rho)^{.5}/\mu \tag{7.6}$$

and A^+ is equal to 26.

In the outer region, the turbulent viscosity is given by

$$\mu_t = K \cdot C_{cp} \cdot F_{wake} \cdot F_{Kleb} \, (y) \tag{7.7}$$

where

$$K = \text{Clauser constant} = 0.0168$$

$$C_{cp} = 1.6$$

$$F_{wake} = \text{Min } [Y_{max} \, F_{max}, \, C_{wk} \, Y_{max} \, U_{max}^2/F_{max}]$$

$$F_{Kleb}(y) = [1 + 5.5 \, (C_{Kleb}/Y_{max})^6]^{-1}$$

and Y_{max} and F_{max} are the location and maximum functional value given by

$$F(y) = y \, (\omega) \, [1 - \exp(-y^+/A^+)]$$

and

$$C_{wk} = 0.25$$

$$C_{Kleb} = 0.3 \quad .$$

Chapter 8

INITIAL AND BOUNDARY CONDITIONS

8.1   Introduction

As stated earlier, the equations of fluid dynamics pose an initial-boundary value problem which are then solved numerically.   Initial conditions (i.e. the initial state of the fluid) must be supplied for the solution to proceed.   It is usually assumed that the final steady state solution is independent of the initial conditions, although this is not necessarily the case and the author is unaware of any mathematical theorems that state this is true.

On the other hand, the boundary conditions are crucial to achieving a correct solution of the problem and must be consistent with the physics of the problem.   The boundaries of the computational domain include both physical and artificial boundaries.   Physical boundaries are normally walls and it is generally, although not always, possible to specify conditions at these boundaries in a straightforward manner. Artificial boundaries exist due to the necessity of having a finite computational domain and the specification of conditions at these boundaries is more difficult and open to question.

The boundary conditions are also important insofar as the stability and convergence properties of the numerical scheme.   Improper specification of the boundary conditions can lead to instability or slow convergence of the computations.

8.2 Initial Conditions

The initial conditions used in each of the four problems varied depending on the scheme used and are described in the following sections.

8.2.1 Problem One

The initial condition used in scheme one was obtained from the complex velocity potential. It is shown in texts of ideal fluid flow that the potential and stream function together form an analytic function which is called the complex potential as follows

$$F(\zeta) = \theta + i \psi$$

$$= A \zeta(z) \qquad (8.1)$$

where A is a constant. The derivative of the complex potential is then

$$F'(\zeta) = dF/dz$$

$$= u - iv \qquad (8.2)$$

The right-hand side of Eq. (8.2) is called the complex velocity and is the complex conjugate of the velocity vector $u + iv$. For problem one, the complex velocity is given by

$$F'(\zeta) = A \pi \left[(\zeta - 1)/(\zeta + 1) \right]^{.5}$$

$$= \vec{V} = u + iv \qquad (8.3)$$

In order to have u go to u_∞ as ζ goes to infinity, it is necessary to have

$$A = u_\infty/\pi$$

Equation (8.3) then becomes

$$u + iv = u_\infty \left[(\zeta - 1)/(\zeta + 1)\right]^{.5} \qquad (8.4)$$

The value of u_∞ in this case is specified according to the pressure at the exit of the channel since there is no "infinity." Isentropic flow is assumed and the speed of sound and the Mach No. at the exit are obtained from the exit pressure. The velocity at the exit is then taken to be u_∞. The pressure is obtained by assuming the flow to be isenthalpic and using the initial u and v components in Eq. (4.3) to get the speed of sound which is then related to the pressure by the isentropic relation

$$p = \left[a^2/\gamma\right]^{1/(1-\gamma)}$$

The initial condition used in scheme two is a converged solution from a previous run of scheme one. First, the solution is scanned along lines of constant η to determine the shock location. The shock is initially placed at the midpoint between the upstream supersonic and downstream subsonic points. In order to avoid kinks in the initial shape of the shock, which result when the ϵ coordinate value of the midpoint shifts, the shock shape is then smoothed by a simple iterative routine which keeps the shock between the supersonic and subsonic points.

Once the initial shock shape has been determined, a new shock fitted grid is introduced and the old solution is interpolated onto the new grid. The distribution of points along the lines of constant η is done by the following second degree polynomial:

$$\epsilon = \epsilon_0 + (\epsilon_1 - \epsilon_0)(a_1 X + a_2 X^2)$$

where a_1 and a_2 are calculated to satisfy

$$X = 0 \quad \text{at} \quad \epsilon = \epsilon_0$$

$$X = IM\text{-}1 \quad \text{at} \quad \epsilon = \epsilon_1$$

$$X = IS \quad \text{at} \quad \epsilon = \epsilon_s$$

IS is the integer value of the shock point and ϵ_s is the ϵ location of the shock.

The interpolation from the old grid onto the new one is done by a first order linear interpolation. The values of the flowfield u, v, and P at the upstream shock point are determined by a linear extrapolation from the two previous upstream points on the old grid. The Rankine-Hugoniot jump relations are used to obtain u, v, P and the entropy S on the downstream shock points. Since scheme two uses the entropy as the energy variable and since this is not one of the variables used in scheme one, the entropy at each point is obtained from the pressure and the speed of sound using Eqs. (4.4) and (5.3). The normalization for the entropy sets the entropy of the incoming flow equal to zero and so a calculated value of the entropy greater than zero at a point indicates that the fluid has passed through a shock or some other dissipative mechanism. A calculated entropy of less than zero is erroneous and is instead set to zero.

The initial conditions used in scheme three are obtained from the specified Mach number at the entrance and exit of the channel and the assumption that the v component of velocity is zero at these locations.

Then using the assumption that the flow is isenthalpic the speed of sound, the pressure, density and the u component of velocity is obtained at the entrance and exit. The points between the entrance (I = 1) and the exit (I = IM) are then determined by a linear interpolation based on the I coordinate.

The Navier-Stokes code (scheme four) was used in a "flate plate" option which assumed the upper computational boundary is a free stream boundary instead of as a wall as the first three codes assumed. The code, therefore, initialized all flow quantities to the specified free stream values.

8.2.2 Problem Two

In scheme one, the complex velocity is used as in Sec. 8.2.1 and it is found that the velocity is given by [29]

$$u + iv = u_\infty (1 - 1/z^2) \tag{8.6}$$

and the pressure is given by Eq. (8.5)

The initial conditions in scheme two were obtained using the same procedure as in problem one.

The initial conditions in scheme three were obtained using the same procedure as in problem one. However, since the inflow and outflow Mach numbers are the same, the initial condition for this problem is one of uniform flow.

8.2.3 Problem Three

For scheme one, it can be shown that the velocity is given by

$$u + iv = u_\infty/[n(dz/d\zeta)] \tag{8.7}$$

where $dz/d\zeta$ is given by

$$dz/d\zeta = n(z^2 - 1)/(\zeta^2 - 4)$$

and n is given by Eq. (2.8). Again, the pressure is found from the assumption that the flow is isenthalpic and isentropic as in problems one and two.

The initial conditions used in schemes two and three are the same as those used in problems one and two.

8.2.4 Problem Four

The initial condition used for the airfoil problem was developed by (1) first setting surface where the velocity was set equal to the component of the uniform free stream u_∞ tangent to the wall and then, (2) using a simple laplacian operator to smooth the flowfield prior to beginning with the actual flow solver. The reason for using this procedure was to minimize transients which could cause instability in the initial solution and which would be due to initial sharp gradients that would exist such as at the leading edge where the velocity would be zero at the wall and free stream one point off the wall.

8.3 Wall Boundary Conditions

The condition of no flow through the wall was applied at all wall boundaries. For the inviscid calculations, this is the basic condition whereas for the viscous calculations, the additional condition of zero velocity tangent to the wall or the so-called "no slip" boundary condition must also be imposed. The following sections described in detail how these conditions were implemented in each scheme.

8.3.1 Scheme One

Referring to Eqs. (4.21), the no penetration boundary condition implies that $V = V_\xi = V_t = 0$. The two governing equations reduce to

$$P_t + .5 \ [\lambda^+ \ P_\xi^+ + \lambda^- \ P_\xi^- + \Omega^+ \ P_\eta^+ + \Omega^- \ P_\eta^-$$

$$+ \frac{\gamma}{a\sqrt{J}} \ (\lambda^+ \ U_\xi^+ - \lambda^- \ U_\xi^- + \Omega^+ \ V_\eta^+ - \Omega^- \ V_\eta^-)] = P_s \qquad (8.8a)$$

$$U_t + .5 \ [\lambda^+ \ U_\xi^+ + \lambda^- \ U_\xi^- + \frac{a\sqrt{J}}{\gamma} \ (\lambda^+ \ P_\eta^+ - \lambda^- \ P_\eta^-)] = U_s \qquad (8.8b)$$

$$.5 \ [\Omega^+ \ V_\eta^+ + \Omega^- \ V_\eta^- + \frac{a\sqrt{J}}{\gamma} \ (\Omega^+ \ P_\eta^+ - \Omega^- \ P_\eta^-)] = V_s \qquad (8.8c)$$

Equation (8.8b) can be used as it is, but before Eq. (8.8a) can be used, it must be modified to eliminate the terms $\Omega^+ \ P_\eta^+$ and $\Omega^+ \ V_\eta^+$ at the lower wall and the terms $\Omega^- \ P_\eta^-$ and $\Omega^- \ V_\eta^-$ at the upper wall since they require information from outside the computational domain. This is done by combining Eqs. (8.8a) and (8.8c) to get

$$P_t + .5 [\lambda^+ P_\xi^+ + \lambda^- P_\xi^- + 2 \Omega^+ P_\eta^+$$

$$+ \frac{\gamma}{a\sqrt{J}} (\lambda^+ U_\xi^+ - \lambda^- U_\xi^- + 2 \Omega^+ V_\eta^+)] = P_s + \frac{\gamma}{a\sqrt{J}} V_s$$

which applies at the upper wall and

$$P_t + .5 [\lambda^+ P_\xi^+ + \lambda^- P_\xi^- + 2 \Omega^- P_\eta^-$$

$$+ \frac{\gamma}{a\sqrt{J}} (\lambda^+ U_\xi^+ - \lambda^- U_\xi^+ - \lambda^- U_\xi^- - 2\Omega^- V_\eta^-)] = P_s - \frac{\gamma}{a\sqrt{J}} V_s$$

which applies at the lower wall. The governing equations can therefore be used at the walls and the three explicit scheme used as in the interior points.

8.3.2 Scheme Two

The same concept as just described for scheme one is also applied in this case. The resulting equations are slightly different and will not be given.

8.3.3 Scheme Three

Since scheme three solves the governing equations implicitly, the implementation of the scheme at the boundaries poses difficulties and explicit boundary conditions are used instead. The velocity V and density at the wall are first found by extrapolation from the inside. The pressure at the wall is next found by extrapolation from the interior using the momentum equation in the η direction

$$\frac{\partial p}{\partial \eta} = \rho (u^2 + v^2)/[R(n_x^2 + n_y^2)^{.5}] \tag{8.9}$$

where R is the radius of curvature and is given by

$$R = (1 + (f')^2)^{1.5}/f''$$

$$f' = dy/dx \qquad (8.10)$$

The density at the wall is now recalculated by using the assumption that

$$\rho = \gamma \, p^\gamma \qquad (8.11)$$

which is not valid if there are entropy gradients normal to the wall but which may be regarded as approximately true. Using this assumption, the density gradient along n_o is given by

$$\frac{\partial \rho}{\partial p} = (1/a^2) \frac{\partial p}{\partial \rho} \qquad (8.12)$$

8.3.4 Scheme Four

As stated earlier, for the viscous calculations, both the u and v components of velocity are taken to be zero to satisfy the no-slip boundary condition. The density at the wall is next obtained by a zero order extrapolation from the point above it. Next, the speed of sound one point off the wall is found by using the energy equation as follows. The density at the same location is then used in conjunction with the speed of sound to get the pressure at the wall. The pressure at the wall divided by $(\gamma - 1)$ is then the total energy which completes the procedure.

8.4 Subsonic Inflow Boundary

This section and the following two involve "artificial" boundaries in the sense that they exist in the computational domain but not in the physical domain. Since boundary conditions must be imposed to make the problem solvable and since these conditions must reflect the actual physical situation, the correct specification of these conditions is fairly important. Much of what has been done up until the present time involves making some simplifying assumptions and frequently characteristic theory is used. At the upstream boundary, the flow is subsonic and entering the computational domain. If the flow is assumed to be inviscid so that the Euler equations apply, the governing equations in primitive variable form are

$$Q_t + A Q_x + B Q_y = 0 \qquad (8.13)$$

where

$$Q = \begin{bmatrix} \rho \\ u \\ v \\ p \end{bmatrix} \qquad (8.14a)$$

$$A = \begin{bmatrix} u & \rho & 0 & 0 \\ 0 & u & 0 & 1/\rho \\ 0 & 0 & u & 0 \\ 0 & \gamma p & 0 & u \end{bmatrix} \qquad (8.14b)$$

$$B = \begin{bmatrix} v & 0 & \rho & 0 \\ 0 & v & 0 & 0 \\ 0 & 0 & v & 1/\rho \\ 0 & 0 & \gamma p & v \end{bmatrix} \qquad (8.14c)$$

The eigenvalues of A are u, u, u + a and u - a. The eigenvalues of B are v, v, v + a and v - a. The directions u + a and v + a are referred to as bicharacterisitics and are the intersections of the characteristic monge conge with the planes x = constant and y = constant.

It is well known that for purely one-dimensional unsteady isentropic flow, the equations of gas dynamics possess Riemann invariants which are constant along characteristics. These functions are

$$R^+ = u + 2\,a/(\gamma - 1) \qquad \text{along } dx/dt = u + a \qquad (8.15a)$$

$$R^- = u - 2\,a/(\gamma - 1) \qquad \text{along } dx/dt = u - a \qquad (8.15b)$$

At a subsonic inflow boundary, the R^+ value is constant along the characteristic entering from outside of the computational domain and can therefore be specified and used in conjunction with R^- from inside the domain to get new values of u and a. Equation (4.13) does not possess Riemann invariants but according to the theory of Kreiss, the number of conditions which must be specified at an inflow (or an outflow) boundary in order to have a numerically stable boundary condition must agree with the number of characteristic lines that approach the boundary from the outside [52]. If the flow is assumed to be at least locally one-dimensional, this would mean that there must be three quantities specified from the outside and one extrapolated from the inside at the inflow boundary and the reverse at the outflow boundary.

8.4.1 Schemes One and Two

The conditions which were assumed for problems one through three were that the contravarient component of velocity V is zero and that the flow is isentropic and isenthalpic at the inflow boundary. The first

assumption is an approximation to the actual physical situation and is not exactly correct while the thermodynamic assumptions are correct in the steady state. Since V and V_t are assumed zero, the governing equations are

$$P_t + .5 \left[\lambda^+ P_x^+ + \lambda^- P_x^- + \Omega^+ P_y^+ + \Omega^- P_y^- + \frac{\gamma}{a\sqrt{J}} (\lambda^+ U_x^+ - \lambda^- U_x^-) \right] = P_s$$

$$U_t + .5 \left[\lambda^+ U_x^+ + \lambda^- U_x^- + \frac{a\sqrt{J}}{\gamma} (\lambda^+ P_x^+ - \lambda^- P_x^-) \right] = U_s$$

$$U V_x X_\xi + \frac{a\sqrt{J}}{2\gamma} (\Omega^- P_y^- - \Omega^- P_y^-) = V_s$$

Since the flow is subsonic, it is not possible to use these equations since P and U require information from outside the domain. But the two equations for P_t and U_t can be combined to eliminate these terms to get

$$P_t - \frac{\gamma}{a\sqrt{J}} U_t + \lambda^- P_x^- + .5 (\Omega^+ P_y^+ + \Omega^- P_y^-) + \frac{\gamma}{a\sqrt{J}} (U_s - \lambda^- U_x^-) = P_\xi$$
$$\text{(8.16)}$$

It is possible to relate P_t to U_t by the 1-D energy equation

$$a^2 / (\gamma - 1) + .5 (u^2 + v^2) = h_0 = \text{const} \tag{8.17}$$

It is not necessary but if it is also assumed that $v = 0$, then

$$a \cong U/J^{.5} \tag{8.18}$$

and since the flow is isentropic

$$a^2 = \gamma \, p^{(\gamma-1)/\gamma}$$

which leads to the equation

$$P_t \cong - \gamma \; U \; U_t /(a^2 \; J) \tag{8.19}$$

which can then be substituted back into Eq. (8.18) to get a single equation for U_t as follows

$$U_t = \frac{U_s - \lambda^- \; U_x^- - a \; J^{.5} \; [P_s - \lambda^- \; P_x^- - .5 \; (\Omega^+ \; P_y^+ + \Omega^- \; P_y)]}{[1 + U/a \; J^{.5}]}$$

P_t can then be obtained using Eq. (8.19).

8.4.2 Scheme Three

The inflow boundary condition used in this scheme is described by von Lavante in [47] and will only be briefly discussed here. The assumption is made that the flow is locally one-dimensional so that the governing equations can be written in the characteristic form

$$\frac{\partial W}{\partial t} + \Lambda \; \frac{\partial W}{\partial x} = 0 \tag{8.20}$$

where W is the characteristic variable given as

$$W = \begin{bmatrix} W_1 \\ W_2 \end{bmatrix} \qquad \begin{aligned} W_1 &= 1 + u(\gamma - 1)/2 \; SQ_{1D} \\ W_2 &= 1 - u(\gamma - 1)/2 \; SQ_{1D} \end{aligned} \tag{8.21}$$

$$\Lambda = \begin{bmatrix} \lambda_1 & 0 \\ 0 & \lambda_2 \end{bmatrix}$$

$$SQ_1 = [(u(\gamma - 1)/2 \; \gamma)^2 + a^2/\gamma]^{.5}$$

The characteristic variable W_1 propagates along the characteristic $dx/dt = u + a$ and is therefore specified whereas the variable W_2 propagates along the backward characteristic $dx/dt = u - a$ and is taken from the inside of the computational domain. Equations (8.21) are then solved simultaneously on the boundary to get the Mach number at the inflow which is

$$M^2 = 1/\{(\gamma - 1)^2 \ [1/(W_1 - W_2)^2 - 1/4]\} \qquad (8.22)$$

The Mach number is then used to calculate ρ, u, v and p from the isentropic relationships and the energy Eq. (8.17). The procedure is very similar, at least in principle, to a "time split" inflow boundary condition introduced by Tong [55] and avoids the necessity for assuming that $v = 0$ at the inflow boundary as was the case in schemes one and two. Furthermore, it has been found that the procedure gives good results even when the upstream boundary is close to a leading edge.

8.4.3 Scheme Four

The condition used in this situation first assumes the v component is zero so the flow is taken to be locally one-dimensional. The pressure at the inflow boundary is then found from the energy equation using the known values of the total energy and the u and v components of velocity at the next point downstream. The pressure is then used to get the density assuming the flow is also isentropic. Finally, the u component of velocity is found using the isenthalpic energy Eq. (8.17). This procedure should thus allow pressure waves which are traveling upstream to escape without reflection. However, the assumption that $v = 0$ at the boundary is not strictly correct and may introduce errors.

8.5 Outflow Boundary Condition

At the outflow boundary, there are three characteristics from inside the computational domain and one from outside and hence according to the theory of Kreiss, one condition may be specified at the outflow boundary. This condition is usually taken to be the pressure since this determine the flow through the channel at the steady state. For example, in a De Laval nozzel, the backpressure completely determines the flow inside the nozzel and the conditions at the throat. However, if the pressure is specified as constant at the outflow boundary, then during the convergence from the initial condition to the final steady state solution, pressure waves which may develop inside the computational domain are reflected at the outflow boundary instead of passing through and this will slow convergence.

The approach used in the first three schemes was introduced by Rudy and Strikwerda [54] and was based on earlier work by Enquist and Majda [55] and Hedstrom on nonreflective boundary conditions. The idea is to apply the following equation at the outflow boundary

$$\frac{\partial p}{\partial t} - \rho \ c \ \frac{\partial u}{\partial t} + \alpha \ (p - p_e) \tag{8.23}$$

where α is some constant and p_e is the specified pressure at the boundary. In the steady state, the pressure p should be equal to p_e. The numerical approximation to Eq. (8.23) is

$$p^{n+1} = [p^n + \alpha \ \Delta t \ p_e + \rho^n \ a^n \ (u^{n+1} - u^n)]/(1 + \alpha \ \Delta t)$$

where u^{n+1} is extrapolated from the inside to the boundary. This procedure has been found to work well but has the disadvantage that the parameter α must be chosen. As α approaches zero, the influence of the

specified back pressure is also relaxed and approaches zero. As α is increased, the outflow boundary becomes increasingly reflective and p is maintained close to the specified p_e. Rudy and Strikwerda recommend that α be chosen to optimize the convergence to the steady and show that α has a significant effect on the number of iterations required for a ty, cal test case to converge. Figure 8.1 shows the results of applying this boundary condition to problem one.

In scheme four, the pressure was simply held constant at the outflow boundary while the density and the u and v components of velocity were set equal to the next upstream point. This is an entirely reflective boundary condition but was used in the flat plate option because the flow assumed to be mainly all boundary layer and hence parabolic. This assumption was not true in the cases modeled but is the physical condition imposed is correct in the steady state.

8.6 Far Field Boundary Condition

The far field refers to the flow field at a distance away from the body which is significantly greater than the length scale of the body. For example, it is common practice to put the outer boundary for two-dimensional transonic calculations about airfoils at least ten chord lengths away from the airfoil. The reason for this is that one would like to specify conditions in the free stream where the flow is unaffected by the body but this only occurs at an infinite distance away from the body. Since it is impossible to construct grids which go out to infinity, it is necessary to specify boundary conditions in the far field where there are still perturbations about the free stream conditions.

MACH NO. AT EXIT

```
            UPPER  WALL  AT  20
·······     UPPER  WALL  AT  40
            UPPER  WALL  AT  100
```
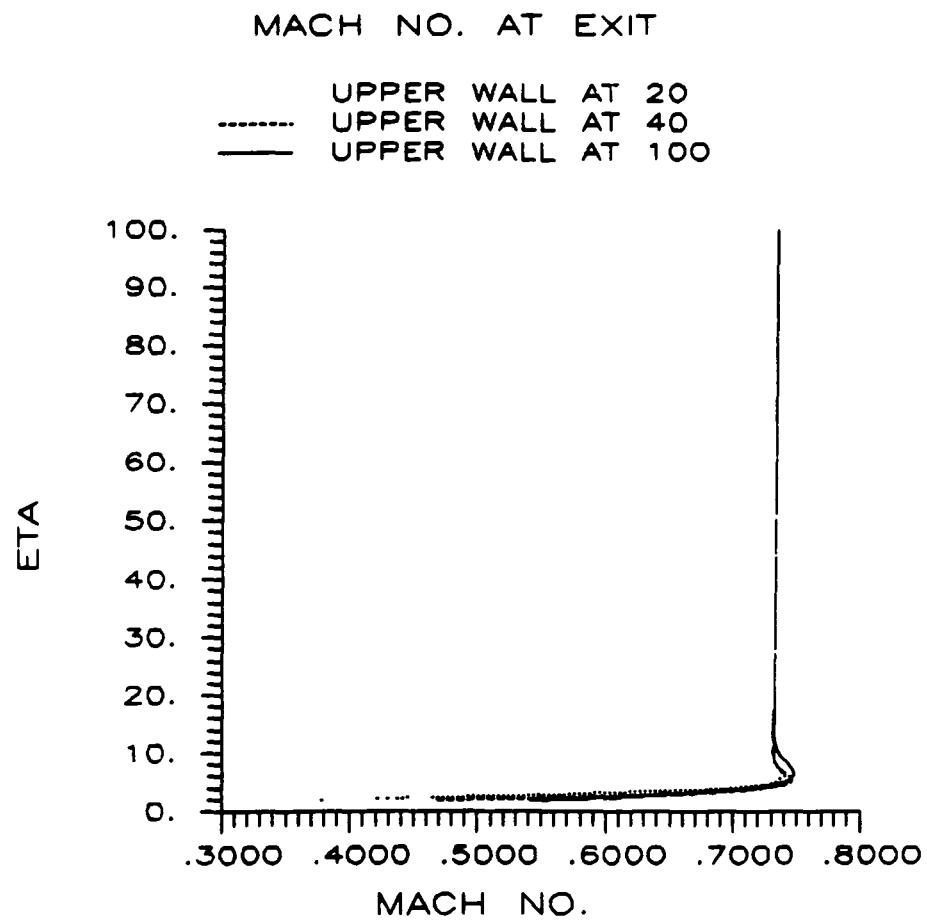

Fig. 8.1 Mach Number at Outflow Boundary.

In problems one and two, the upper boundary was treated as a solid wall in all of the schemes except scheme four. Since this scheme solves the viscous equations, it was deemed desirable to avoid treating the upper boundary as a wall since doing so would necessitate grid clustering at the top and lower boundaries due to the existence of boundary layer growth on both surfaces. Therefore, this boundary was treated in exactly the same manner as the outflow boundary was treated. The pressure was held constant at the free stream pressure and the remaining variables were extrapolated from inside the computational domain. This approach may not produce the best convergence, but the results appear reasonable at the top boundary. Attempts were made to develop characteristic based nonreflective boundary conditions for the top boundary for schemes one, two and three which would permit this boundary to be relatively close to the lower boundary and allow for a better comparison between these schemes and scheme four but these efforts were not successful. Instead, the upper boundary was progressively moved away from the lower wall until the perturbations at the upper boundary were reduced to an acceptable level.

For problem four, the outer boundary condition which was used was developed by Thomas and Salas [56]. The approach assumes that wavelike transients in the physical domain arrive at the outer boundary in a direction mainly normal to the boundary as shown in Fig. 8.2. The flowfield at the outer boundary can be thought to consist of a uniform flow plus small perturbations due to these transient waves which in time should decay to the final deviations from the uniform flow. Therefore, the gradients along the outer boundary are assumed small in comparison to the gradients normal to the boundary the following characteristic relations are presumed valid
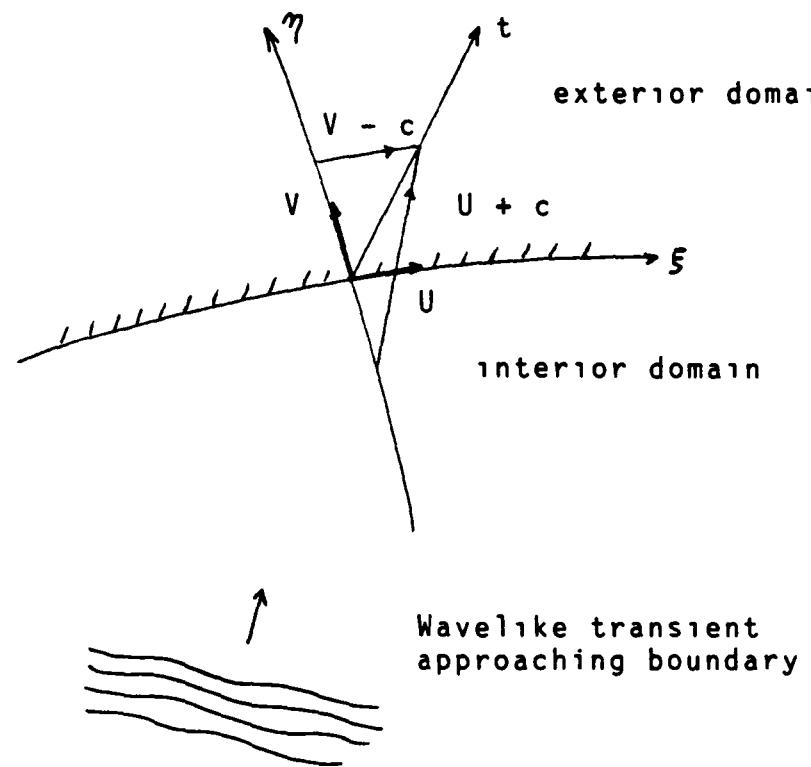
Fig. 8.2 Far Field Boundary Condition.

$$dS/dt = 0 \qquad \text{along } d\eta/dt = U \qquad (8.21a)$$

$$dV/dt = 0 \qquad \text{along } d\eta/dt = U \qquad (8.21b)$$

$$\frac{dU}{dt} + \frac{1}{\rho a}\frac{dp}{\partial t} = 0 \qquad \text{along } d\eta/dt = U + a\, J^{.5} \qquad (8.21c)$$

where S is the entropy and U and V are the contravarient velocities in the ξ and η directions respectively. Since the flowfield at the outer boundary is isentropic for inviscid flow and nearly so even for viscous flow, Eq. (8.24) implies the existence of Riemann invariants at the outer boundary and the equivalent of Eq. (8.15) in a direction normal to the outer boundary is

$$R^{\pm} = \vec{V} \cdot n + 2\,a/(\gamma - 1)$$

$$\text{along } d\eta/dt = \vec{V} \cdot n + a \qquad (8.25)$$

where

$$\vec{V} \cdot n = V/[J\,(x_E^2 + y_E^2)^{.5}]$$

The invariant R⁻, which reaches the boundary from outside the computational domain, is specified from the free stream values of u and a applied at the outer boundary and the values of R⁺ is taken from inside the computational domain. The equations for R⁺ and R⁻ are then solved simultaneously to get the new values of V and a on the boundary. Depending on the sign of V, the values of the remaining variables U, ρ, and p are then either taken from inside or outside the computational domain. If V is negative, the flow at the boundary is in and the free stream values of u, ρ, and p are used. If V is positive, the flow at

the boundary is out and U, ρ, and p are extrapolated from the inside of the domain. This procedure has been found to give good results in the computations performed as a part of this investigation. However, Roe has questioned the practice of assuming locally one-dimensional flow at remote boundaries and claims that it does not result in the monotonic decay of the pressure and the radial component to the expected free stream values [57]. More work will undoubtedly be done on the treatment of far field boundaries in the future in view of the importance of the topic.

Chapter 9

RESULTS AND DISCUSSION

9.1 Problem One

9.1.1 Inviscid Results

The three inviscid codes were run using various values of η for the lower and upper boundaries, referred to as η_0 and η_1 respectively. The lower boundary η_0 was varied to study the effect of changing the geometry from a channel with a gradual one-sided expansion to a channel with a one-sided sudden expansion (rearward facing step). It was found that a value $\eta_0 = 2$ produced a shock at the expansion corner near $\xi = -1$ and the flow was attached. As η_0 was reduced, the flow would eventually separate (usually before $\eta_0 = 1$) and as η_0 was further reduced the recirculation zone would grow in size. The effect of moving the upper boundary was also studied; it was found early in the investigation that the position of η_1 strongly affected the flow in the entrance region of the channel ahead of the expansion corner. This is because the ratio of the entrance area to the exit area is increased and approaches 1.0 as η_1 is increased and the result can be seen in Fig. 9.1 which shows the Mach number distribution across the inflow boundary for $\eta_1 = 20$, 40, and 100 using scheme one. As η_1 is increased, the inflow Mach numbers are reduced as would be expected.

UPPER WALL AT 20
········ UPPER WALL AT 40
———— UPPER WALL AT 100
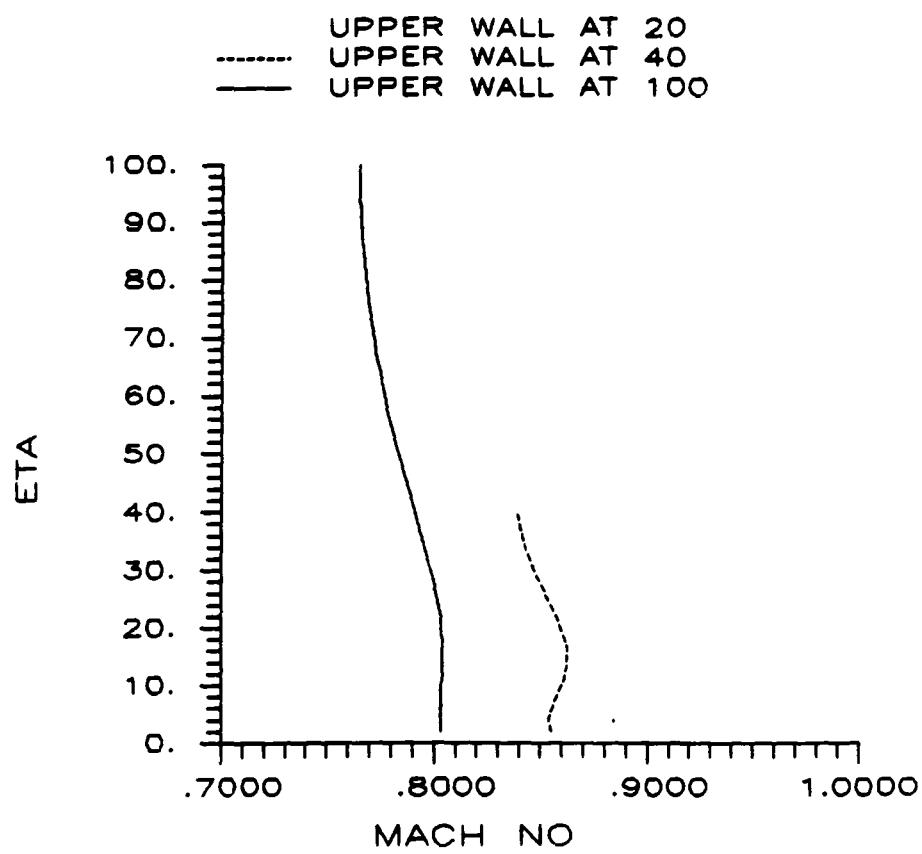
Fig. 9.1 Mach Number at Channel Entrance.

The three inviscid codes were run on 81x41 grids of which an example (with $n_0 = 2$ and $n_1 = 20$) is shown in Fig. 9.2. In addition, the shock fitting was also repeated using 161x81 grids to determine the effect of refining the grid by a factor of two. In general, scheme one was run for 3000 iterations in each case, which usually resulted in a residual drop, measured by the ℓ_2 norm of $\partial_t p$, of between two and three orders of magnitude. The slow rate of convergence is due to the CFL < 1 limitation and the fact that no convergence acceleration methods other than local time stepping were used.

The shock fitting runs were done in continuous sequences with n_0 initially equal to 2 and then gradually reducing n_0 in a step-like manner. Thus, the lower wall was first brought to n_0 of 1.8 and this position held constant until the shock movement was reduced to an acceptable level. This procedure was repeated by reducing n_0 in steps of 0.2 and usually at least 2000 to 3000 iterations were required on the coarse grid to steady the shock, while on the fine grid 4000 to 5000 iterations were required.

The implicit flux-vector splitting scheme was run for 2000 iterations in most cases and the residual drop, measured by the norm of $\partial_t p$, was usually at least three orders of magnitude. In some cases, a constant global time step was used, while in other cases a constant local maximum CFL generally between three and six was used. It was found that the later approach gave the best convergence results and was therefore used for most of the later runs.

The Mach number on the upstream side of the shock foot is shown in Figs. 9.3, 9.4 and 9.5 for n_1 positions of 20, 40 and 100 respectively.
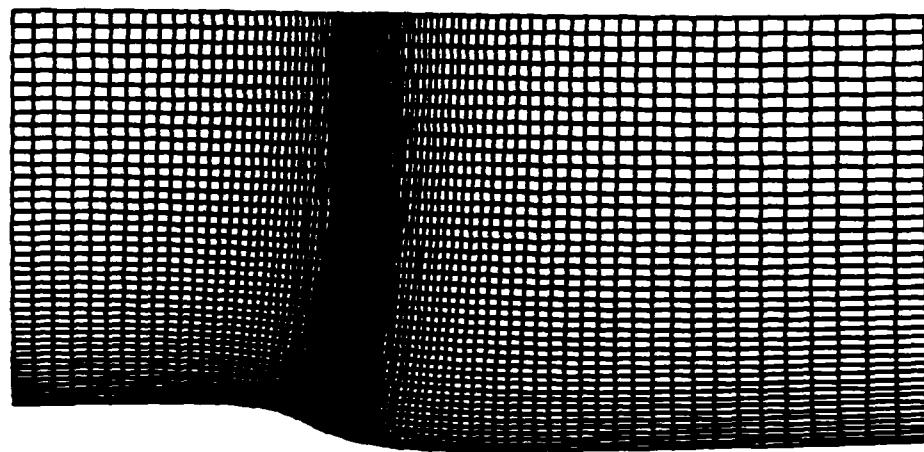
MIN ETA: 2.00   MAX ETA: 20.00
MIN XI: -15.00   MAX XI: 25.00

Fig. 9.2   Example 81x41 Grid Used for Inviscid Calculations.

In Fig. 9.3, it is apparent that scheme one produces significantly higher Mach numbers as n_0 is reduced than the other two schemes. This is believed due to the nonconservative formulation of scheme one. There is fairly good agreement between the coarse and the fine grid solutions obtained using scheme two. The Mach numbers obtained using the flux vector splitting scheme were consistently lower than those obtained using schemes one and two, perhaps due to greater dissipation at the shock in scheme three. The lowest n_0 for which solutions were obtained was 0.4 for schemes one and two and 0.1 for scheme three. It was only possible to get a solution at $n_0 = 0.1$ for scheme three by changing the grid in steps to gradually reduce n_0, while at the same time increasing cluster points at the expansion corner. It can be seen that the Mach number at the shock foot reaches a maximum for schemes two and three at $n_0 = 1.2$, and as n_0 is further reduced, the Mach number gradually becomes lower and the results using scheme three suggest it would go to a limit of 1. at $n_0 = 0$.

The results at $n_1 = 40$ are shown in Fig. 9.4. The results using scheme one, again, show that as n_0 is reduced, the Mach number at the shock foot increases. The results from the shock fitting scheme two show two different tendencies on the coarse and fine grids. On the coarse grid, the trend is similar to scheme one, whereas on the fine grid the results are similar to those of scheme three. The anomalous results using scheme one were checked by doing this series of runs over again with 4000 iterations being taken when n_0 is reduced each 0.2. The results were well converged and do not appear to be in error. The increase in the Mach number is partially explained by the shock position as will be discussed later. Again, the results using scheme three
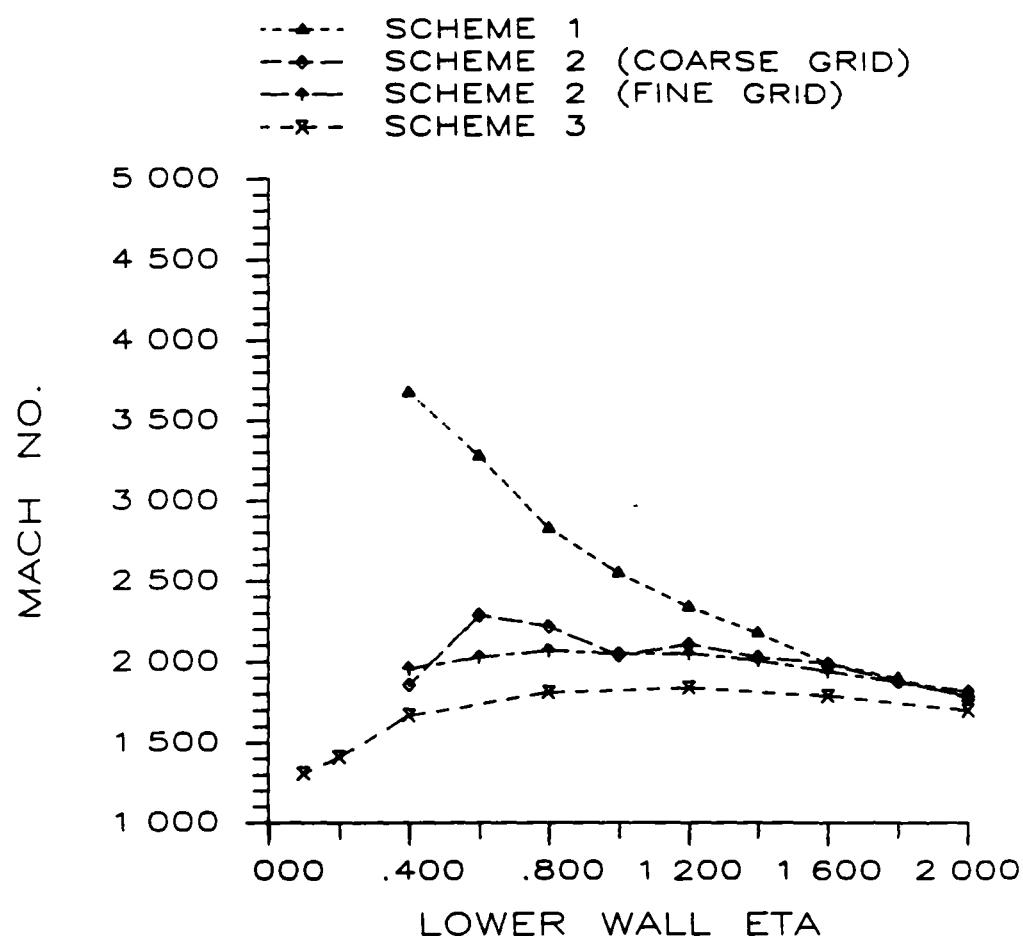
Fig. 9.3 Mach Number at Shock ($\eta_0 = 20$).
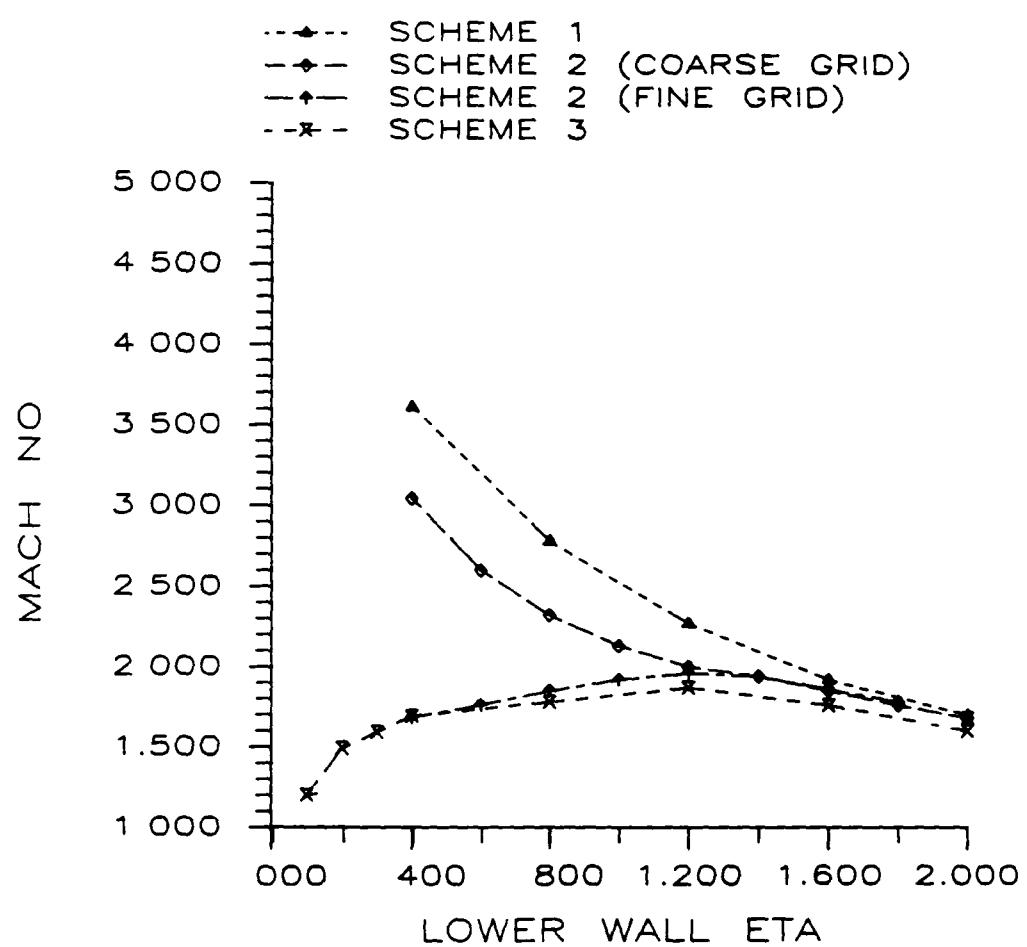
Fig. 9.4 Mach Number at Shock (η_o = 40).
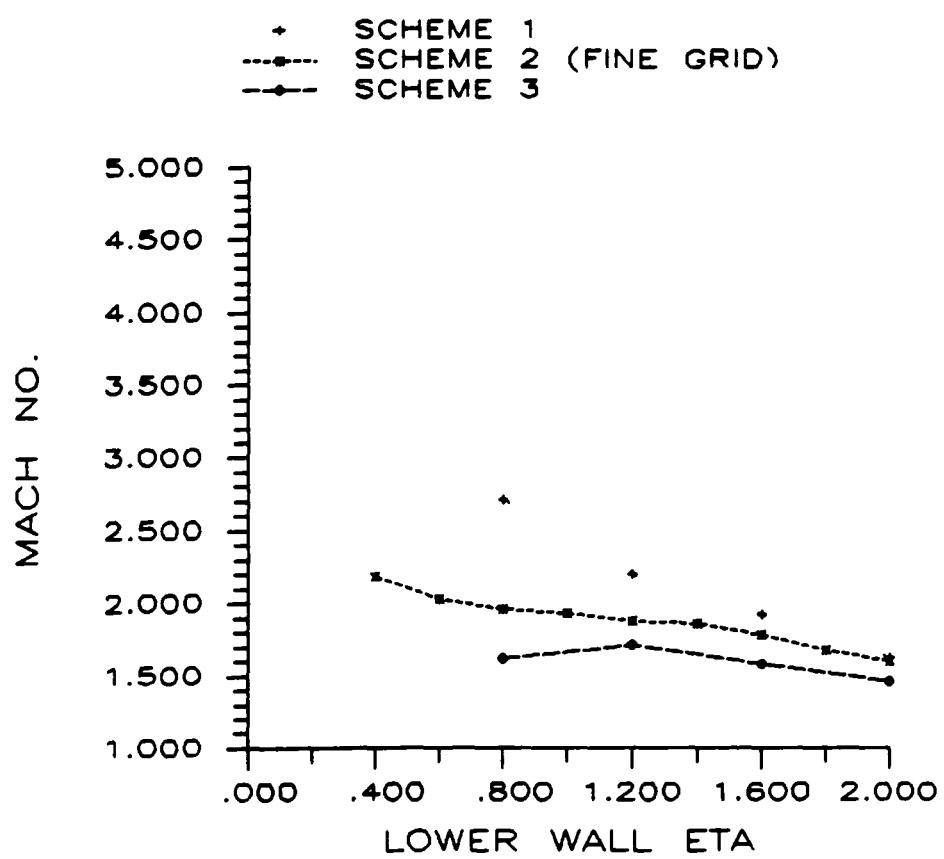
Fig. 9.5 Mach Number at Shock (η_l = 100).

show the lowest Mach numbers —and are similar to those obtained at $n_1 = 20$. The lowest n_0 for which a solution was obtained was 0.1 using scheme three and this was again achieved by changing the grid to progressively cluster the grid about the expansion corner. The trends show the Mach number ahead of the shock decreasing to a limit of one as n_0 approaches the limit zero which suggests that the shock would eventually vanish. The results obtained using scheme three for $n_1 = 40$ agree closely with the results obtained with the same scheme for $n_1 = 20$.

From Fig. 9.5, it is seen that the Mach number at the shock is always less with $n_1 = 100$ than each corresponding case at $n_1 = 40$. This is due to the lower velocities in the flow field ahead of the shock. The fine grid shock fitting results show the Mach number to be gradually increasing; whereas, for the flux vector splitting, the maximum value of M occurs at 1.2 and then decreases. No reliable results were obtained for n_0 values lower than 0.4 because the resolution of the grids at the corner at $\xi = -1$ was inadequate.

Figures 9.6, 9.7 and 9.8 show the shock location ξ_s in terms of the ξ coordinate along the lower wall. A value of ξ equal to -1 corresponds to the location of the upper corner as shown in Fig. 2.1. The results obtained using scheme 1 are identical at $n_1 = 20$ and $n_1 = 40$ and are not appreciably different at $n_1 = 100$. The shock fitting results and the flux vector splitting results at $n_1 = 20$ show general agreement with $\xi_1 = 40$ on the coarse grid show the shock moving progressively towards $\xi = -.5$ as n_0 is reduced. This partially explains the Mach numbers at the shock the position $\xi = -.5$ is considerably further around the expansion corner than the fine grid results which
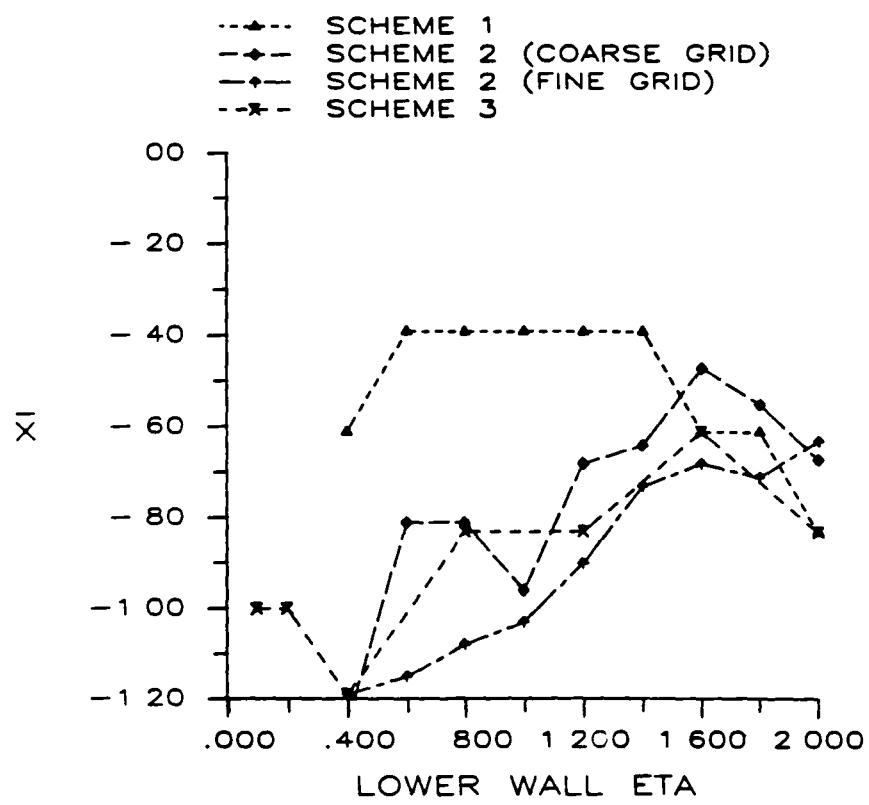
Fig. 9.6 Shock Location vs. η_o ($\eta_i = 20$).
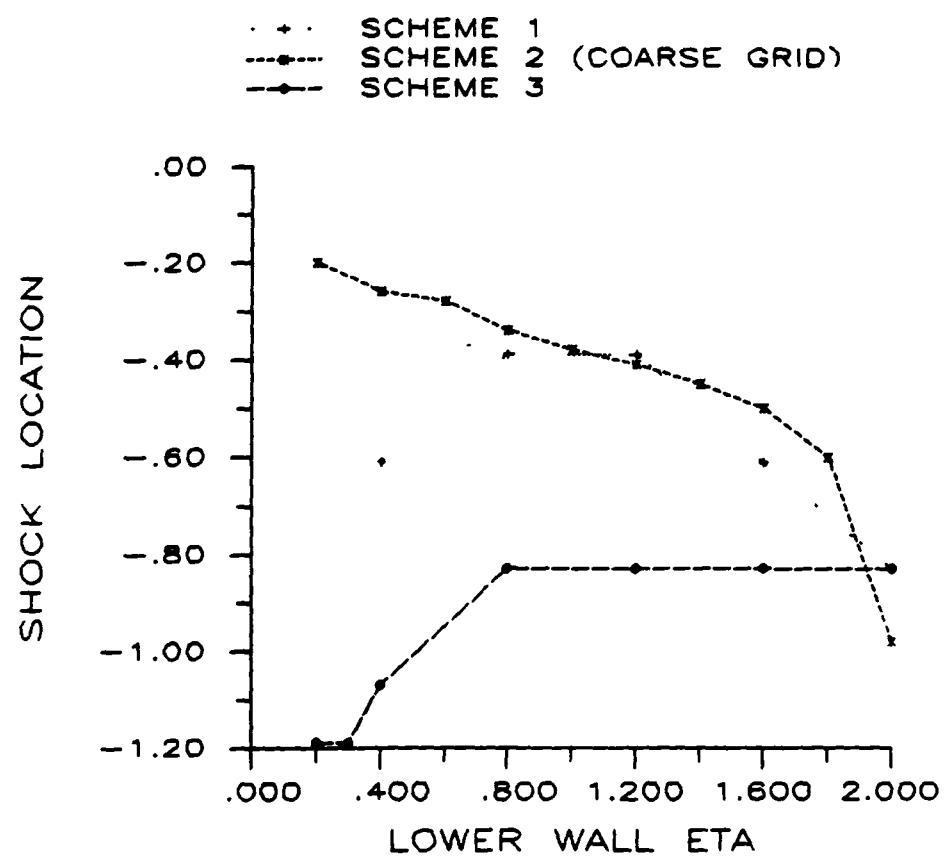
Fig. 9.7 Shock Location vs. η_o ($\eta_i = 40$).
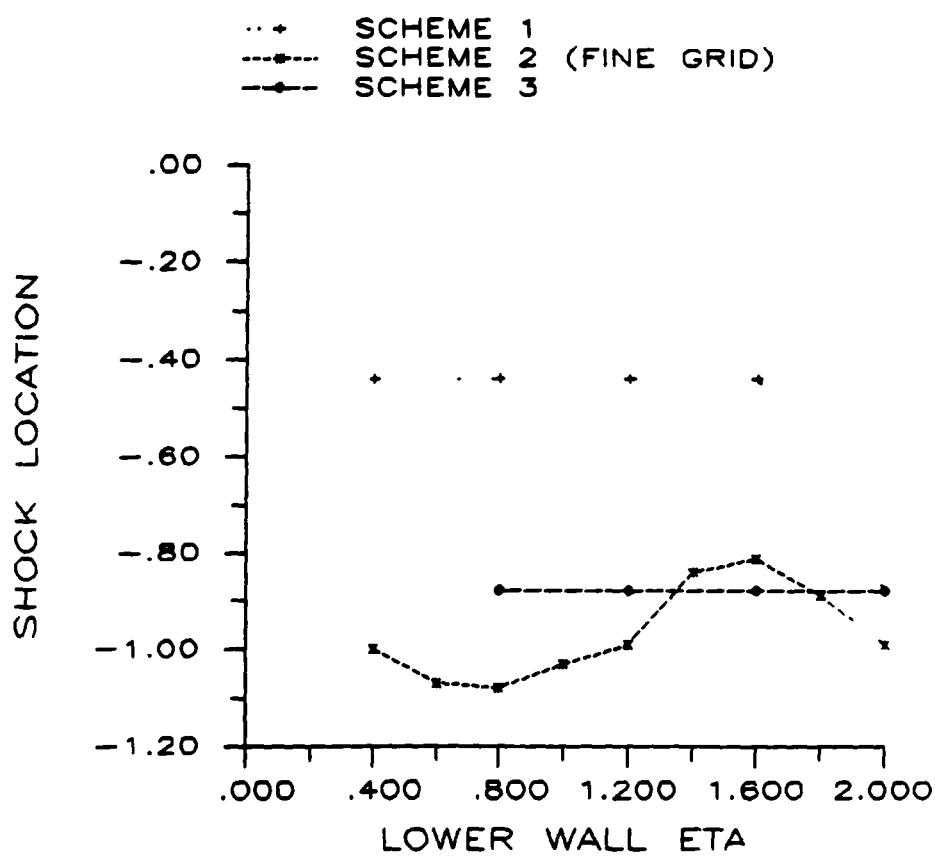
Fig. 9.8   Shock Location vs. η_o ($\eta_l = 100$).

means that the flow has accelerated more and is moving at higher velocities. The flux vector splitting results at all three values of n_1 agree fairly closely. In particular, it is noteworthy that the shock position at $n_0 = .1$ is approaching $\xi = -1$. The shock fitting scheme two for $n_1 = 100$ also shows ξ going to a limit of -1 as n_0 is reduced. It thus appears that this is the proper limiting position of the shock, but this is not achieved in all of the case computed.

The maximum entropy in the flow on the downstream side of the shock is shown in Fig. 9.9 and the vorticity in the flow downstream of the shock is shown in Fig. 9.10 both for cases when $n_1 = 20$. It can be seen that there is a fairly consistent trend for the entropy to increase and the vorticity to decrease toward larger negative values as n_0 is reduced. This result must be interpreted with caution. As stated earlier, it may be the vorticity in the initial unsteady transient flow which leads to separation. Theoretically, none of the entropy and vorticity produce in the flow in the steady state actually enters the separation zones, when they occur. Nevertheless, it is indicative of the conditions which may have led to separation.

In Fig. 9.11, the minimum value of the Mach number multiplied by the direction of the flow along the lower wall is plotted against for $n_1 = 20$. This indicates the approximate value of n_0 at which the flow separates for each scheme. It can be seen that scheme one produces separation at a higher value of n_0 ($n_0 = 1.68$) than scheme two ($n_0 = 1.52$) and that scheme three requires n_0 equal to approximately 1.12 before separation occurs. Thus scheme three appears to be the least susceptible to separation as compared with schemes one and two.

Fig. 9.9 Entropy Downstream of Shock.

VORTICITY

```
    +        SCHEME  1
--·--      SCHEME  2  (COARSE  GRID)
-·-        SCHEME  2  (FINE  GRID)
-*-        SCHEME  3
```
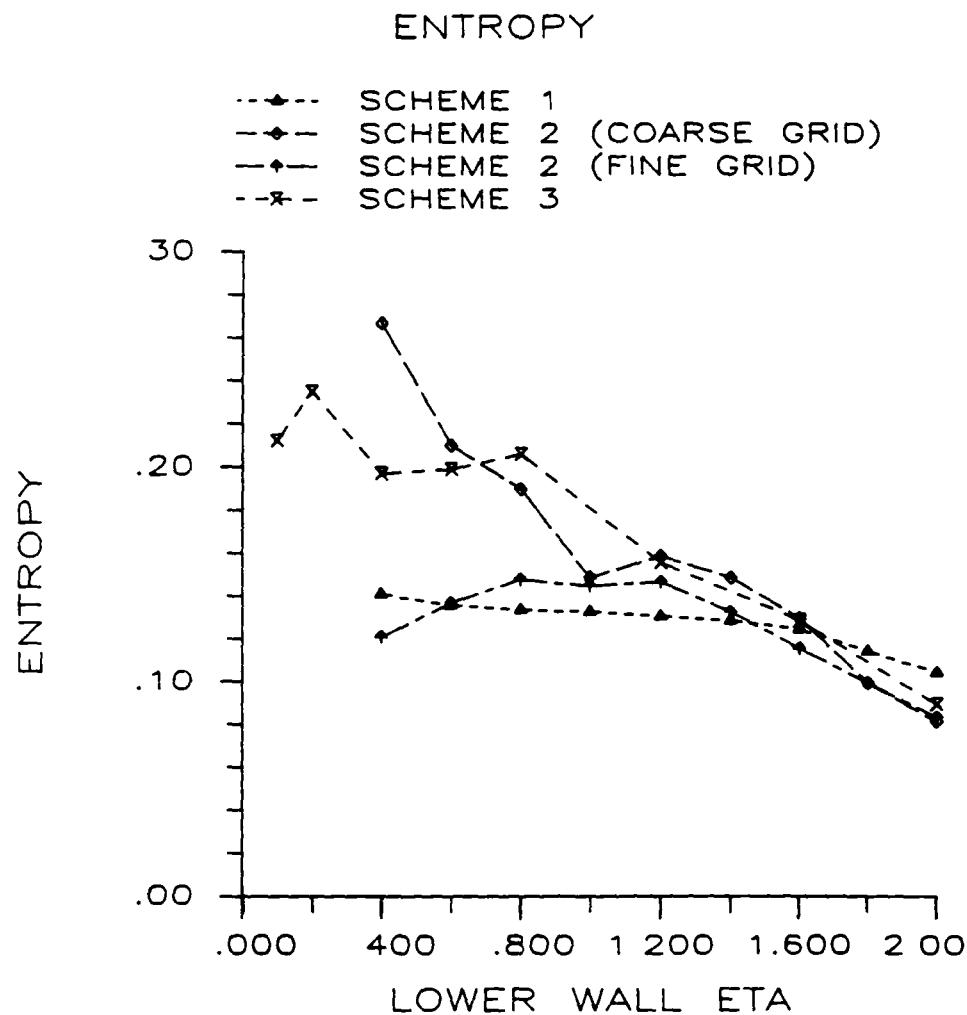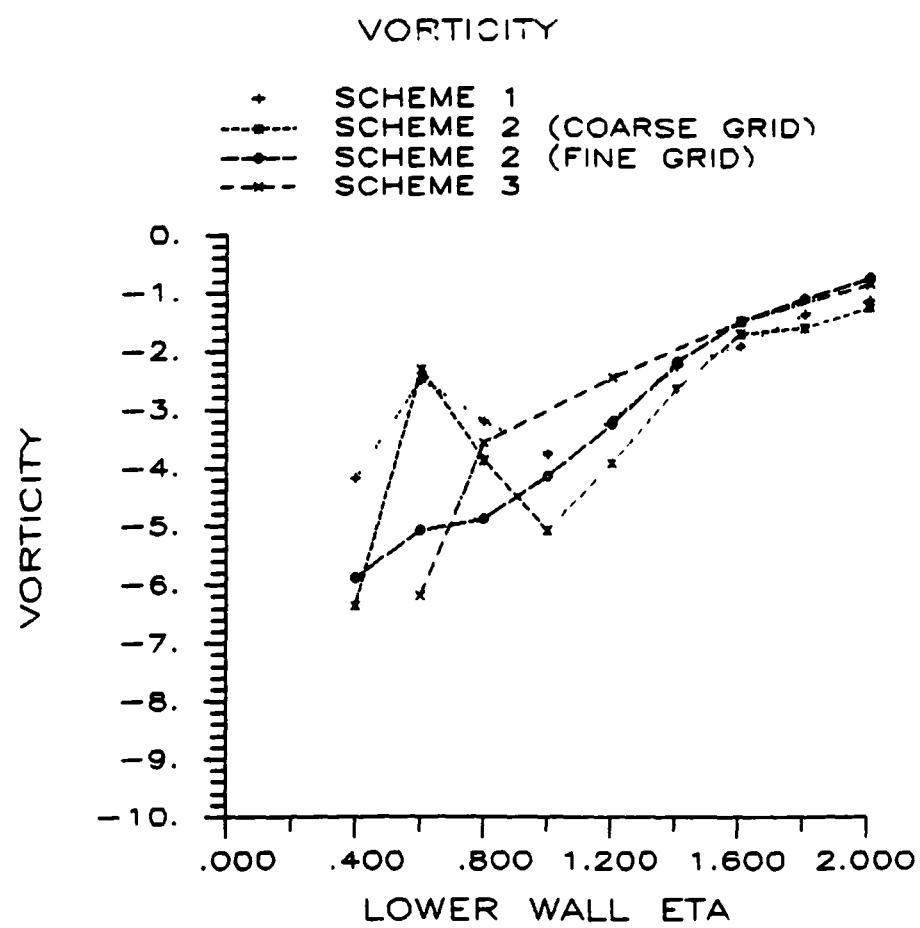

Fig. 9.10   Vorticity Downstream of Shock.
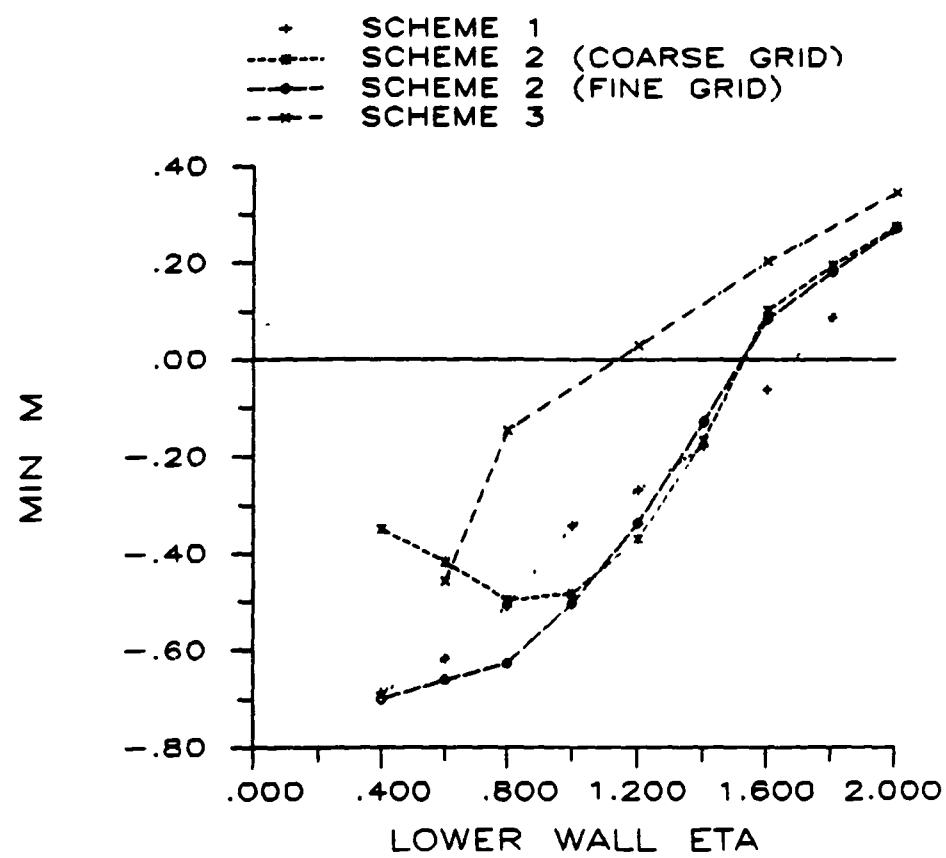
Fig. 9.11 Minimum M vs. η_o (η_i = 20).

The reattachement ξ locations for the same set of cases is shown in Fig. 9.12. There appears to be general agreement in that as η_0 is reduced, the separation bubbles grow in length and reattach further downstream. Similar results for the case when $\eta_1 = 100$ are shown in Figs. 9.13 and 9.14. It can be seen that, in general, having the upper boundary further away reduces the η_0 at which the lower wall must be before separation occurs and the ξ at which reattachment occurs is less, which means that the separation bubbles are not as long.

A comparison of the result using schemes one, two and three with $\eta_1 = 20$ and $\eta_0 = 2.0$ is shown in Figs. 9.15 and 9.16. Figures 9.15a-9.15c show Mach contours and it can be seen that the results are all similar. The Mach numbers multiplied by the sign of U along the lower wall are shown in Fig. 9.16 and again the close agreement is evident. The shock location is nearly identical in all three cases while the maximum computed Mach number reached at the upstream side of the shock is higher using shemes one and two than three. A similar comparison for the case with $\eta_1 = 20$ and $\eta_0 = 1.2$ is shown in Figs. 9.17 and 9.18. Again general agreement is evident although the Mach contours of the flux vector splitting results appear smoother. A comparison of the Mach number multiplied by the sign of U is shown in Fig. 9.18. The flux vector splitting results, while close to separation, have not separated whereas the results of both scheme one and two have. It is also apparent that the jump in velocity using the unfitted scheme one is now much greater than either scheme two or three. A third such comparison with $\eta_0 = 0.4$ is shown in Figs. 9.19 and 9.20. Figures 9.19b and 9.19c show Mach contours generated from the results of scheme two on the coarse and fine grids respectively. The contours shown in Fig. 9.19a

Fig. 9.12   Reattachment ξ vs. η_o (η_l = 20).

SCHEME 1
SCHEME 2 (FINE GRID)
SCHEME 3
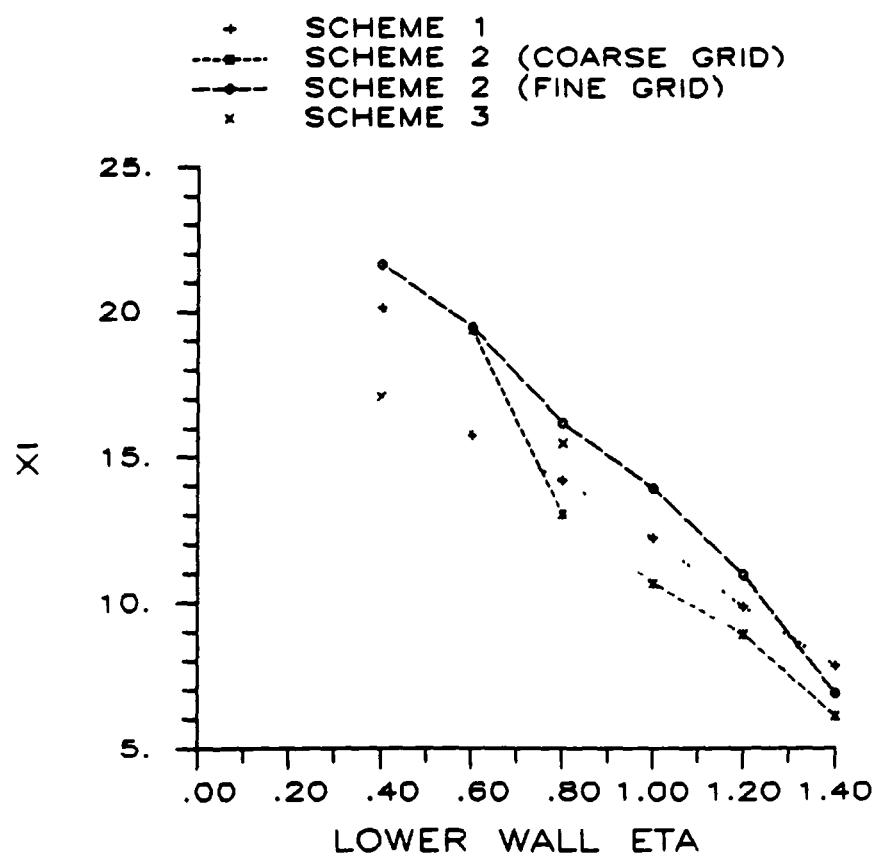
Fig. 9.13 Minimum M vs. η_o (η_i = 100).
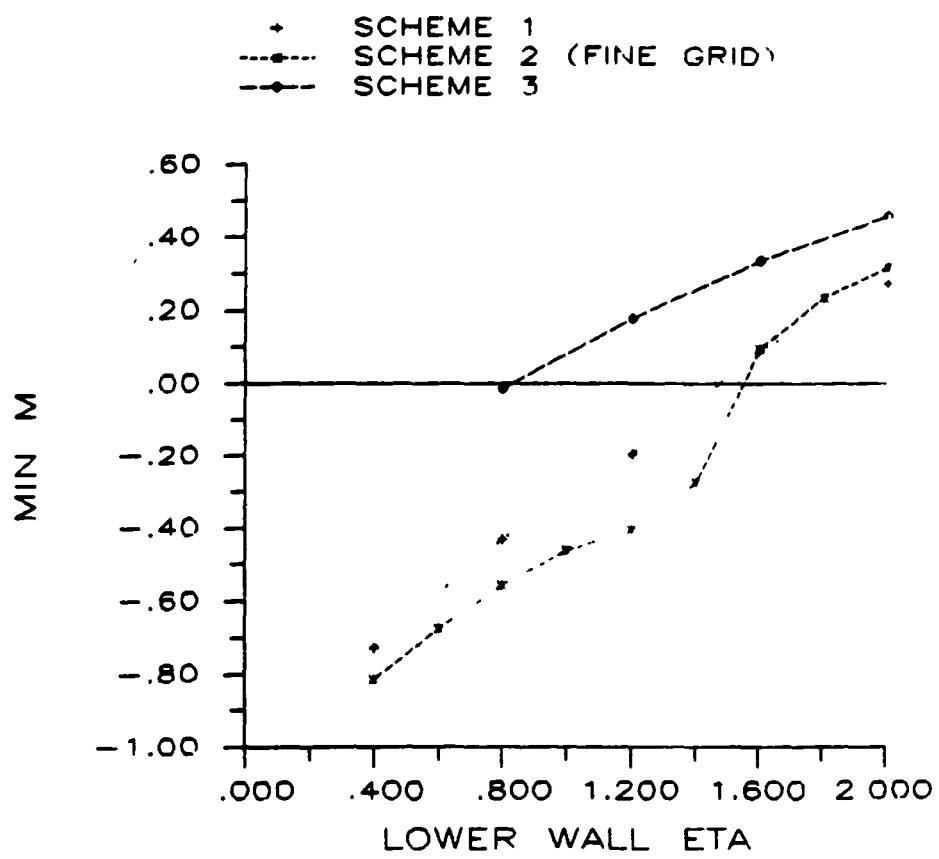
REATTACHMENT XI

+ SCHEME 1
---•--- SCHEME 2 (FINE GRID)
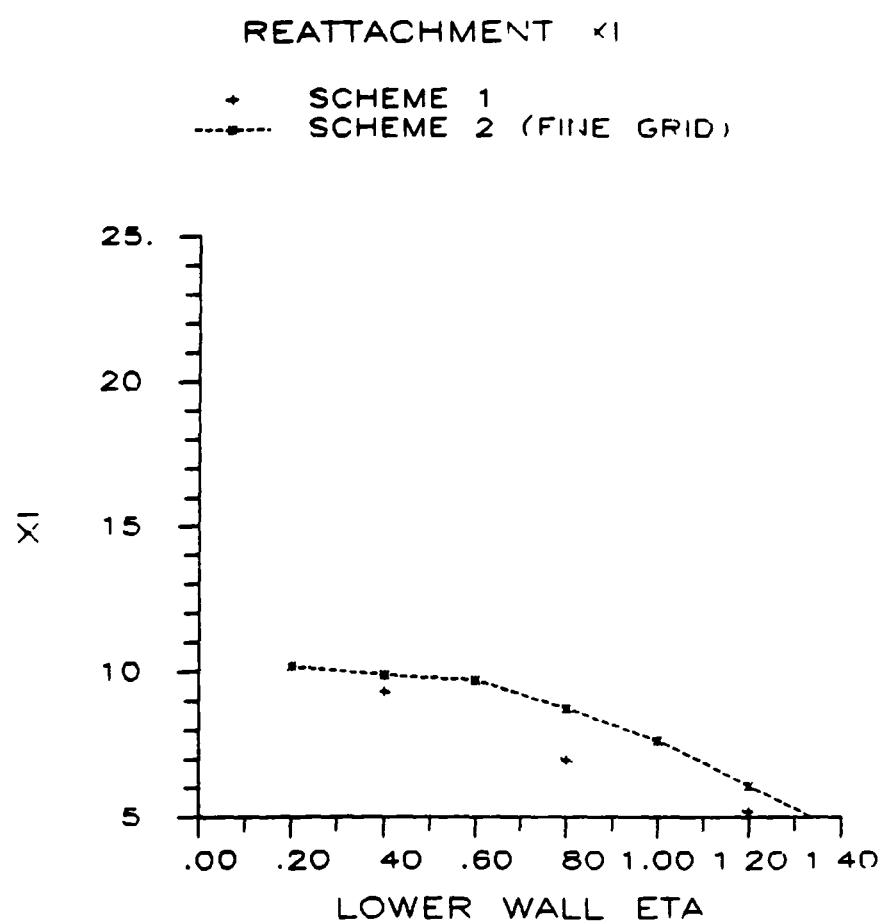
Fig. 9.14 Reattachment ξ vs. η_o (η_1 = 100).
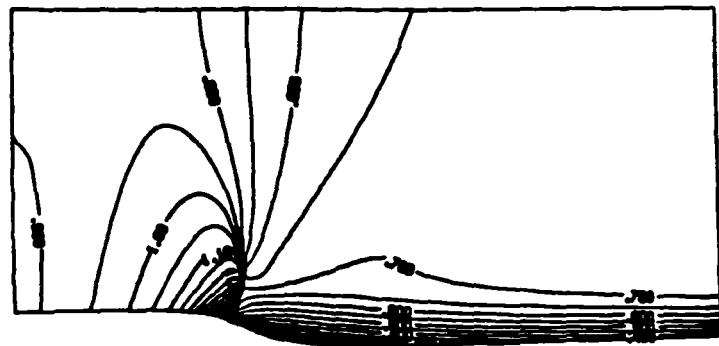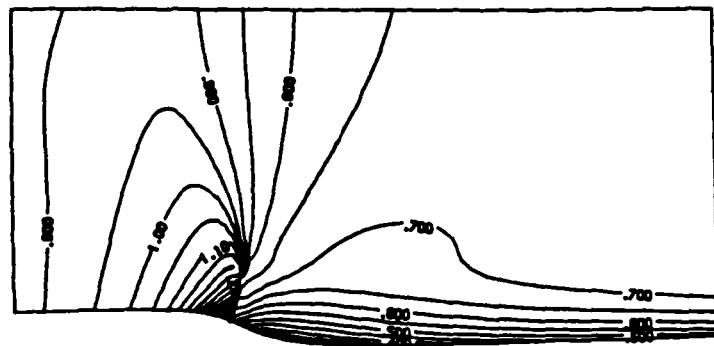
(a) Scheme One

(b) Scheme Two
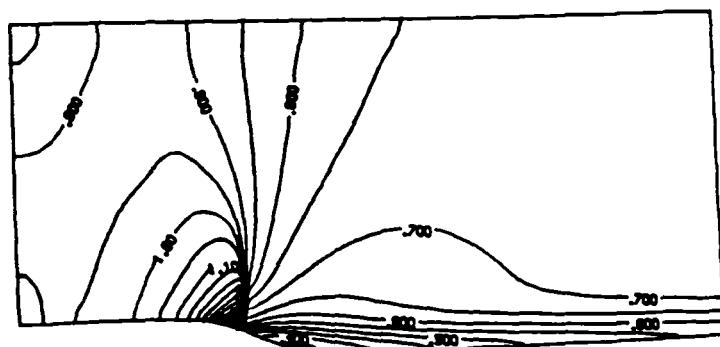
(c) Scheme Three

Fig. 9.15 Mach Contours $(\eta_0 = 2.0)$.
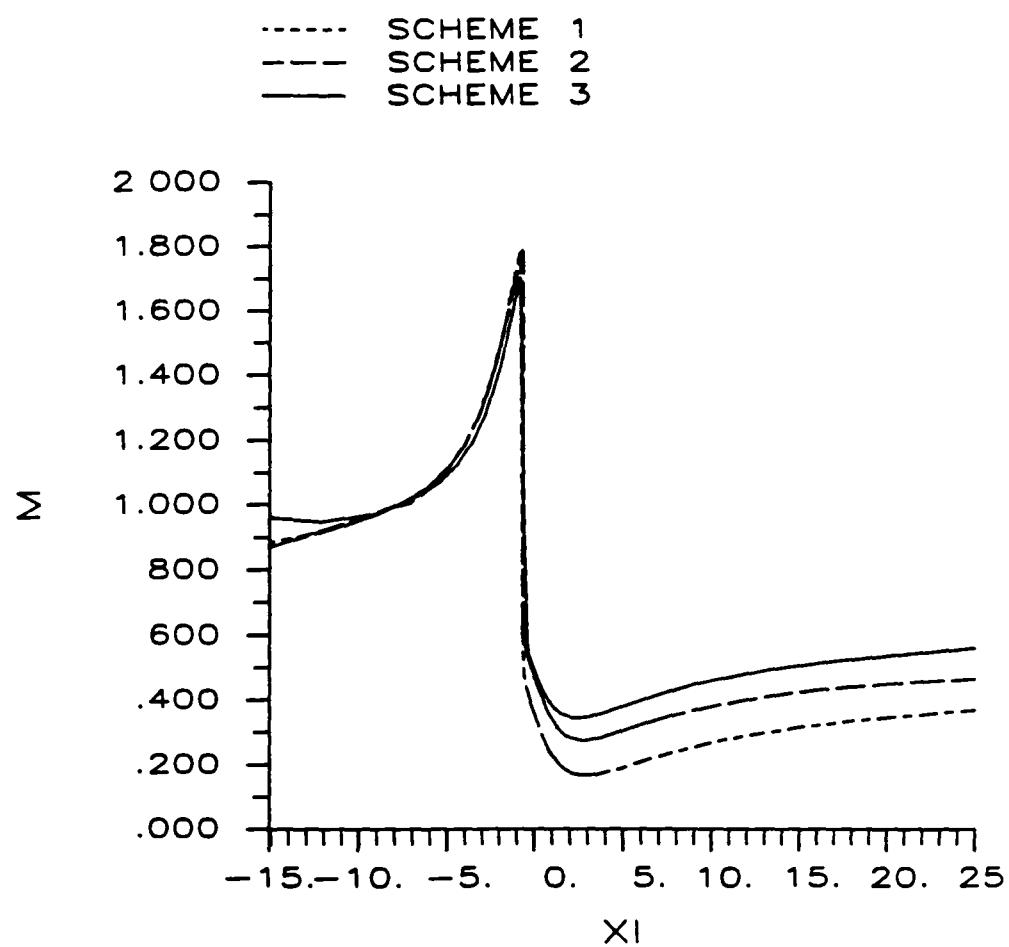
Fig. 9.16 Lower Wall M ($\eta_o = 2.0$).
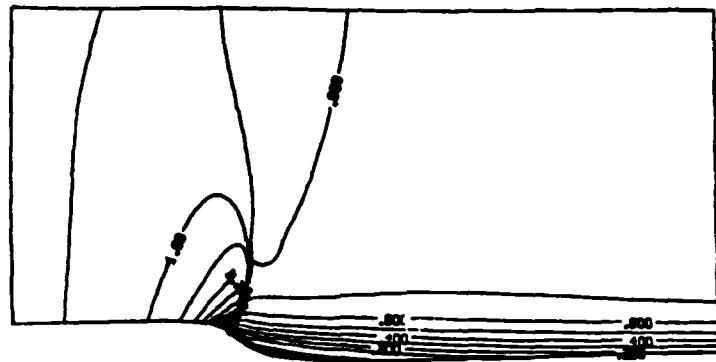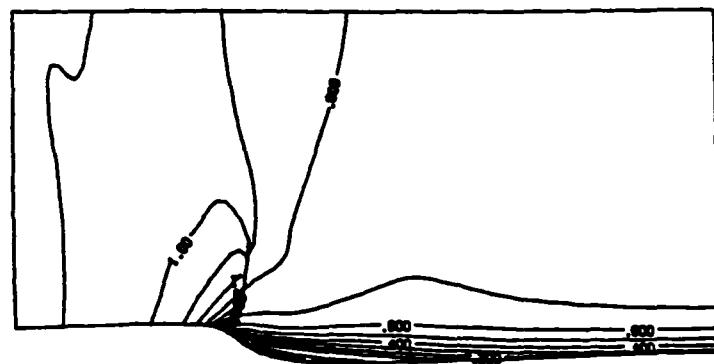
(a) Scheme One

(b) Scheme Two
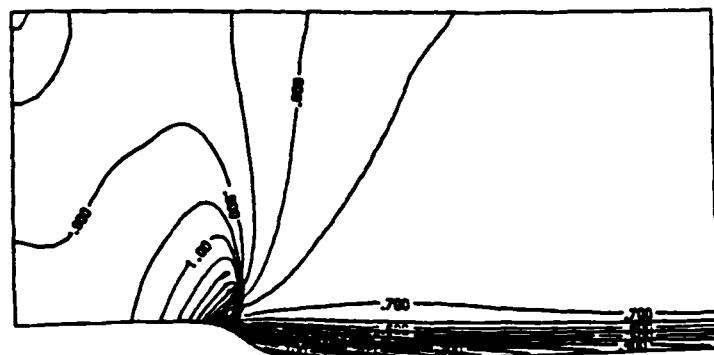
(c) Scheme Three

Fig. 9.17 Mach Contours $(\eta_0 = 1.2)$.
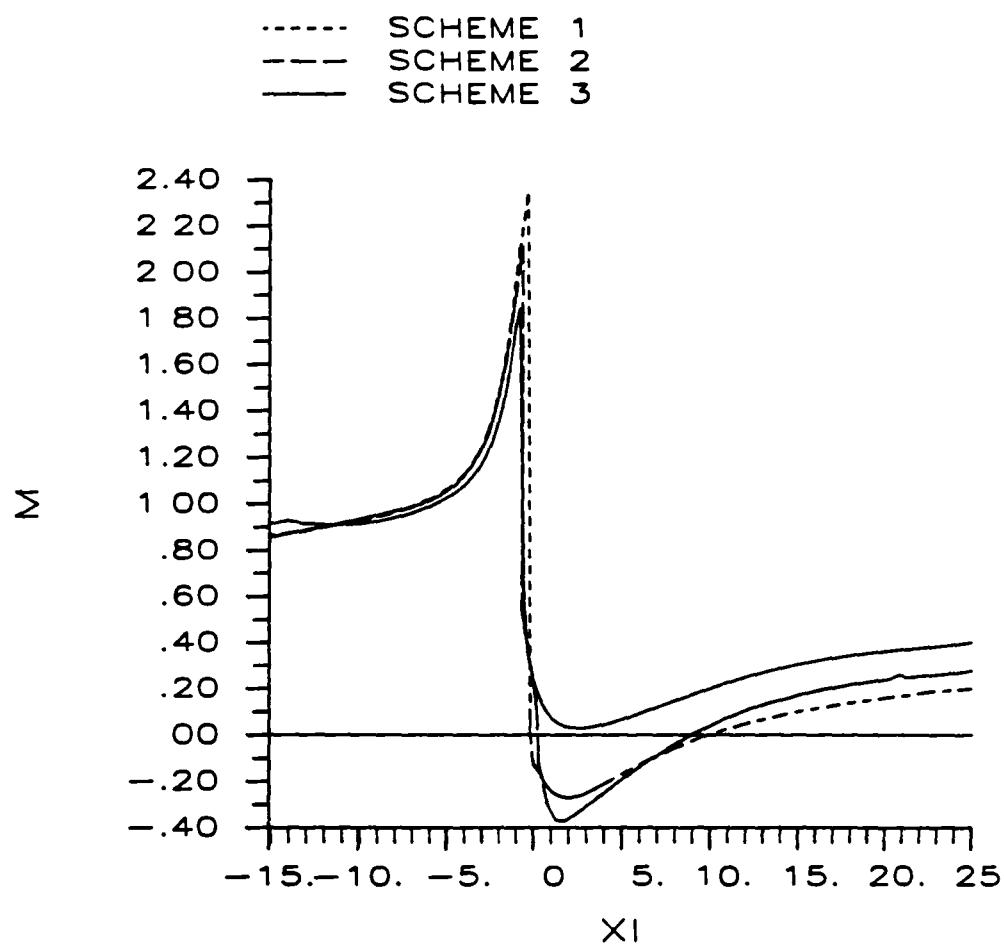
Fig. 9.18 Lower Wall M (η_0 = 1.2).
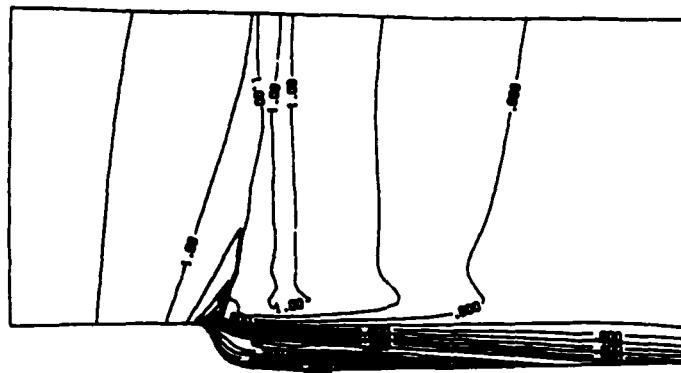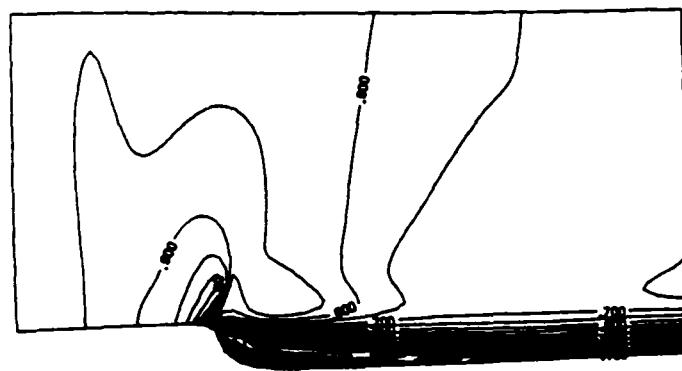
(a) Scheme One

(b) Scheme Two (81x41 grid)
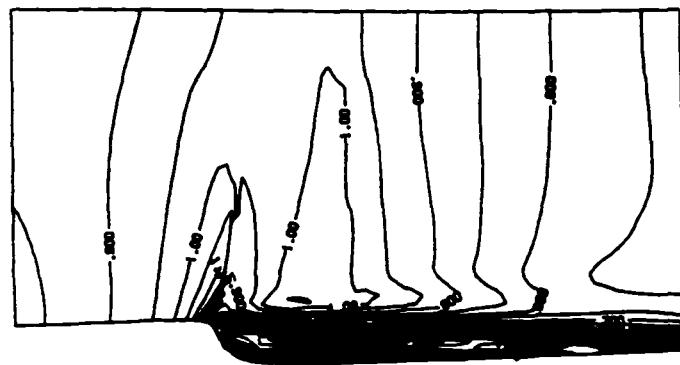
(c) Scheme Two (161x81 grid)

Fig. 9.19 Mach Contours ($\eta_o = 0.4$).
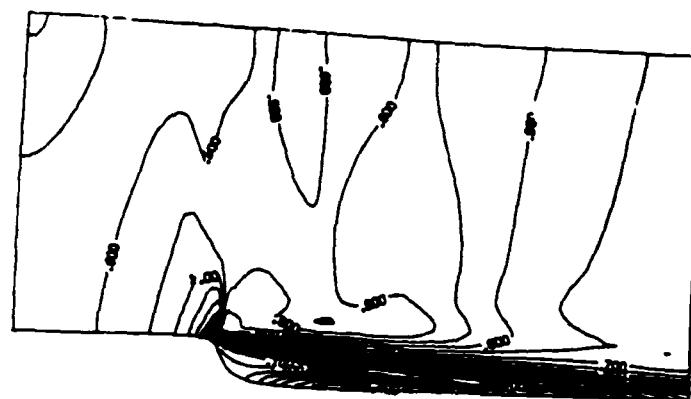
Fig. 9.19d Mach Contours - Scheme Four
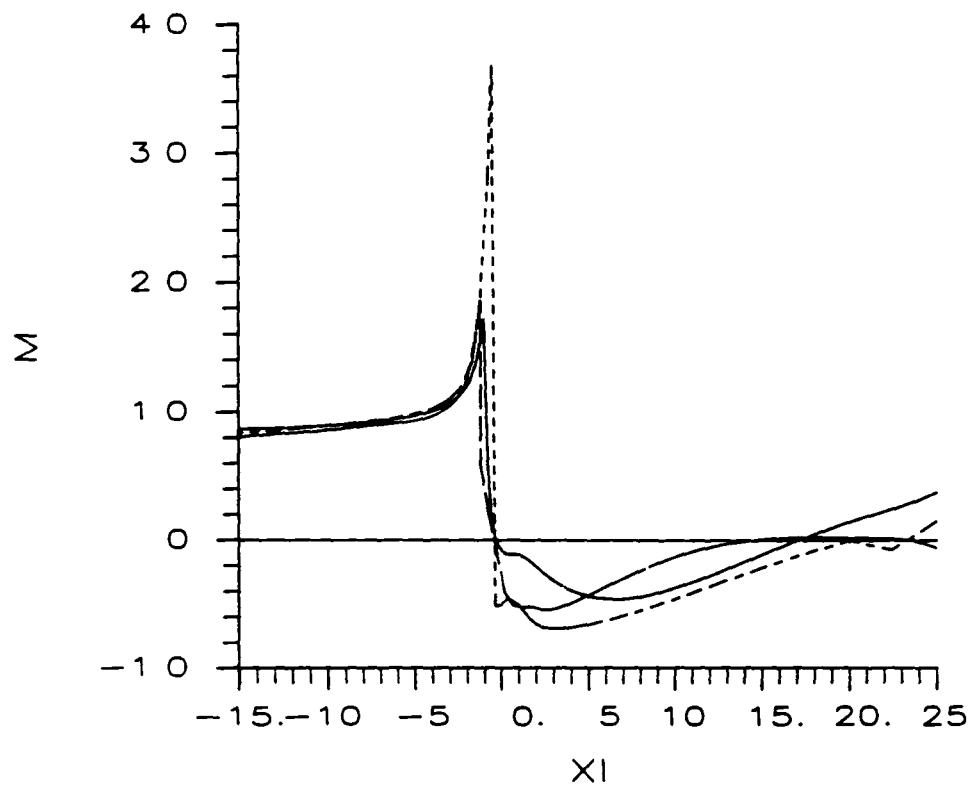
Fig. 9.20 Lower Wall M (η_o = 0.4).

using scheme one and Fig. 9.19c using scheme two on the fine grid both show a supersonic zone extending across the channel just downstream of the expansion corner which suggests that the flow is chocked in the channel and then expands supersonically as in a converging-diverging nozzle. The comparison of "M" vs. ξ in Fig. 9.20 shows that the flux vector splitting results show the least separation whereas the results from scheme one are the most separated.

The entropy produced by flow through the shock is shown in Figs. 9.21a-9.21c. These results were obtained using scheme two with the upper boundary $\eta_1 = 20$. In Fig. 9.21a, the lower boundary is at 2.0 and the maximum value of the entropy is 0.0878 just downstream from the shock along the wall. In Fig. 9.21b, the lower wall η_0 is at 1.6 and the maximum value of S is 0.126 and the entropy gradients are somewhat larger than in Fig. 9.21a. In Fig. 9.21c, the lower wall η_0 is at 1.2 and the maximum value of S is 0.145. It can be seen that there is a recirculation region and the entropy gradients are again greater than in the previous two cases with most of the entropy being produced very close to the lower boundary. These results correlate with Fig. 9.10, which shows the vorticity level increasing as η_0 is reduced and with Crocco's theorem which states the vorticity will exits in a flow if gradients of entropy and/or enthalpy also exist [60].

Figures 9.22 through 9.25 show the results of the flux splitting scheme three with the upper boundary at 40 and the lower boundary being reduced from 0.4 to 0.2 to 0.1. In Figs. 9.22a and 9.22b, the Mach contours and sonic line are shown for $\eta_0 = 0.4$ and the large separated zone downstream of the step and the shock at the expansion corner are evident. The Mach contours for $\eta_0 = 0.2$ in Fig. 9.23a and the

corresponding sonic line plot—in Fig. 9.23b show a much smaller supersonic zone at the corner and a slightly larger supersonic zone which is apparently not terminated by a shock just slightly downstream and above it. In Fig. 9.24a, the Mach contours for $n_0 = 0.1$ are shown and the corresponding sonic zones are given in Fig. 9.24b. It can be seen that the supersonic zone at the corner has nearly disappeared and the supersonic bubble out in the flow field has grown. The entropy contours shown in Fig. 9.24c and the stream function plot in Fig. 9.24d show clearly the separation region with the entropy now associated with the rotating vortex. Figure 9.25 shows the portion of the grid around the expansion corner and the resolution which is achieved at the corner by the special clustering.

A similar procedure was done using the same scheme but with the upper boundary instead at $n_1 = 20$. The results at $n_0 = 0.1$ are shown in Figs. 9.26 and 9.27. Figure 9.26a shows the Mach contours and it is apparent that a shock has formed which extends across the channel downstream of the expansion corner as was noted earlier. There is a large supersonic zone as is shown in Fig. 9.26b, which is terminated by the shock. The flow has separated from the corner and there is entropy trapped inside the recirculation region as shown in Fig. 9.26c. Figure 9.27 shows the Mach numbers multiplied by the sign of the contravarient velocity in the streamwise direction. The location of the shock at the expansion corner and at the top wall are clearly evident. It is also apparent that the shock at the expansion corner is still fairly strong and may not be going to zero as n_0 approaches 0.
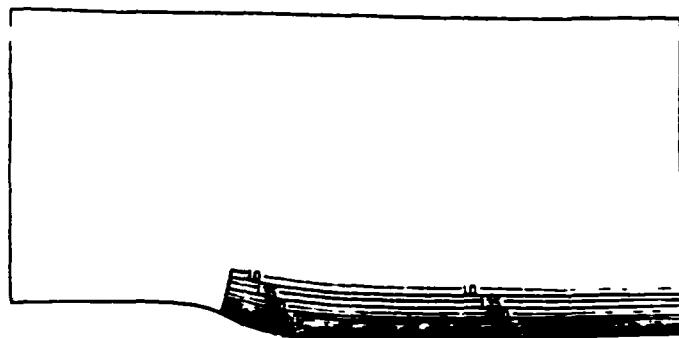
(a) $\eta_0 = 2.0$
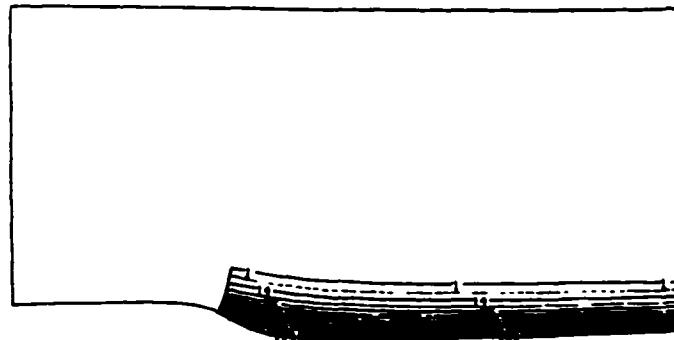
(b) $\eta_0 = 1.6$
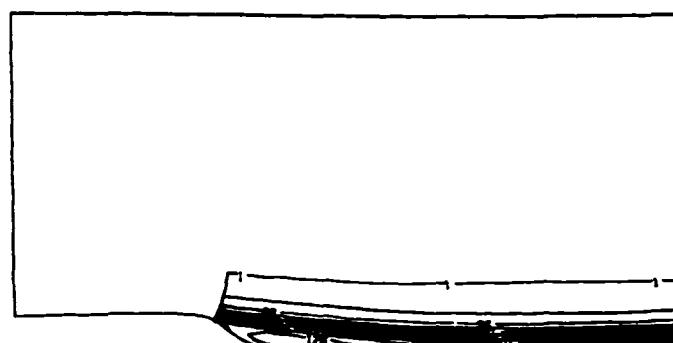
(c) $\eta_0 = 1.2$

Fig. 9.21 Entropy Contours.
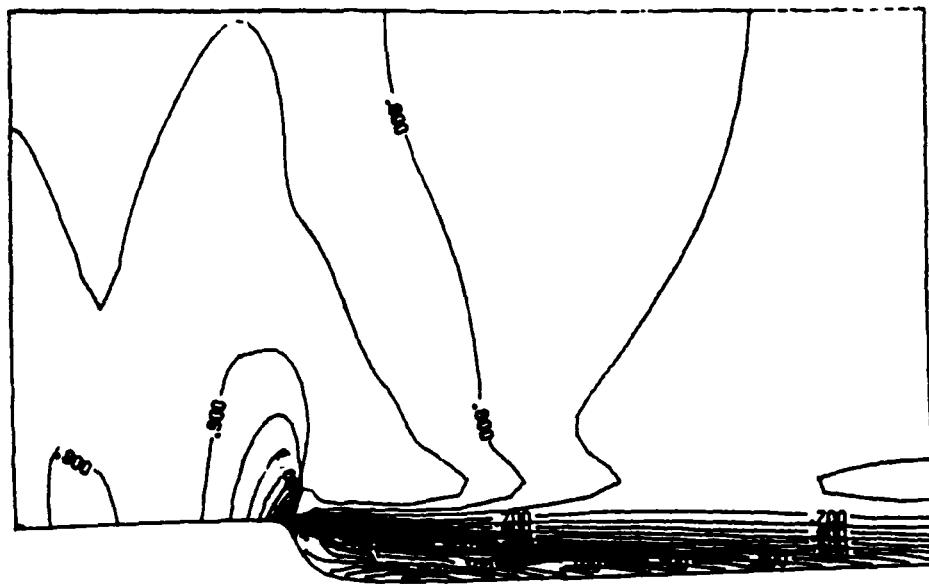
(a) Mach Contours
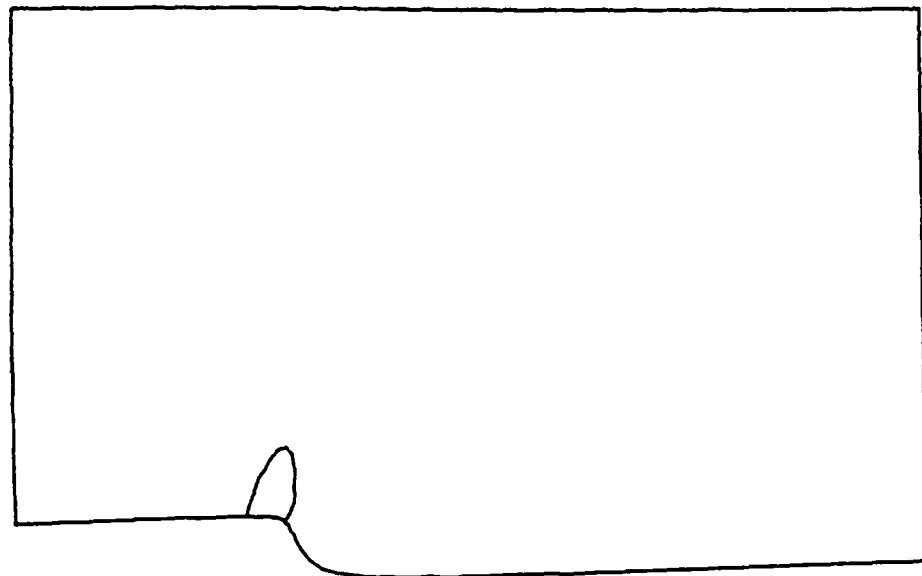
(b) Sonic Line

Fig. 9.22 Results – Scheme 3 (η_o = 0.4, η_I = 40).
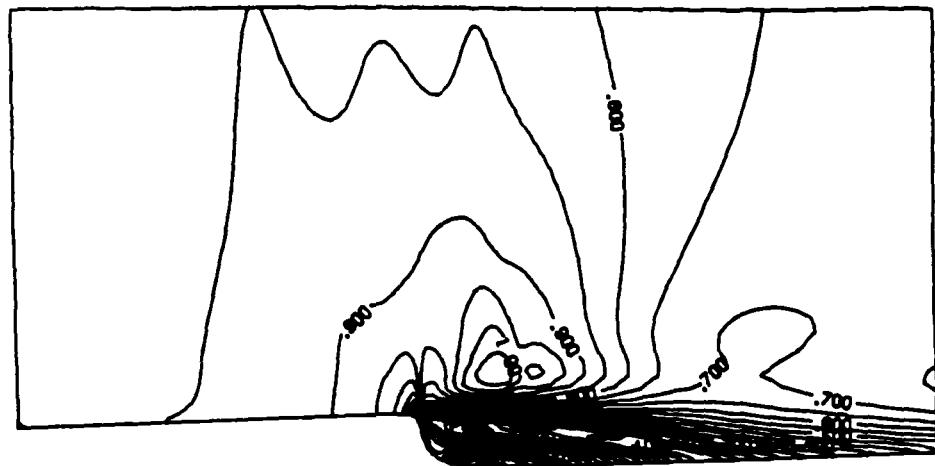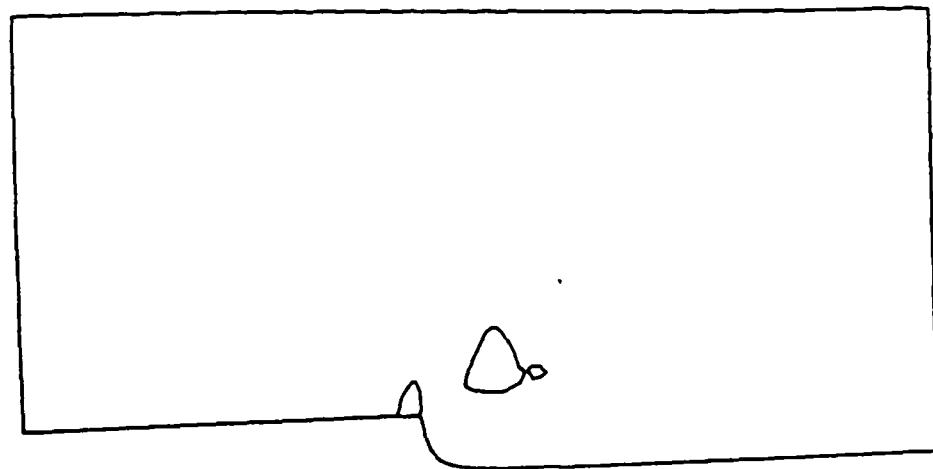
(a) Mach Contours

(b) Sonic Line

Fig. 9.23 Results - Scheme 3 (η_o = 0.2, η_I = 40).
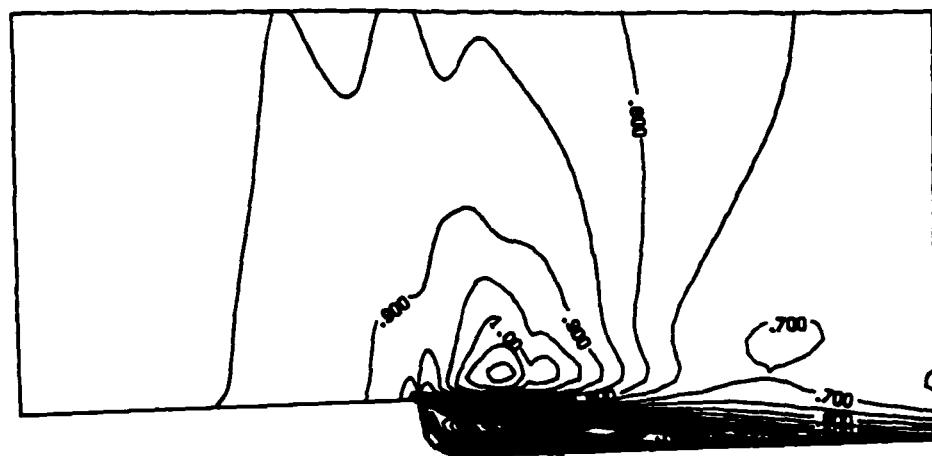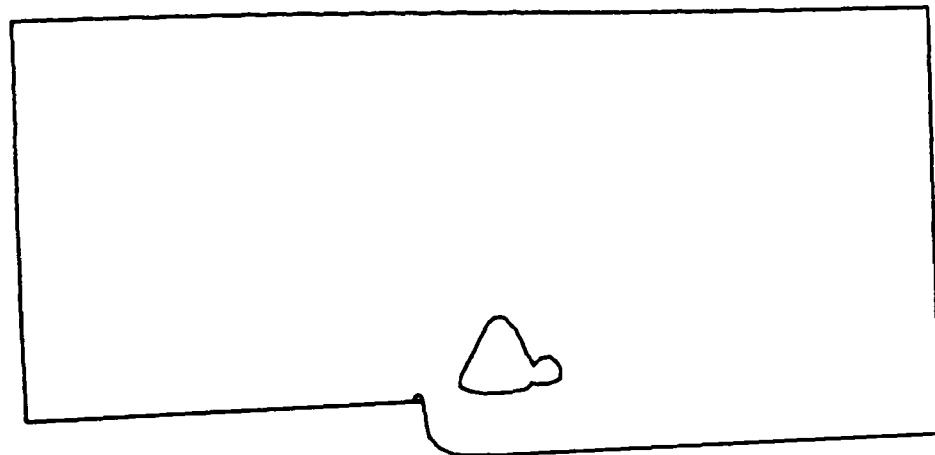
(a) Mach Contours

(b) Sonic Line

Fig. 9.24 Results – Scheme 3 ($\eta_0 = 0.1$, $\eta_1 = 40$).
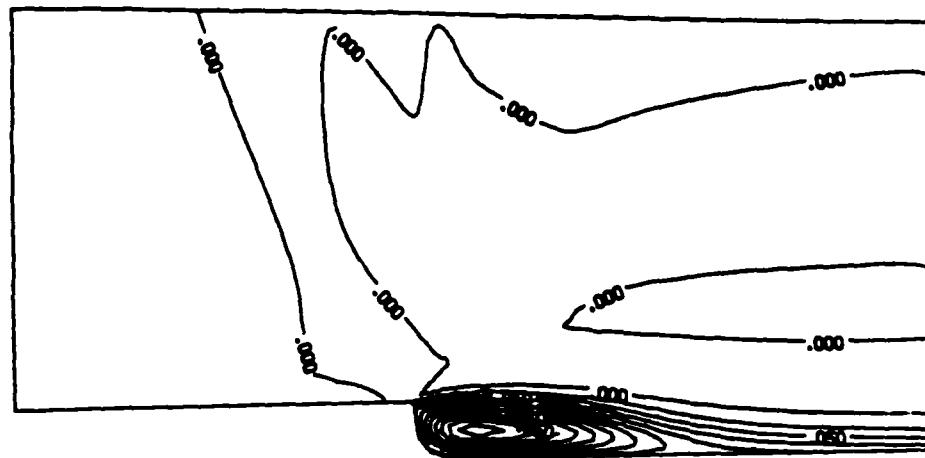
(c) Entropy Contours
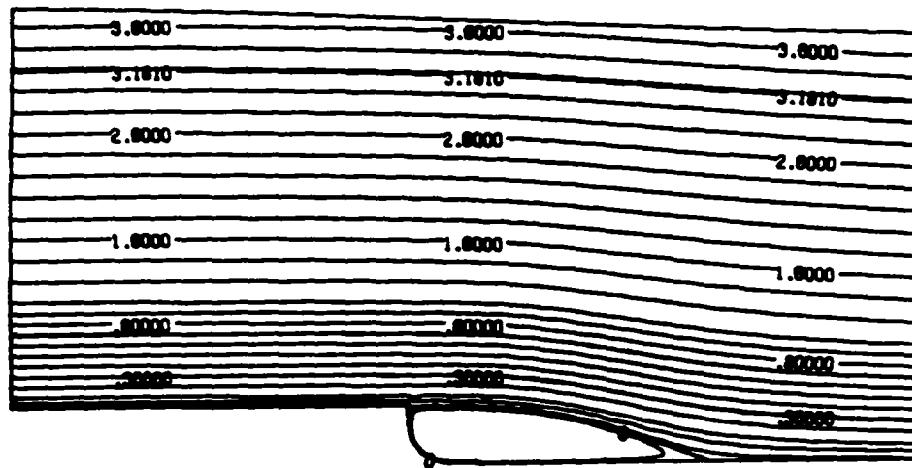
(d) Stream Function Contours

Fig. 9.24 (continued).
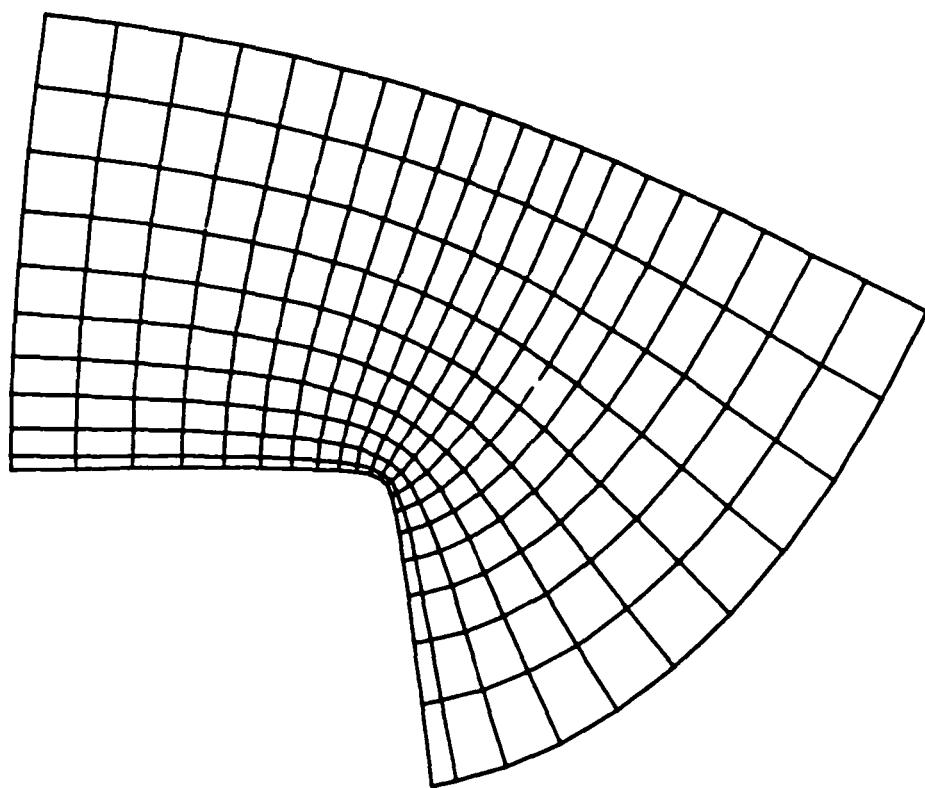
Fig. 9.25 Grid Detail at Corner.
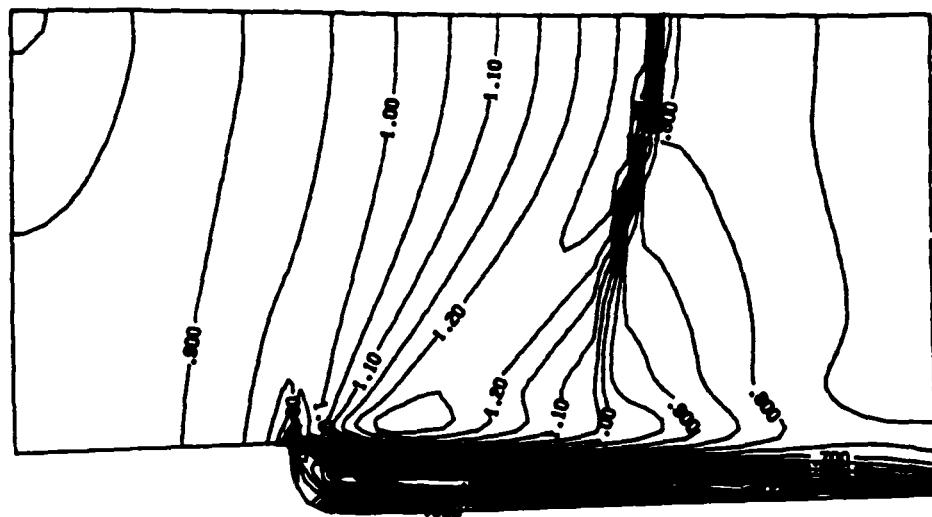
(a) Mach Contours
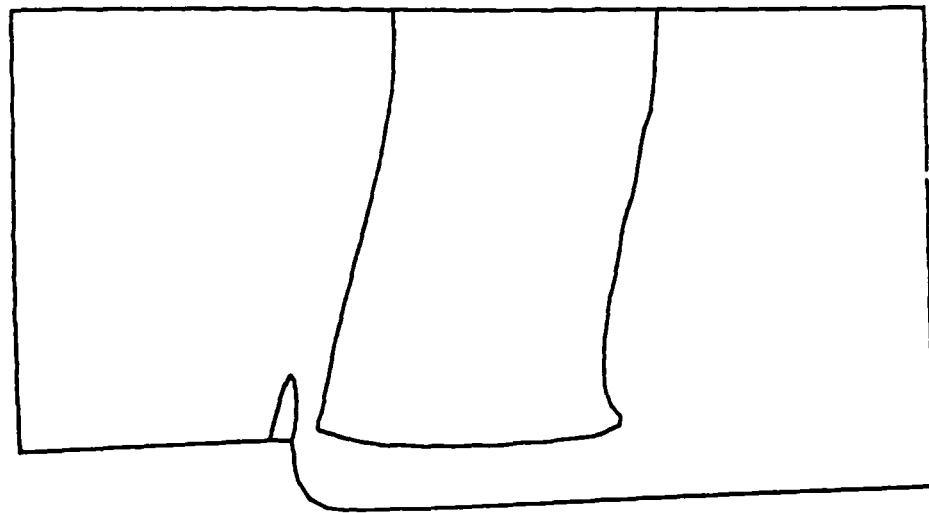
(b) Sonic Line

Fig. 9.26 Results - Scheme 3 (η_0 = 0.1, η_1 = 20).
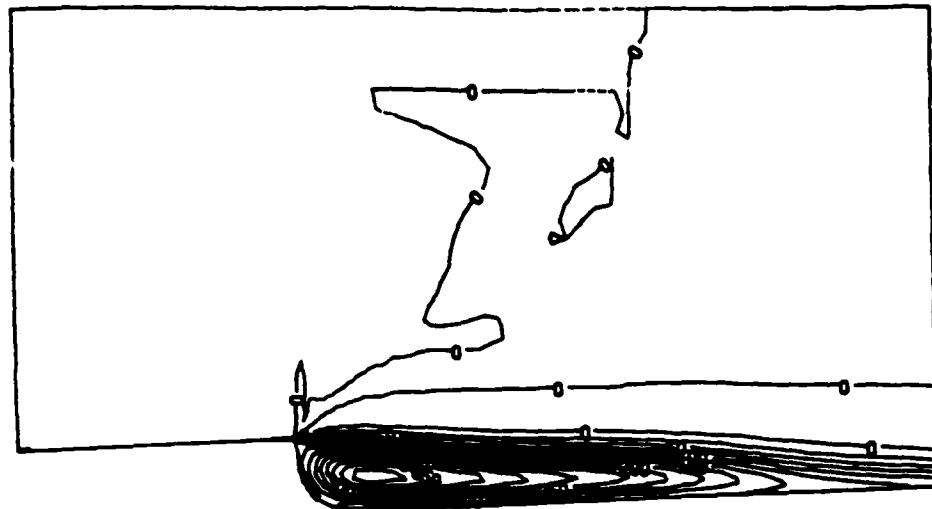
Fig. 9.26(c) Entropy Contours
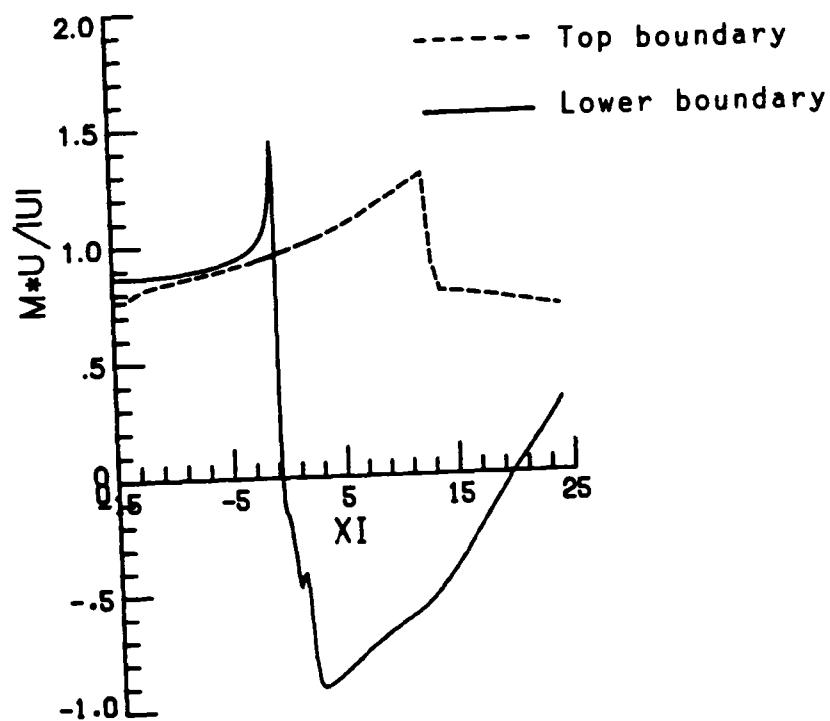
Fig. 9.27 Lower Wall M — Scheme 3 ($\eta_o = 0.1$, $\eta_1 = 20$).

9.1.2 <u>Viscous Results</u>

The Navier-Stokes scheme four has run on the rearward facing step under a variety of conditions. The purpose of the runs was to determine how the viscous results might differ from the inviscid results. No attempt was made to duplicate all of the various positions of the lower wall n_0 and the upper wall n_1 due to the time and computational expense that would be necessary to do this and also because, as will be seen, the results that were obtained were so different from the inviscid results that this was felt by the writer to be unnecessary.

The first set of runs was done using a Reynolds number of 10,000 with the upper boundary at n_1 = 40 and the lower boundary at n_0 = 2. A grid size of 81x61 was used and the first point off the wall was at n = 0.01. A constant global time step of 0.2 was used at the solution was run for 3000 iterations and plots obtained at 1500, 2000, 2500 and 3000 iterations. Figure 9.28 shows the results at 1500 iterations. From the Mach contours in Fig. 9.28a, it is evident that the boundary layer which begins upstream of the corner separates at the corner and that there is no shock there. The solution throughout the flow field is fairly smooth and the freestream upper boundary condition does not appear to be causing any flow abberations. Figure 9.28b shows the pressure contours and the presence of at least one vortex is apparent from the circular pattern with a low pressure center. Figure 9.28c shows the velocity vectors and this large vortex is apparent along with two other smaller vorticies upstream. The wall shear stress plot in Fig. 9.28d provides further evidence of flow reversal along the lower wall between approximately ξ = -4.6 and ξ = -1 and also in the vicinity of $10 < \xi < 17$.
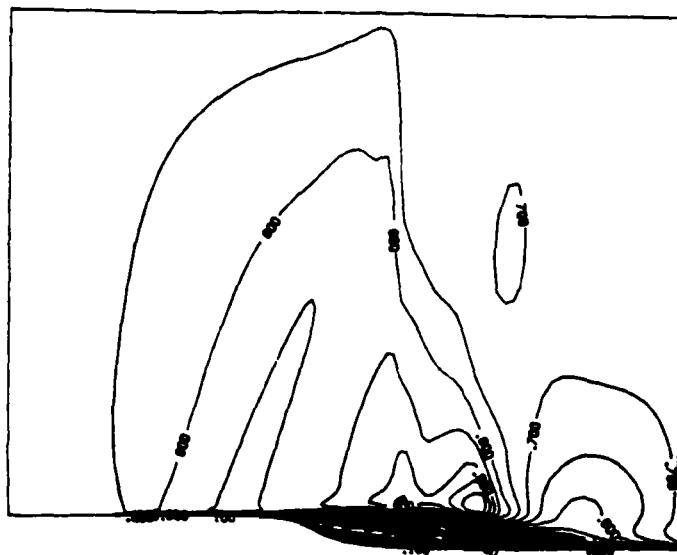
(a) Mach Contours
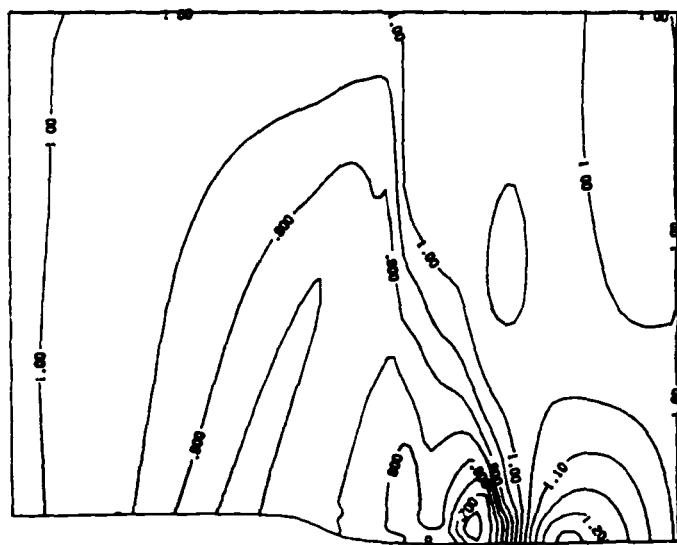
(b) Pressure Contours

Fig. 9.28 Results - Scheme 4 (1500 iterations).
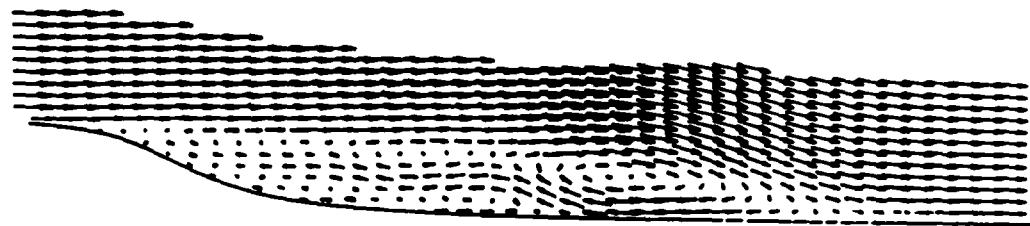
(c) Velocity Vectors
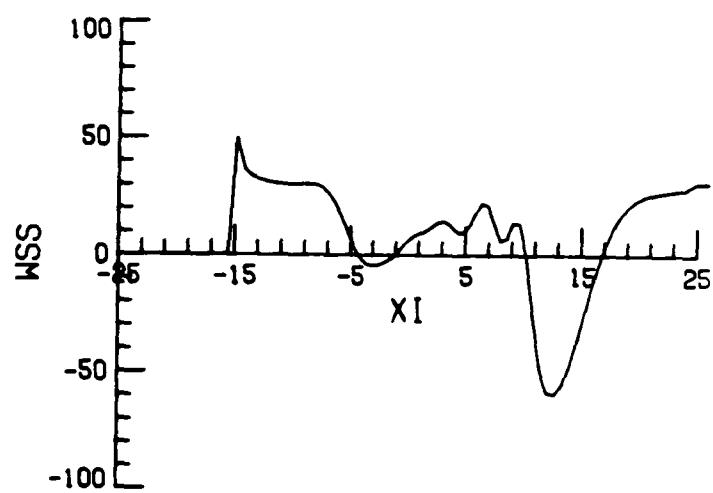
(d) Wall Shear Stress

Fig. 9.28 (continued).

The results of 2000 iterations are shown in Figs. 9.29a through 9.29d. A comparison between Figs. 9.28a and 9.29a shows that the flow field has changed greatly in that the extent of the separation zone has grown and there now appears to be more disruption of the flow field above the separated region. The pressure contours in Fig. 9.29b an the velocity vector plot in Fig. 9.29c show the presence of two large vorticies downstream of the corner. The wall shear stress plot in Fig. 9.29d shows a third reverse flow region in the region of $-5 < \xi < -1$ ahead of the step.

Ther results at 2500 iterations are shown in Figs. 9.30a through 9.30d and it is apparent that the location of the vortices has again changed which indicates that either the flow has not reached a final steady state or the flow may be unsteady. The writer considers the later possibility to be the more likely. One large vortex is present just downstream from the corner and the writer believes it is possible that this may be the small vortex which was just beginning to form at 2000 iterations and has now moved further downstream and grown. At the same time, the two large vortices that were present at 2000 iterations have been swept out of the computational region. Again, from the wall shear stress plot in Fig. 9.30d it is apparent that a smaller reverse flow region appears to exist inside the boundary layer ahead of the step. This region has not changed location significantly from the previous two iterations and it may be a permanent feature that has established itself and may be giving rise periodically to shed vortices which are then swept downstream.

The results at 3000 iterations are shown in Figs. 9.31a through 9.31d and again the flow field appears to have changed. Although the
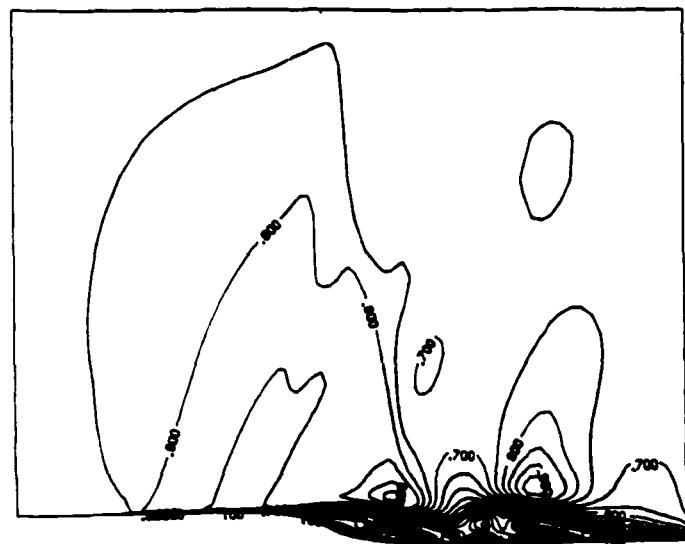
(a) Mach Contours
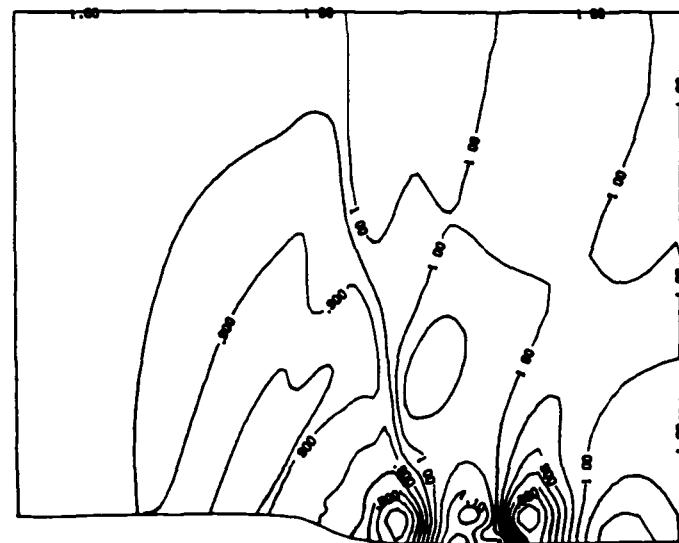
(b) Pressure Contours

Fig. 9.29 Results - Scheme 4 (2000 iterations).
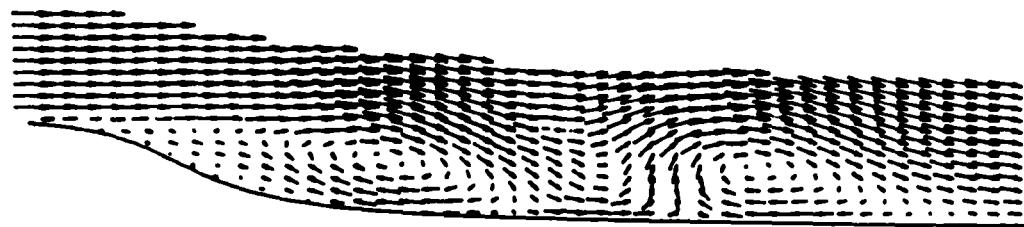
(c) Velocity Vectors
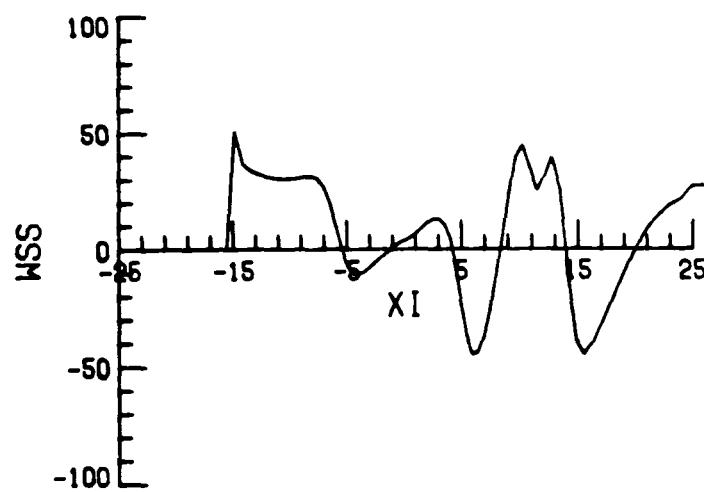
(d) Wall Shear Stress

Fig. 9.29 (continued).

Mach contours in Fig. 9.31a do resemble the Mach contours in Fig. 9.30a, the pressure contours in Fig. 9.31b now show a fairly strong adverse pressure gradient ahead of the corner which was beginning to become apparent in Fig. 9.30b. Figure 9.31b shows the presence of four circular shaped pressure regions of alternating high and low pressure. The velocity vector plots in Fig. 9.31c show two clockwise rotating vorticies which appear to correspond in location to the two low pressure regions in Fig. 9.31b. The high pressure regions appear to correspond to the regions where the flow velocities are low just downstream of the step and in between the two vorticies. The wall shear stress plot in Fig. 9.31d again shows a small recirculation zone ahead of the step which must lie inside of the boundary layer.

Two runs were also done at a Reynolds number of 100,000 and the results are compared in Figs. 9.32 and 9.33. The first run was done using an 81x61 grid with a freestream Mach number of 0.865 using a nondimensional time step of 0.02. The flow was assumed to be laminar and the turbulent terms were turned off. The Mach contour, pressure contour, wall shear stress, and velocity vectors after 2000 iterations are shown in Figs. 9.32a-9.32d respectively. It can be seen that the results are not appreciably different than the results at the lower Reynolds number shown previously. Ther are numerous recirculation vorticies present in the flow as can be seen from the velocity vector plot and there are no shocks in the flow. The second set of results was obtained using the same Reynolds number and time step but a 161x61 grid and the flow was assumed to be turbulent. The results after 2000 iterations are shown in Figs. 9.33a-33d. From the Mach and pressure contours and the wall shear stress plot, it is apparent that a strong
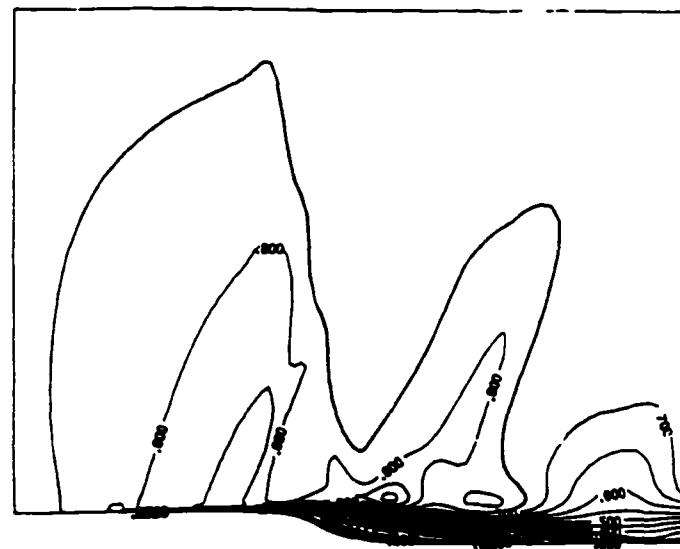
(a) Mach Contours
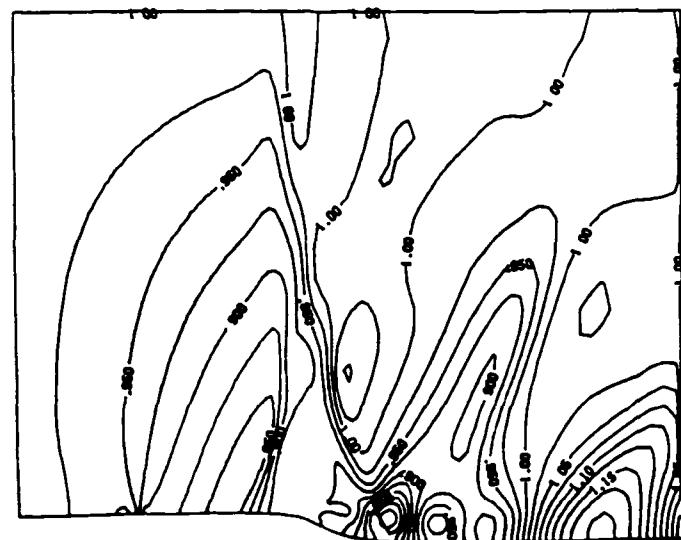
(b) Pressure Contours

Fig. 9.30 Results - Scheme 4 (2500 iterations).
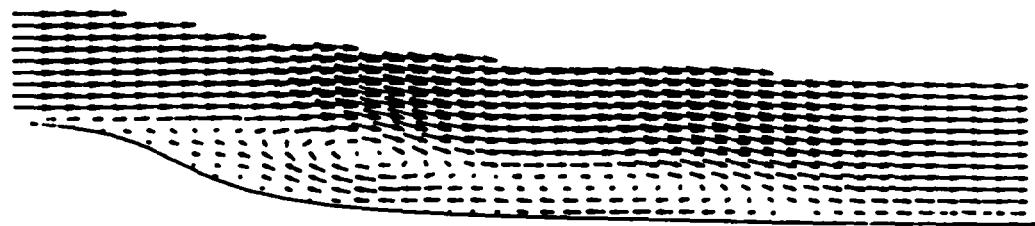
(c) Velocity Vectors
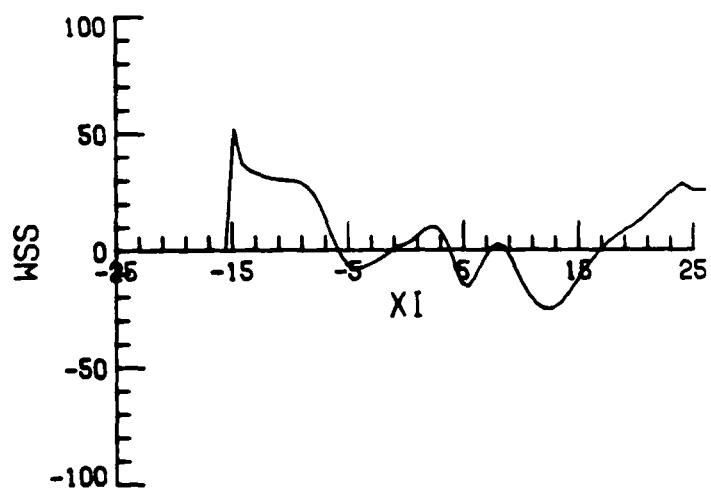
(d) Wall Shear Stress

Fig. 9.30 (continued).
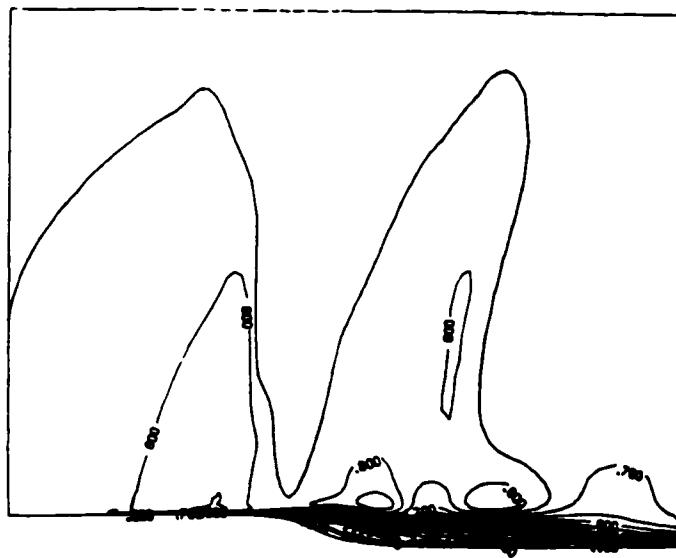
(a)   Mach Contours
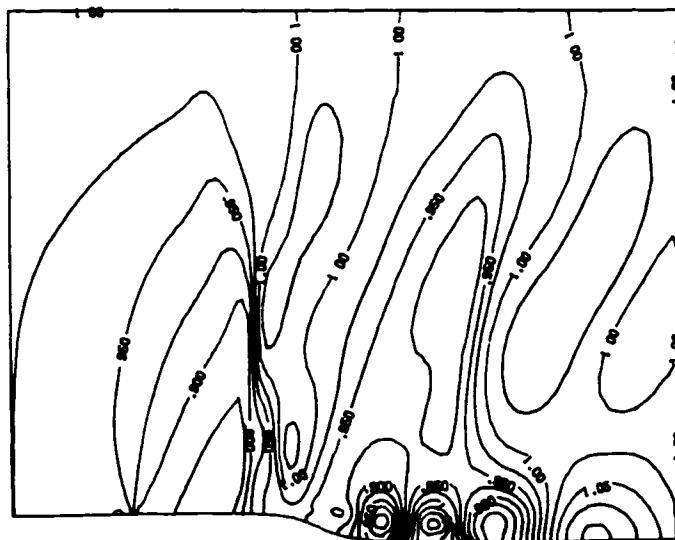
(b)   Pressure Contours

Fig. 9.31   Results - Scheme 4   (3000 iterations).

156
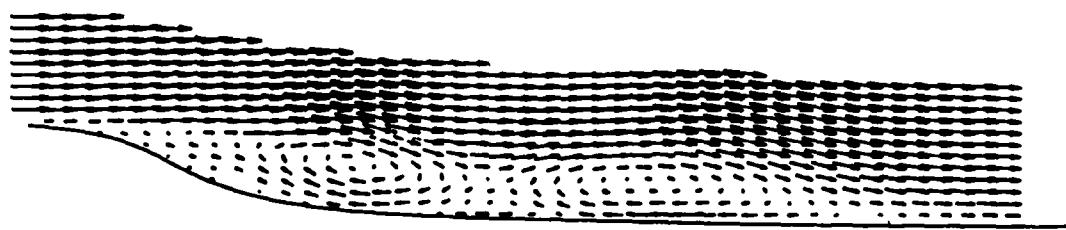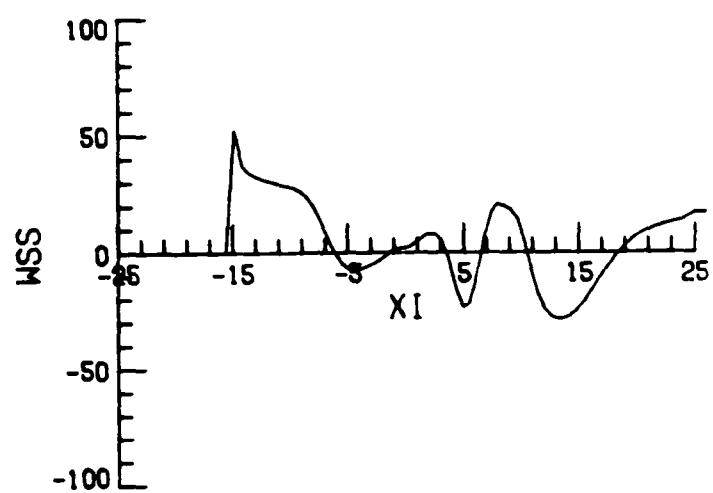
(c) Velocity Vectors

(d) Wall Shear Stress

Fig. 9.31 (continued).
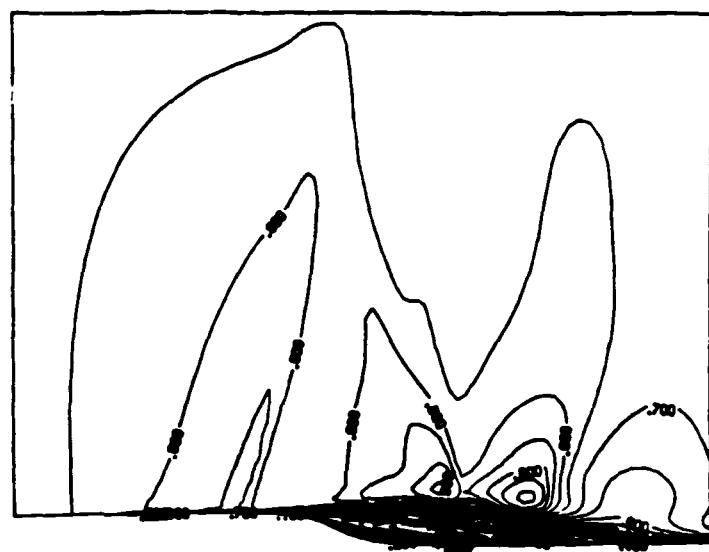
(a)   Mach Contours
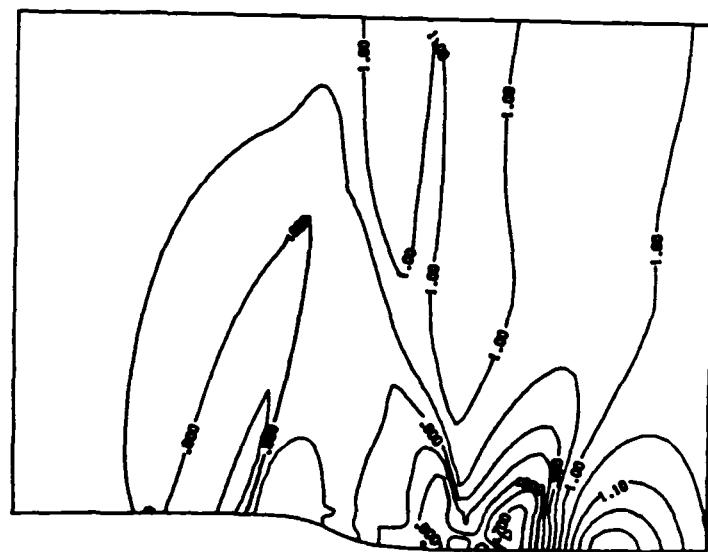
(b)   Pressure Contours

Fig. 9.32   Results - Scheme 4   (Re = 100,000).
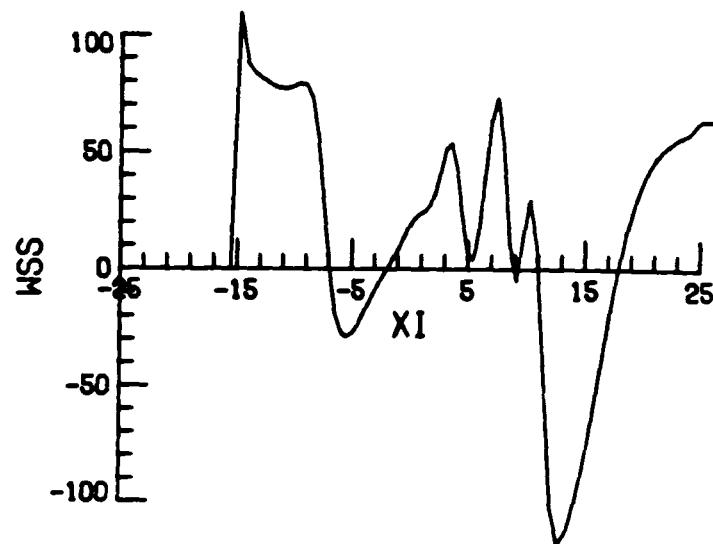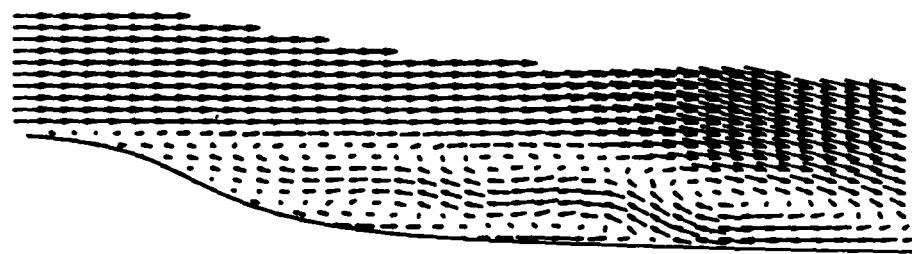
(c) Wall Shear Stress

(d) Velocity Vectors

Fig. 9.32 (continued).
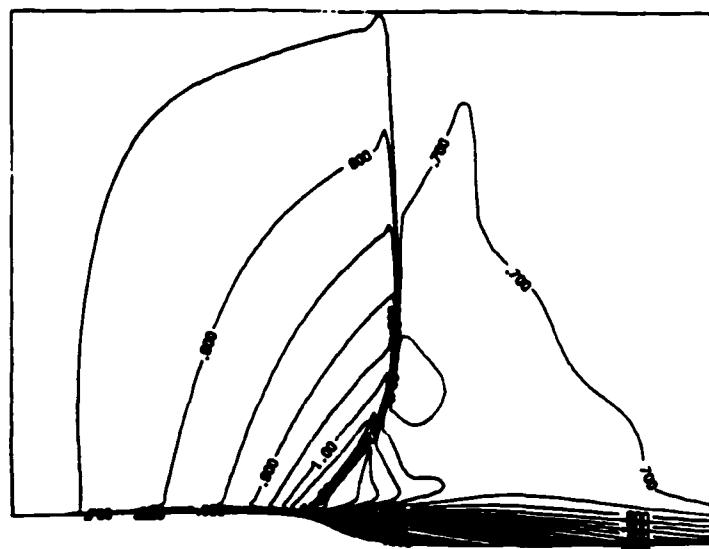
(a) Mach Contours
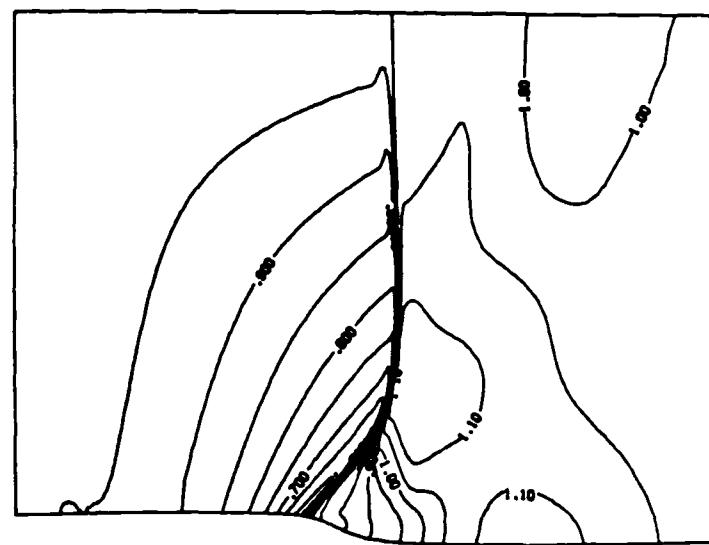
(b) Pressure Contours

Fig. 9.33 Results – Scheme 4 (Re = 100,000).
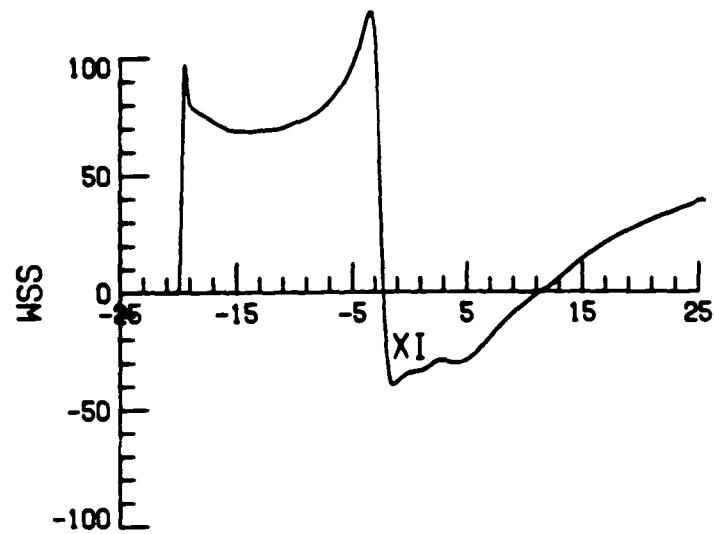
(c) Wall Shear Stress
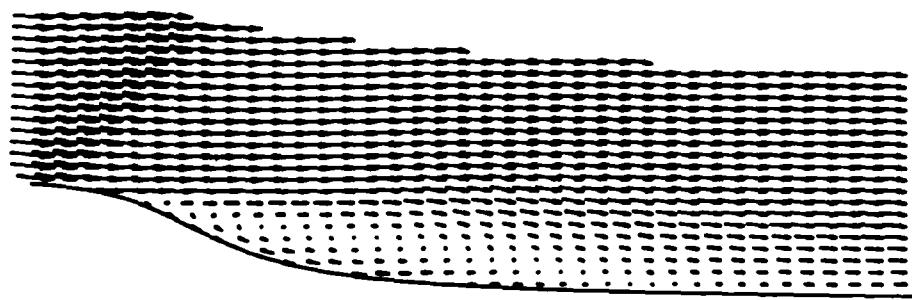
(d) Velocity Vectors

Fig. 9.33 (continued).

shock now exists across the channel similar to some of the inviscid cases. Furthermore, the velocity vector plots show only a single recirculation vortex which is also similar to the inviscid cases. It thus appears that putting the turbulence model into use results in a flow pattern that strongly resembles some of the inviscid results.

9.2 Problem Two

9.2.1 Inviscid Results

The second configuration, a "bump" inside a channel, was treated in a manner similar to the rearward facing step. The three inviscid schemes were all run on 81x41 grids and the shock fitting scheme two was also run on a fine grid 161x81 for comparison. The Navier-Stokes code was run on an 81x61 grid and the results from using this code is discussed in the next section. In all cases, the upper wall η_1 was set at 12.0 and the left and right boundaries were set at $\xi = -10.0$ and +10.0 respectively. The lower wall η_0 was varied from a maximum of 1.0 to a minimum of 0.2 in the inviscid cases. The back pressure boundary condition was that the nondimensional pressure p' is 0.5.

Figure 9.34 shows the Mach number on the upstream side of the shock foot for the various cases which were run. The shock capturing results from scheme one again show that as the lower wall η_0 is reduced and the expansion becomes greater that the Mach number ahead of the shock increases much faster than the other schemes which is a result of the nonconservative nature of the scheme. The shock fitting results on both the coarse and fine grids agree fairly closely with the Mach number increasing to about 2.2 as the lower wall η_0 is reduced. The flux vector splitting scheme three results show lower Mach numbers than the

MACH NO AT SHOCK

--▲-- SCHEME 1
—◆— SCHEME 2 (COARSE GRID)
--◆— SCHEME 2 (FINE GRID)
--✱-- SCHEME 3
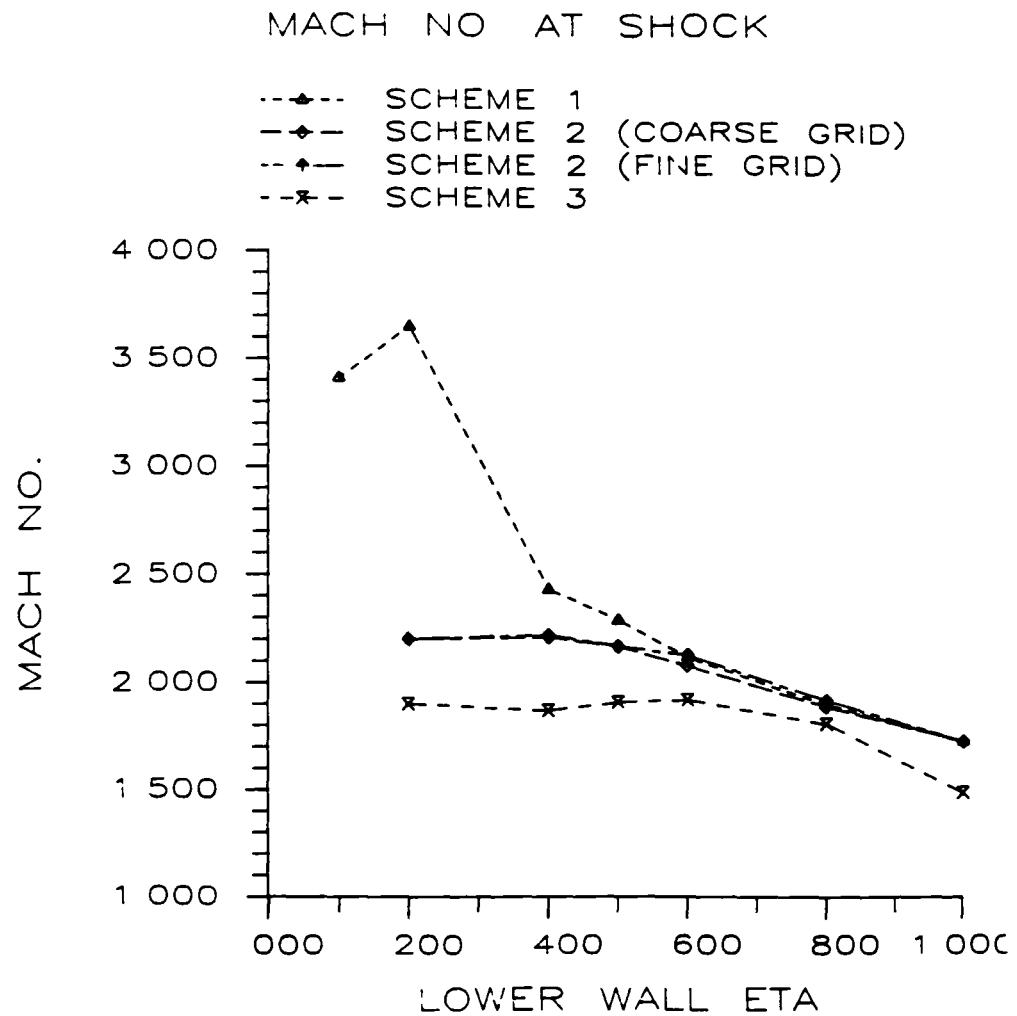
Fig. 9.34 Mach No. vs. η_0.

two previous schemes and this is consistent with the results of problem one. The maximum Mach number achieved with scheme three is 1.92 at n_0 equal to 0.6.

Figure 9.35 shows the shock locations for the four sets of results. The scheme one shock location is consistently greater than 1.4 and reaches a maximum of 1.61 at $n_0 = 0.2$. It should be noted that since the grid is fixed in cases one and three, the shock location shifts of increment of one grid point and cannot achieve intermediary values. The shock fitting scheme two results show that the shock location starts out at the same location as scheme one but that as the lower wall n_0 is reduced, the ξ is gradually reduced to about 0.7 at a lower wall n_0 of 0.2. The results of scheme three are similar at n_0 equal to 0.2, the ξ is 0.53.

Figures 9.36 and 9.37 show the entropy and vorticity downstream of the shock adjacent to the wall. In Fig. 9.36, it can be seen that as the lower wall is reduced the entropy produced by flow through the shock tends to increase in all cases. The shock captured solutions of scheme one show less entropy than the results of the shock fitting scheme or the flux vector splitting scheme three. The results of schemes two on both the coarse and fine grids and scheme three agree fairly closely. In Fig. 9.37, it can be seen that in all cases the vorticity is increased as the lower wall n_0 is reduced. However, the actual levels of vorticity vary depending on the scheme. The flux vector splitting scheme three shows the least the amount of vorticity present in the flow; however, this may be due to the fact that the function values in scheme three are cell volume average instead of point values and this is reflected in the way the values are reported out.

SHOCK LOCATION

---▲--- SCHEME 1
—◆— SCHEME 2 (COARSE GRID)
—●— SCHEME 2 (FINE GRID)
--✕-- SCHEME 3
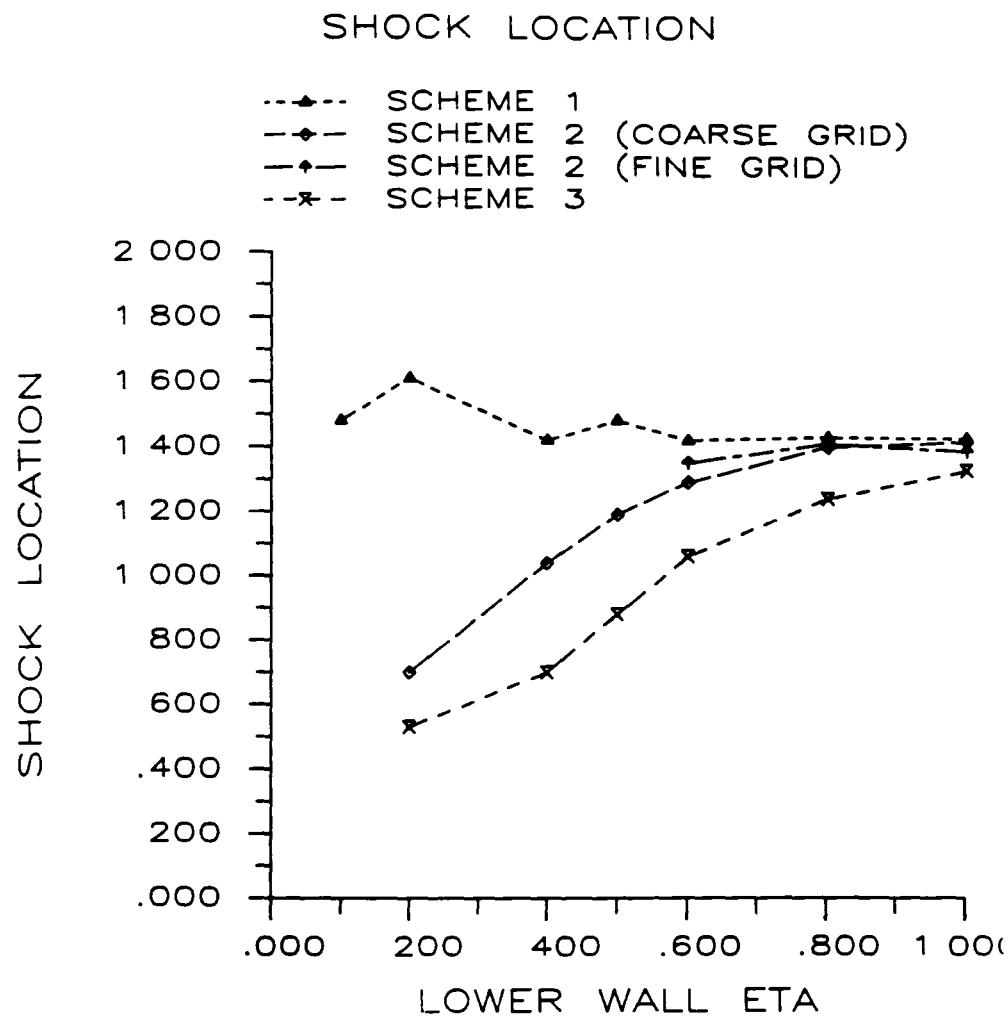
Fig. 9.35 Shock Location vs. η_o.
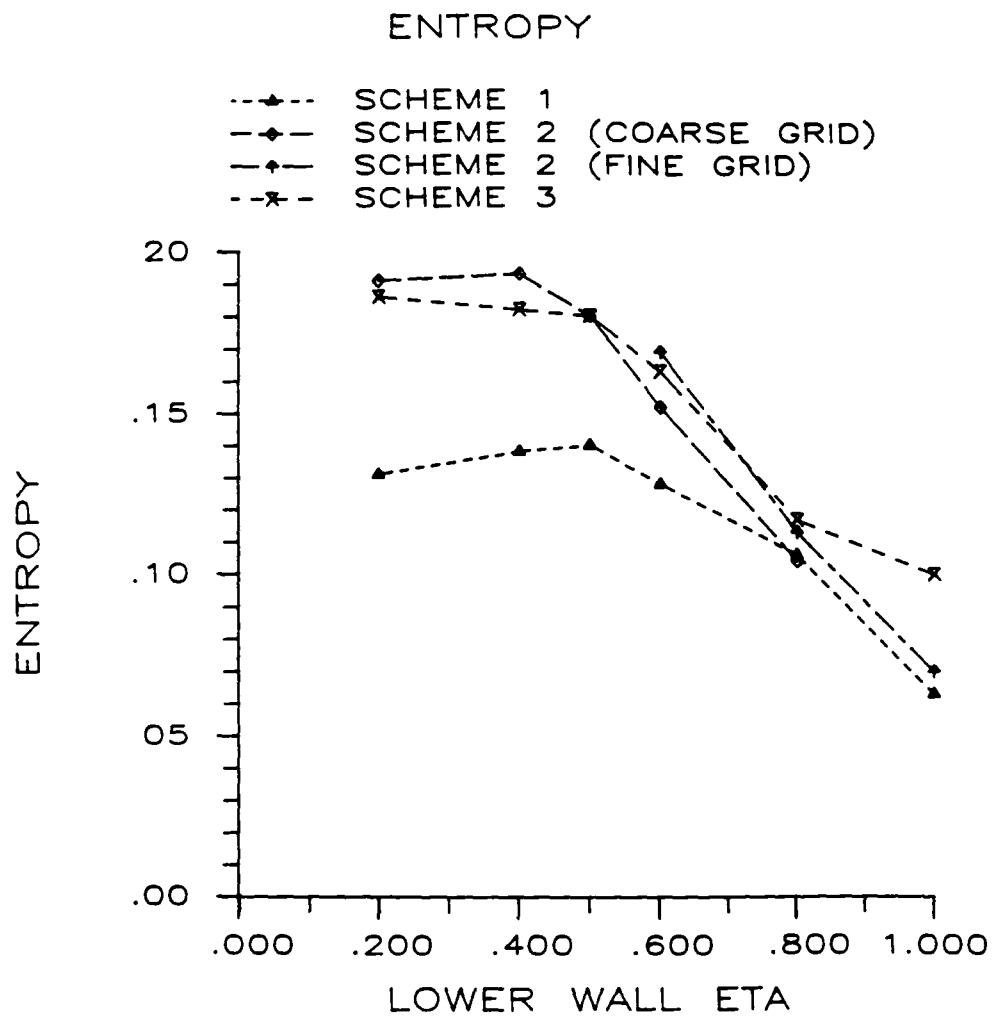
ENTROPY

Fig. 9.36 Entropy Downstream of Shock.

VORTICITY

|	
--▲--	SCHEME 1
—◆—	SCHEME 2 (COARSE GRID)
—✦—	SCHEME 2 (FINE GRID)
--✻--	SCHEME 3
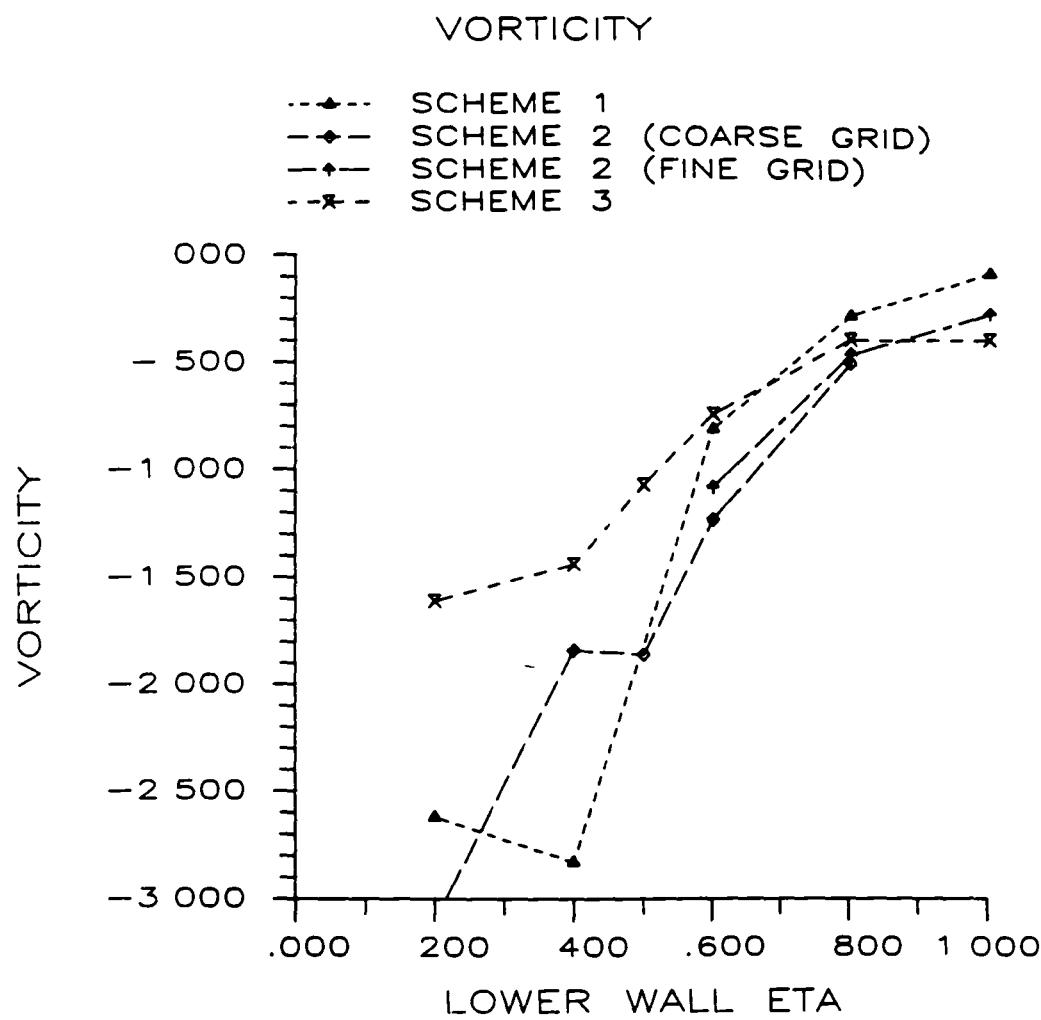
Fig. 9.37 Vorticity Downstream of Shock.

The minimum Mach numbers multiplied by the sign of the contravarient velocity component along the lower wall for the various cases are shown in Fig. 9.38. The results all indicate that as n_0 is reduced, the value of M decreases and that the shock fitting results on the coarse grid were the first to separate which is not the same as problem one when the scheme one results were the first to separate. In general, however, the results in Fig. 9.38 show a fairly high degree of consistency. The ξ location of the flow reattachment shown in Fig. 9.39 indicate that the results of scheme one generally show a smaller separation zone than either shock fitting scheme two or the implicit shock fitting scheme three.

A comparison of the results of the three schemes for the case with the lower wall n_0 equal to 1.0 is shown in Figs. 9.40a-9.40d. From the Mach number contours which are shown, it can be seen that the results are all similar. The fine grid shock fitting results are not as well converged as the coarse grid results since both runs were for 1000 iterations and the fine grid case would need probably 2000 iterations (which would take 8 times as long since there are roughly four times as many points as the coarse grid) to get to the same level of convergence.

A similar comparison is shown in Figs. 9.41-9.41d. The Mach contours produced by scheme one are very similar to those produced by scheme two and, in fact, if the two plots are overlaid, the contours are seen to be nearly identical throughout the flow field except close to the shock. The flux vector splitting Mach contours show a smaller sonic region but overall are similar to the results of schemes one and two. A comparison of the Mach number multiplied by the sign of the contra-varient U shows that the jump through the shock is significantly less with scheme three than with schemes one and two.

Fig. 9.38 Minimum M vs. η_o.

REATTACHMENT XI

---•--	SCHEME 1
---•---	SCHEME 2 (COARSE GRID)
---•--	SCHEME 2 (FINE GRID)
x	SCHEME 3
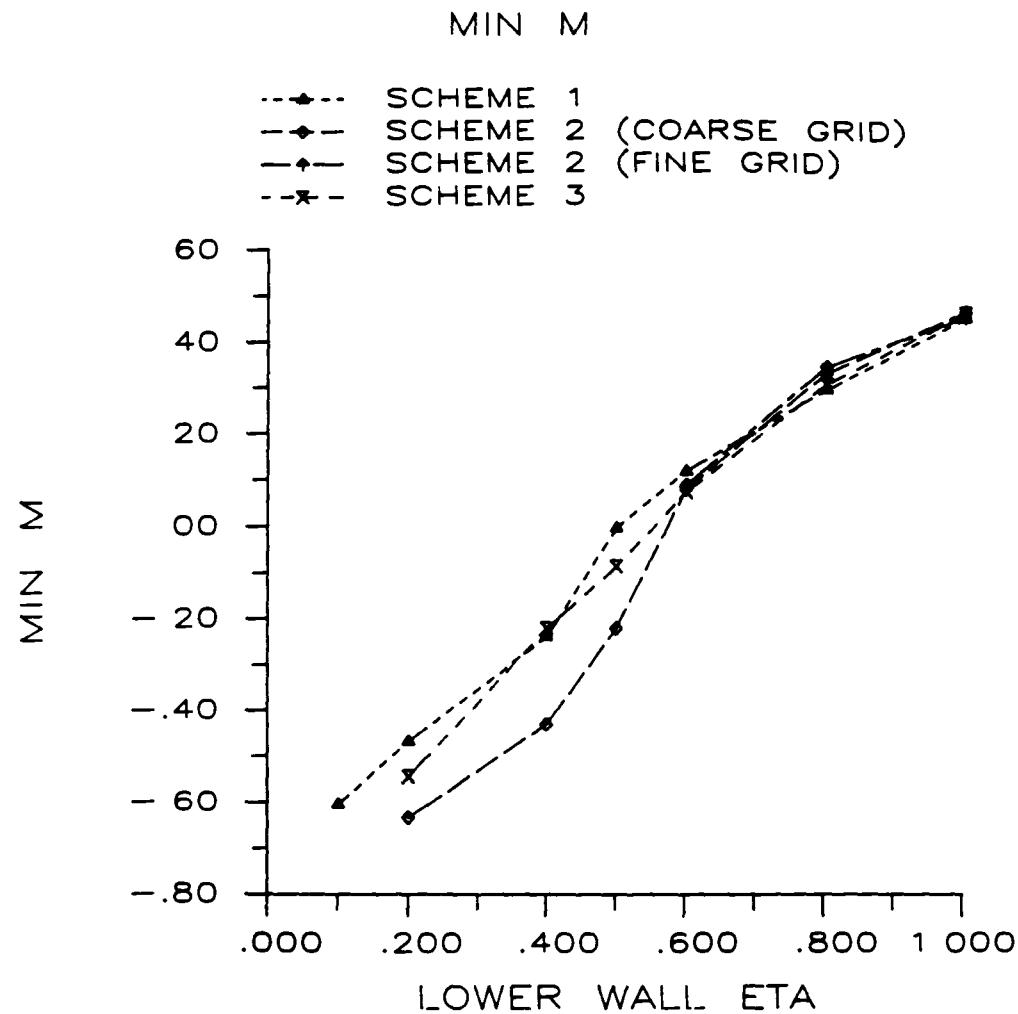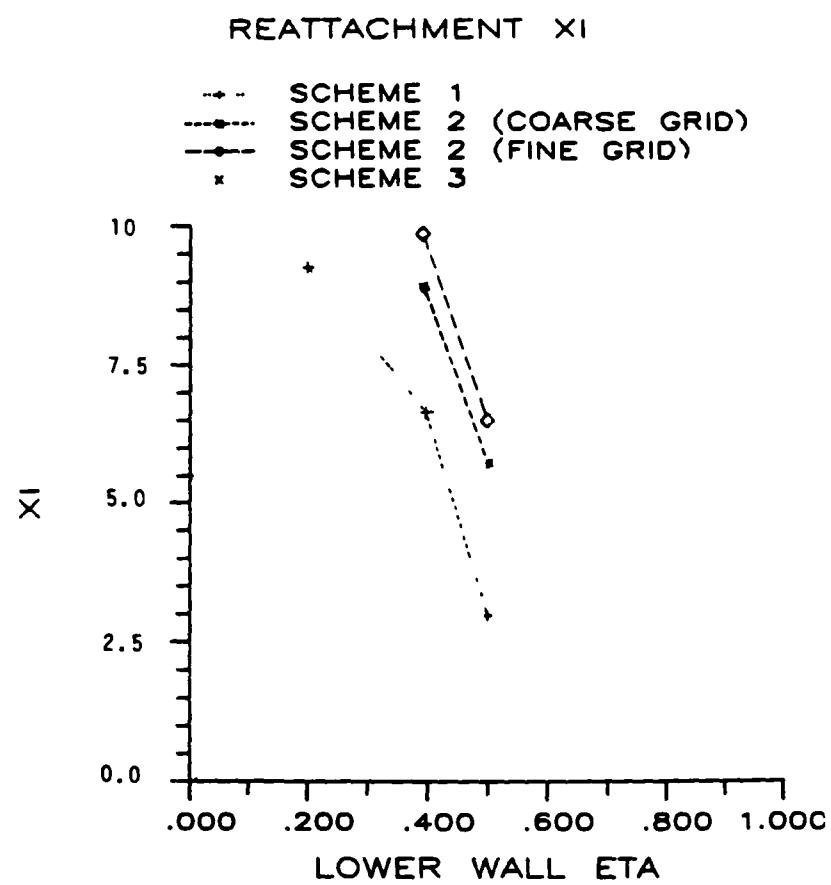
Fig. 9.39 Reattachment ξ vs. η_o.
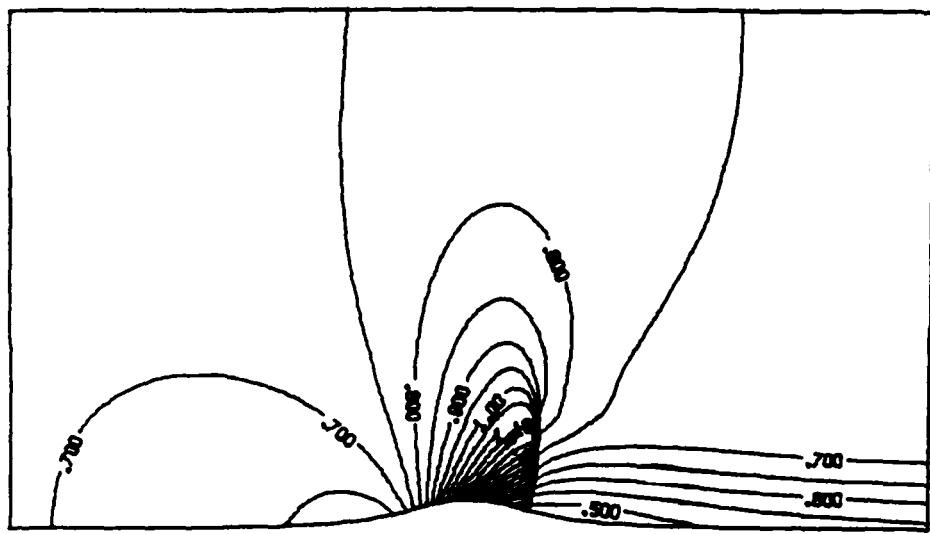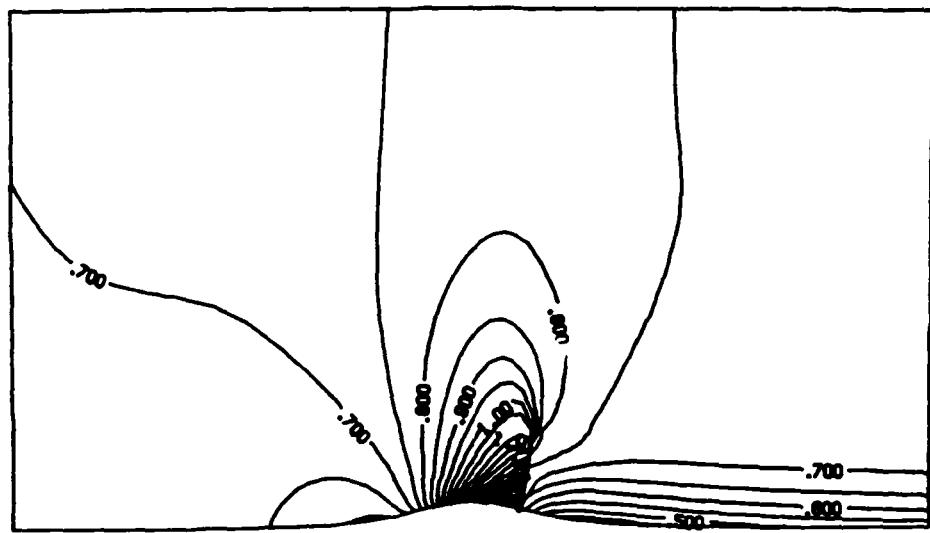
(a)   Scheme One

(b)   Scheme Two   (81x41 grid)

Fig. 9.40   Mach Contours $(\eta_0 = 1.0)$.
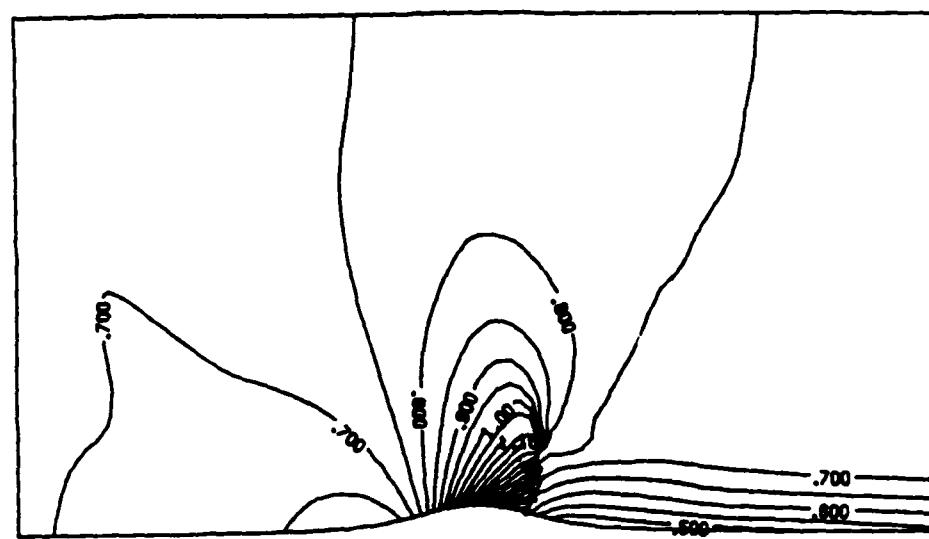
(c)   Scheme Two   (161x81 grid)
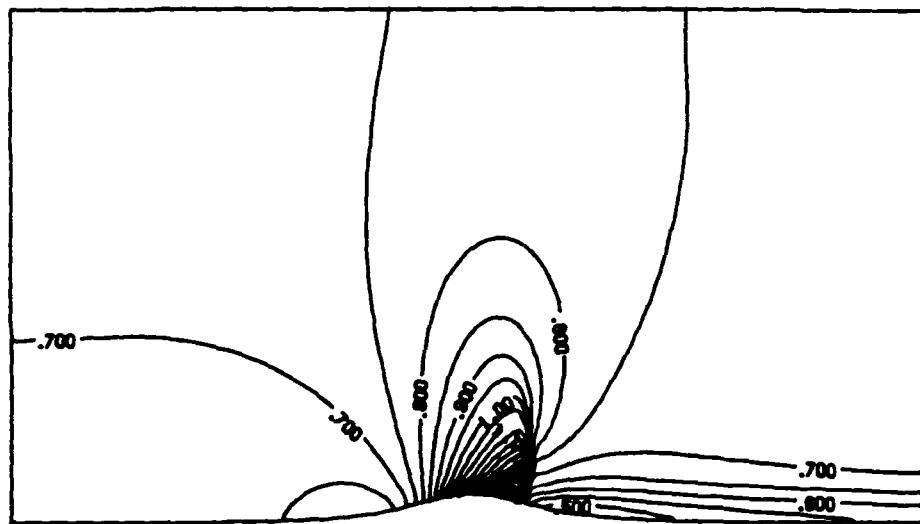
(d)   Scheme Three

Fig. 9.40 (continued).
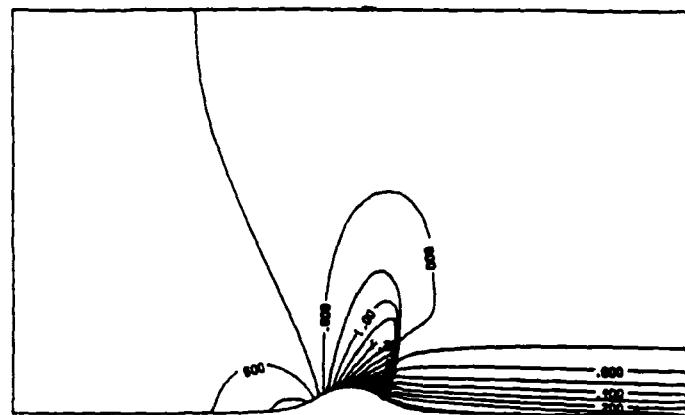
(a) Scheme One
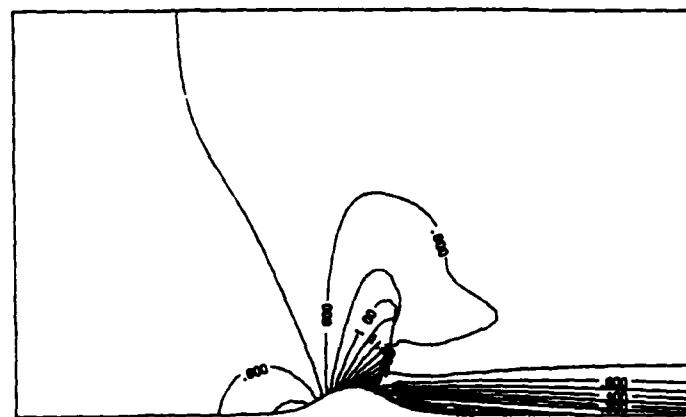
(b) Scheme Two
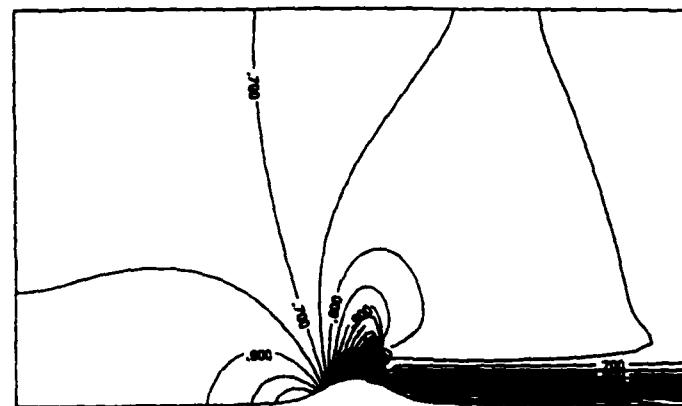
(c) Scheme Three

Fig. 9.41 Mach Contours (η_o = 0.4).

The next set of results which are shown in Figs. 9.42-9.43 compare the coarse grid shock fitting results to the flux vector splitting results for the case when η_0 is 0.2 which is the most severe case which was run. The Mach, entropy, and stream function plots for the shock fitting results are shown in Figs. 9.42a-9.42d respectively, and the same plots for the flux vector splitting results are shown in Figs. 9.43a-9.43d respectively. A comparison of the Mach contours show that the flux vector splitting results shows a smaller sonic region and that, in general, the contours are smoother. A comparison of the entropy contours shows that the shock fitting scheme is particularly good at preserving the correct entropy jump through the shock with zero entropy in the flow which has not been passed through the shock. The vorticity contours show that the shock fitting scheme results in some vorticity being present in the flowfield above the shock where it should not be and this is possibly due to lack of grid smoothness in this region. The vorticity plot Fig. 9.43d shows high gradients of vorticity near the lower boundary which may be due to some error in the way these values were computed although this has been checked and is felt not to be the case. The comparison of the Mach number along the lower boundary multiplied by the contraviant U in Figs. 9.42b and 9.43b shows again that the flux split results have a smaller jump in M through the shock than the shock fitting results.

9.2.2 Viscous Results

The Navier-Stokes code was run for 2000 iteration at a Reynolds number of 10,000 and the results are shown in Figs. 9.44 and 9.45. The flow was assumed to be laminar and calculated without the turbulence
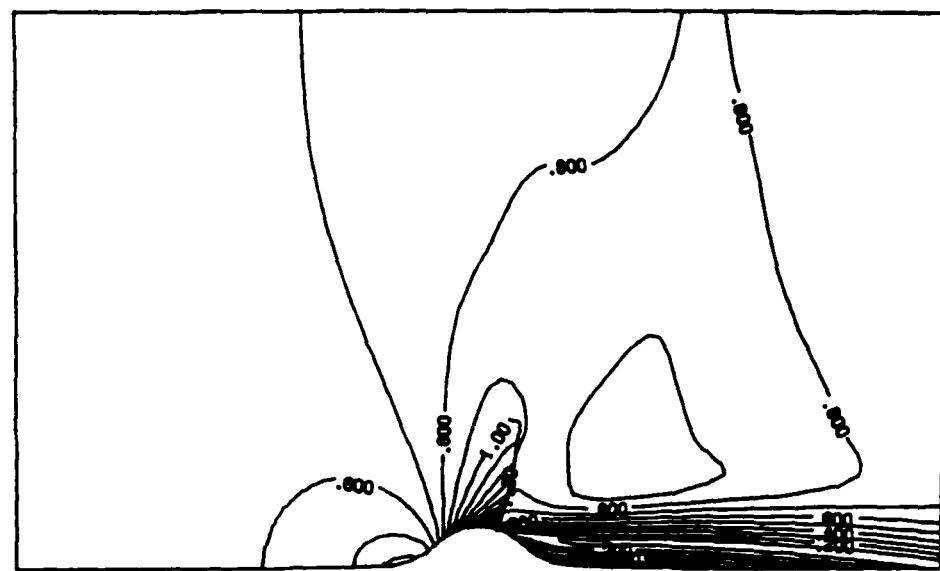
(a)   Mach Contours
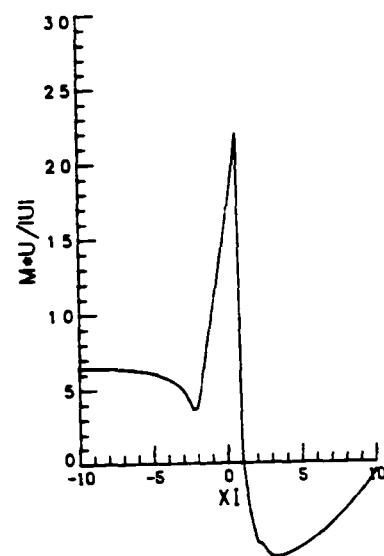
(b)   Lower Wall M vs ξ

Fig. 9.42   Results — Scheme 2   (81x41 grid, η_o = 0.2).
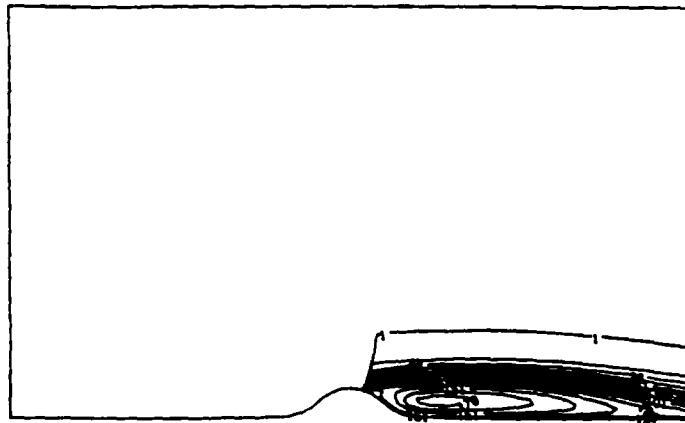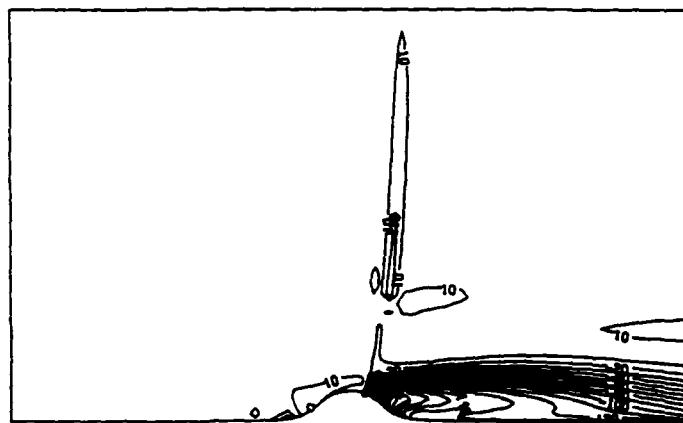
(c) Entropy Contours

(d) Vorticity Contours
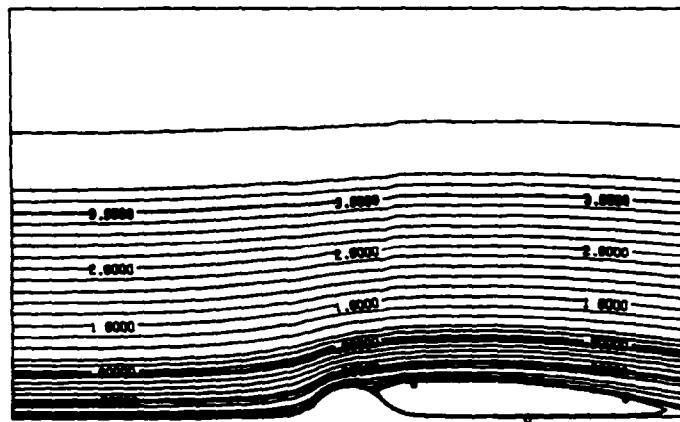
(e) Stream Function Contours

Fig. 9.42 (continued).
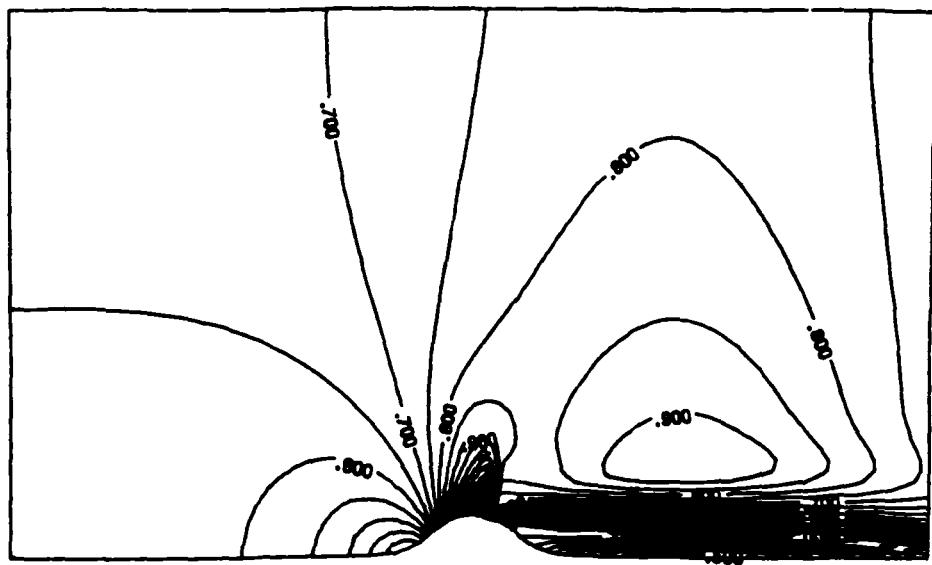
(a) Mach Contours
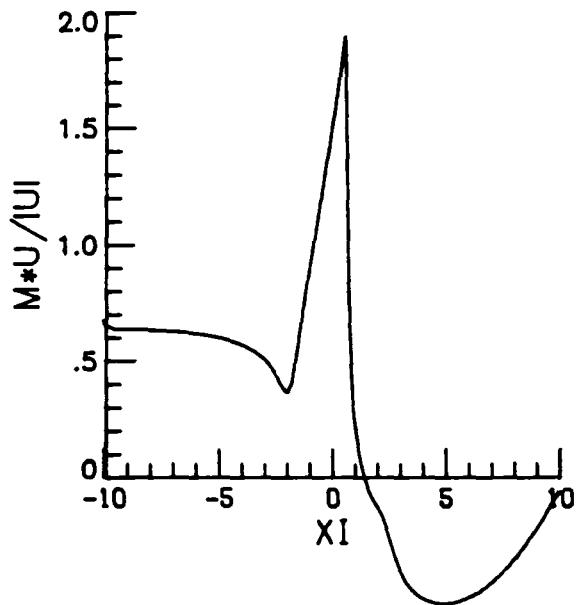
(b) Lower Wall M vs. ξ

Fig. 9.43 Results – Scheme 3 (81x41 grid, η_0 = 0.2).
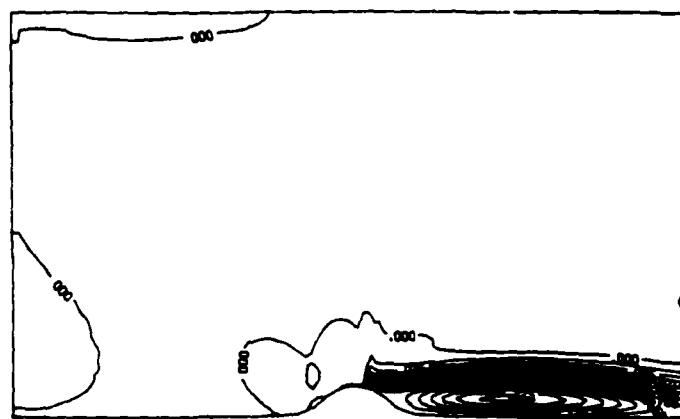
(c) Entropy Contours
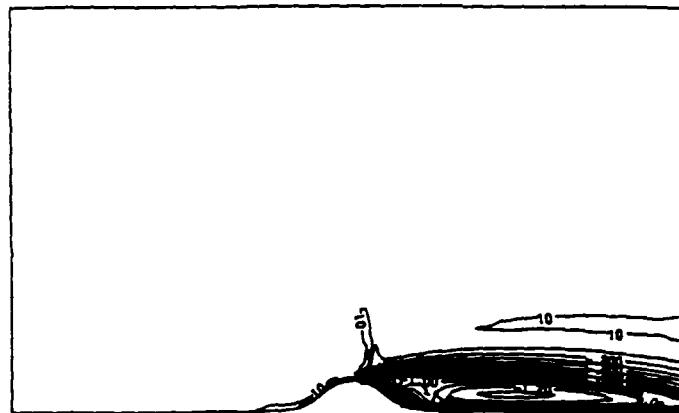
(d) Vorticity Contours
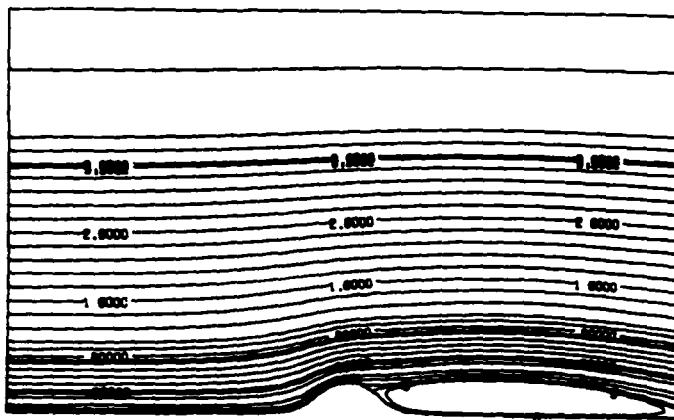
(e) Stream Function Contours

Fig. 9.43 (continued).

model. In Fig. 9.44a, the Mach and pressure contours after 1500 iterations are presented. The lower wall n_0 is equal to 1.0 and it can be seen that the flow has separated downstream of the step with at least one vortex present. The results at 2000 iterations in Fig. 9.45 also show the flow to be separated but the Mach and pressure contours are different from those at 1500 iterations indicating that the flow is unsteady. An examination of the convergence history reveals that after 1500 iterations, the computations do not converge any further, which is a further indication that the flow is unsteady. The viscous results are thus very different from the inviscid results and show that the inviscid separation phenomenon is not a good predictor as to when viscous separation will occur and that viscous calculations are needed.

9.3 Problem Three

The problem of flow past a circular arc (occasionally referred to as "Ni's bump") was solved using the shock capturing scheme 1 and the flux vector splitting scheme 3. An effort to do shock fitting was made using two different approaches but both yielded unsatisfactory results. The reasons for this are discussed in this section and a possible solution is described. The difficulties are the result of the fact that unlike the previous two configurations, this configuration has sharp stagnation corners where the flow velocity goes to zero. It is, therefore, desirable to cluster grid points near the corners in order to capture the high flow field gradients that exist in these regions. Since the shock fitting, which was attempted, moves the grid as the shock moves, special attention must be given to insure that the shock movement does not move the clustered grid away from these corners.
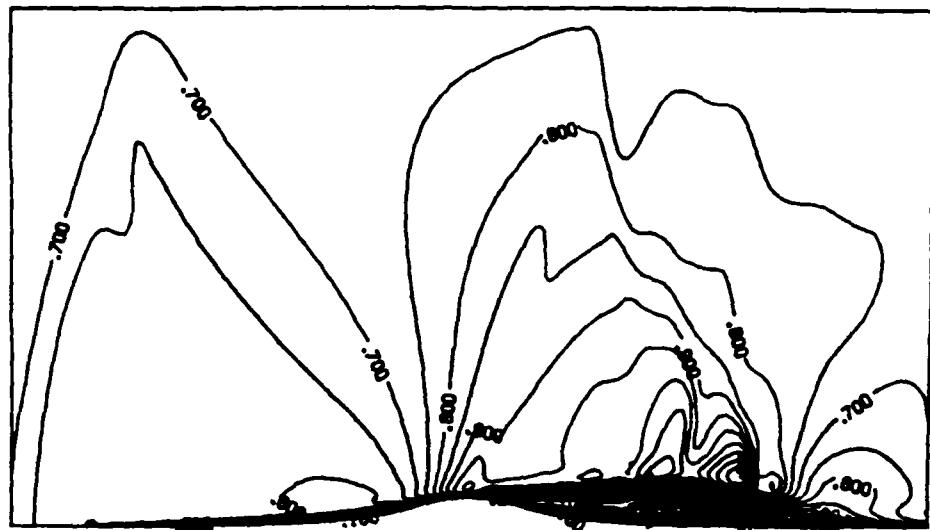
(a) Mach Contours
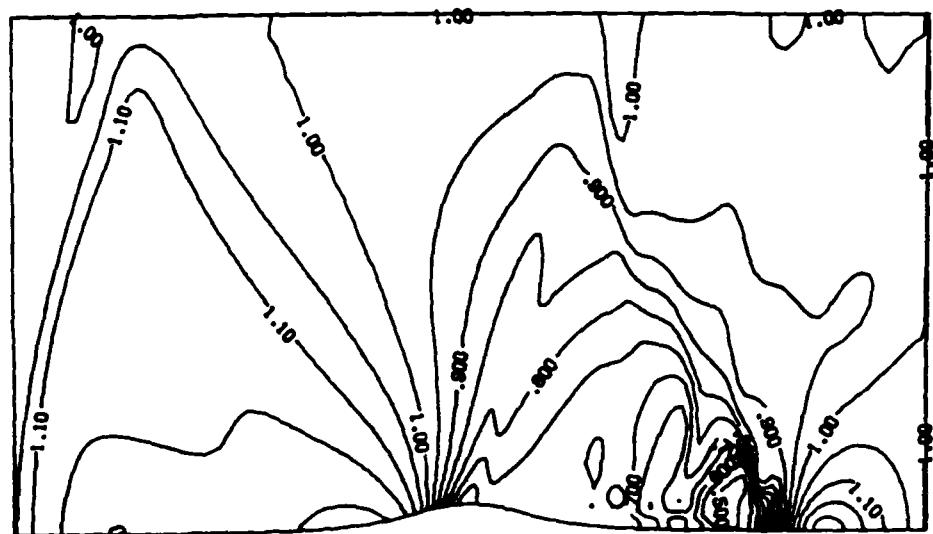
(b) Pressure Contours

Fig. 9.44 Results - Scheme 4 (1500 iterations).
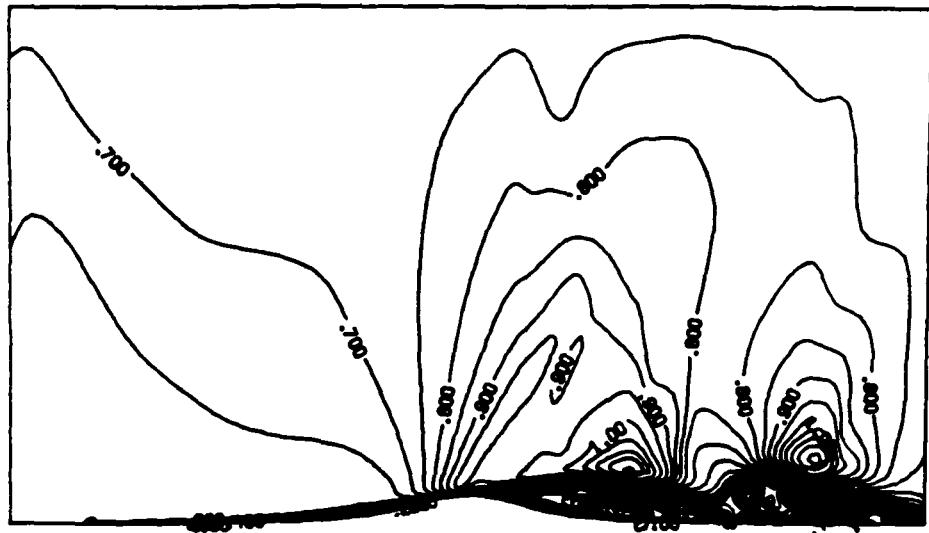
(a) Mach Contours
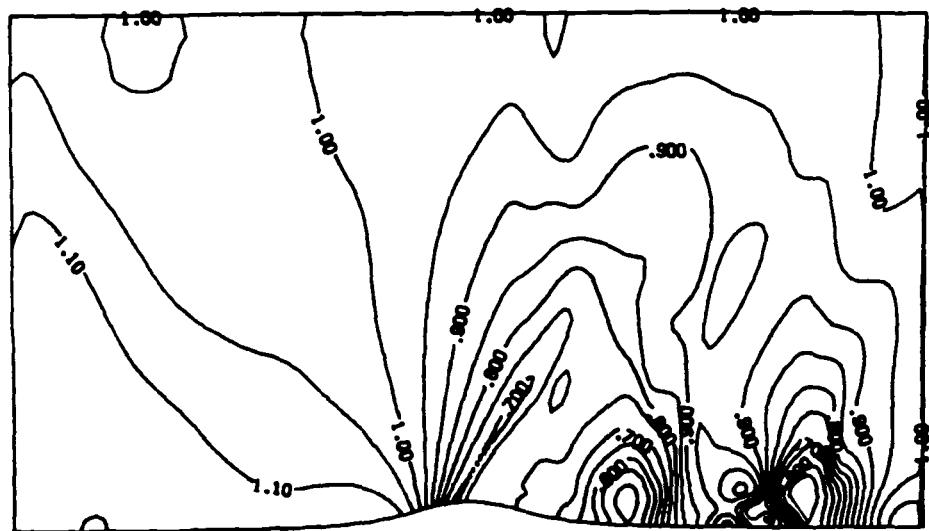
(b) Pressure Contours

Fig. 9.45 Results - Scheme 4 (2000 iterations).

Figures 9.46a shows the first grid which was used to solve the problem using scheme one. The grid was developed using bilinear interpolation and the elliptic smoothing described in Chap. 2. The grid achieves good clustering at the stagnation corners and over the bump through the third order polynomial distribution which was used. The nondimensional back pressure p/p_0 for this case was 0.74. The scheme was run for 1000 iterations and the resulting Mach contours are shown in Fig. 9.46b. It can be seen that the flow is transonic with a shock present over the bump. Unfortunately, there are some wiggles present in the flow field emanating from the corners which are apparently due to the grid clustering which leads to high gradients in the metric terms.

The writer was not able to do the shock fitting on this grid since it was generated using algebraic and elliptic methods instead of conformal mapping and scheme two relies on the existence of a conformal mapping to get the new transformation metrics x_ξ and x_η each time the grid was moved. In principal, it is possible to do this by interpolating the metrics from the original grid (since they are known) to the new shock fitted grid once the shock position is known and the writer tried this approach but it was not successful.

The writer then learned that a conformal transformation exists for this configuration, therefore, it ought to be possible to use the same shock fitting program on this case. The transformation was then used to develop the 81x41 grid shown in Fig. 9.47a, which can be seen clusters the grid points over the bump but not in the corners. Scheme one was then run for 2000 iterations on this case and the resulting Mach contours are shown in Fig. 9.47b. Although the back pressure is the same as in the previous run, the shock on top of the bump is much
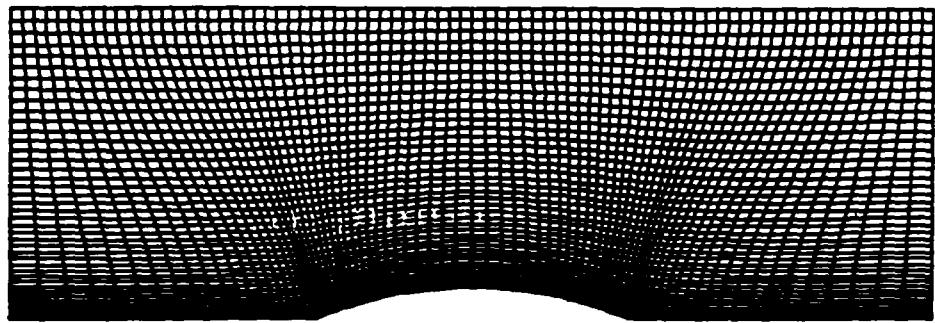
(a) 81x41 Grid
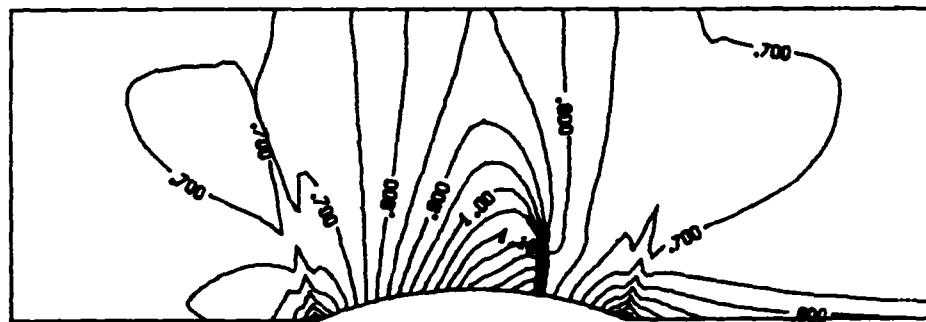
(b) Mach Contours

Fig. 9.46 Results - Problem 3 (algebraic grid).

weaker. A plot of the Mach number along the lower wall is shown in Fig. 9.47c and it can be seen that there is a fairly weak shock at approximately $\xi = 1.0$. It is also evident that true stagnation conditions are not achieved at the corners of the bump as they should be. It was throught that a higher grid resolution might alleviate these problems so the writer then ran the same case using a 161x41 grid. The resulting Mach contours are shown in Fig. 9.48a and the Mach number along the wall is shown in Fig. 9.48b. It is interesting to note that the solution near the lower boundary has high gradients in the Mach numbers and that the velocities near the lower boundary are lower than in the flowfield just off the wall. This is believed to be due to the fact that there is a discontinuity in the metric terms at the corners wich results from the way the grid has been generated.

In order to obtain a shock captured solution which might facilitate shock fitting better than the previous case, it was decided to move the upper boundary further away and to increase the back pressure to a nondimensional p/p_0 of 0.54. Scheme one was run on a 81x41 grid and the resulting Mach contours are shown in Fig. 9.49a and the vorticity contours in Fig. 9.49b. The Mach contours show a strong shock on the leeward side of the bump. The vorticity contours in Fig. 9.49b show high vorticity along the shock and also at the corner on the upstream side of the bump. The vorticity upstream of the shock is not physically correct and indicates again that the scheme does not do well in such regions. The shock fitting scheme two was tried on this case but with little success. The shock would become unstable after the code had run for less than 100 iterations and the code would encounter execution errors and stop.
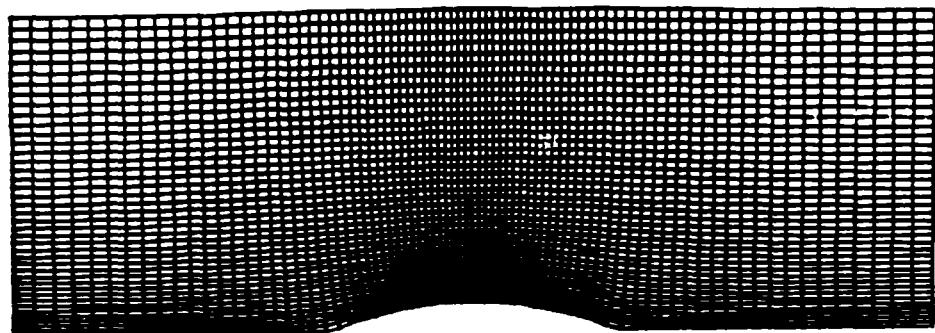
(a) 81x41 Grid
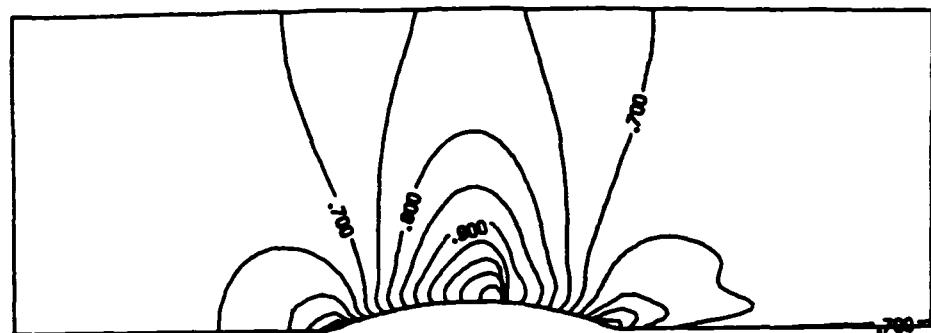
(b) Mach Contours
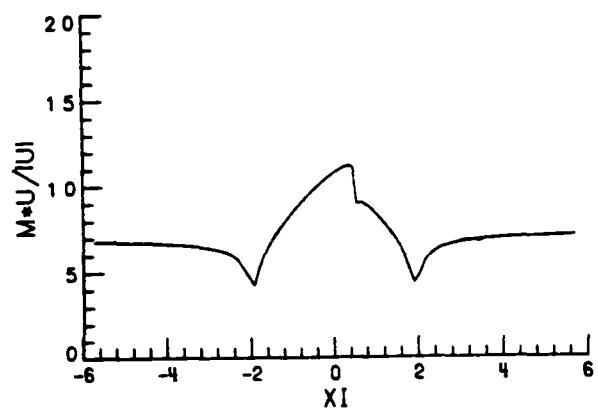
(c) Lower Wall M vs ξ

Fig. 9.47 Results – Problem 3   (81x41 conformal grid).
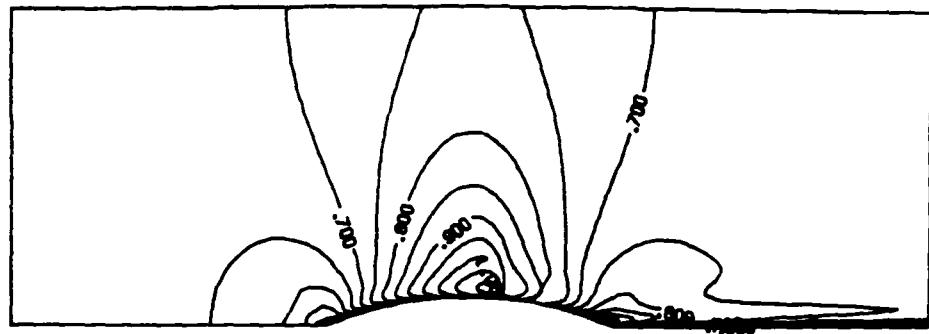
(a) Mach Contours
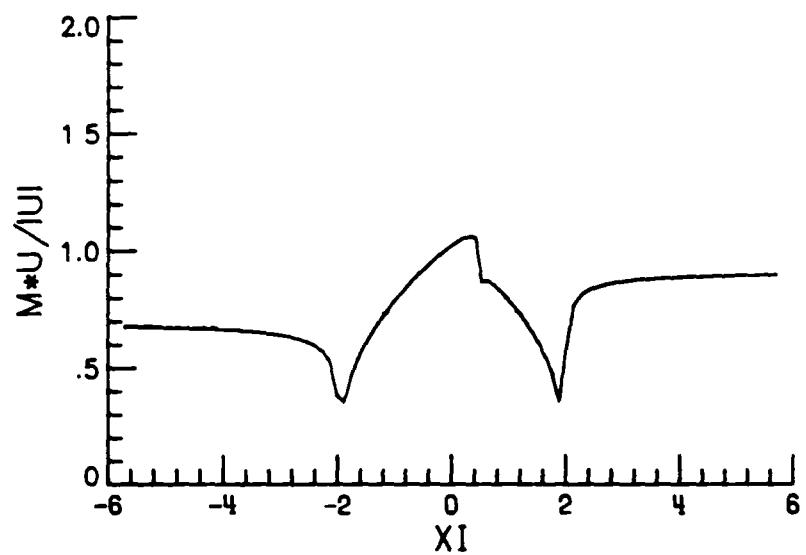
(b) Lower Wall M vs ξ_o

Fig. 9.48 Results - Problem 3 (161x81 conformal grid).
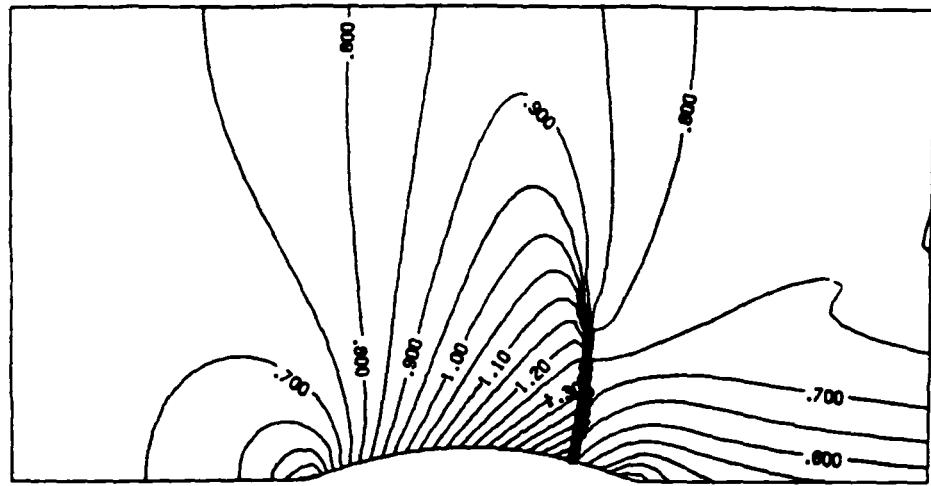
(a) Mach Contours
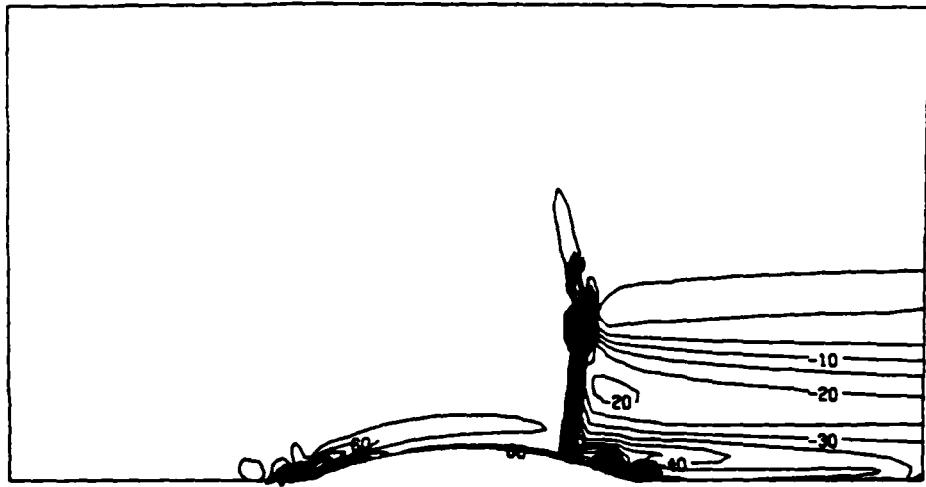
(b) Vorticity Contours

Fig. 9.49 Results – Problem 3 (81x41 conformal grid).

The grid was next refined to a 161x41 grid and the shock capturing scheme one tried again. The resulting Mach and entropy contours are shown in Figs. 9.50a and 9.50b respectively. It was found that refining the grid again resulted in a poor solution near the lower boundary due to the dicontinuity in the grid metrics at the corners. The entropy contours in Fig. 9.50b show that there is an entropy layer produced which starts at the front corner. This is an unphysical result and the poor quality of the solution made it not feasible to go on to the shock fitting.

The flux vector splitting scheme three was run on the 81x41 grid and the resulting Mach contours are shown in Fig. 9.51. The Mach contours appear smooth and there is no problem at the boundaries. The writer feels that this is a much better solution and although the shock is not resolved as well as it might be, the case using shock fitting; the solution was obtained without any special treatment which would have been necessary to get a shock fitted solution.

9.4 Problem Four

The grid for the NACA 0012 airfoil was produced by the elliptic procedure described in Chap. 2. The grid covered only the top half of the airfoil and used 91x33 points in the ξ and η coordinated directions. The outer boundary was placed ten chords away from the airfoil surface and the downstream boundary was ten chords lengths away. There are 73 points along the top surface of the airfoil. The grid is shown in Fig. 9.52 in three perspectives ranging from far away to close to the leading edge. It can be seen that the resolution near the leading and trailing edges is reasonably dense and that the orthogonality of the grid at the airfoil surface is good.
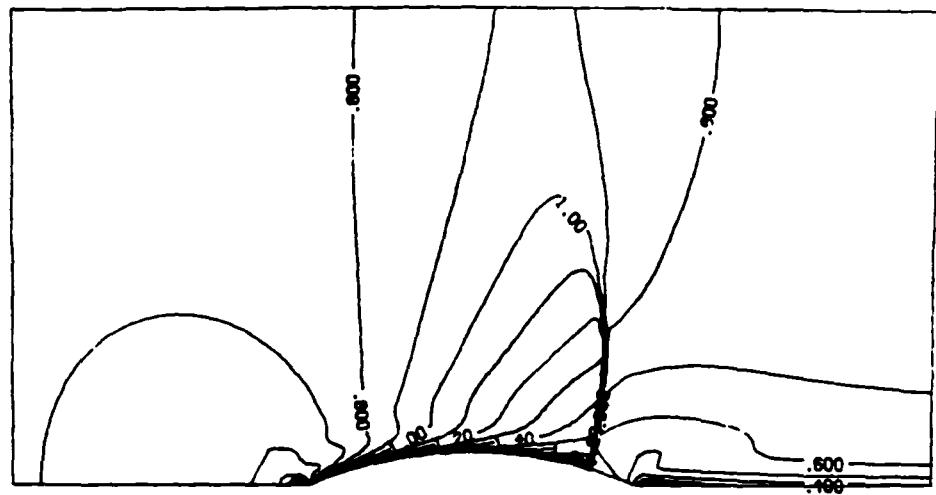
(a) Mach Contours
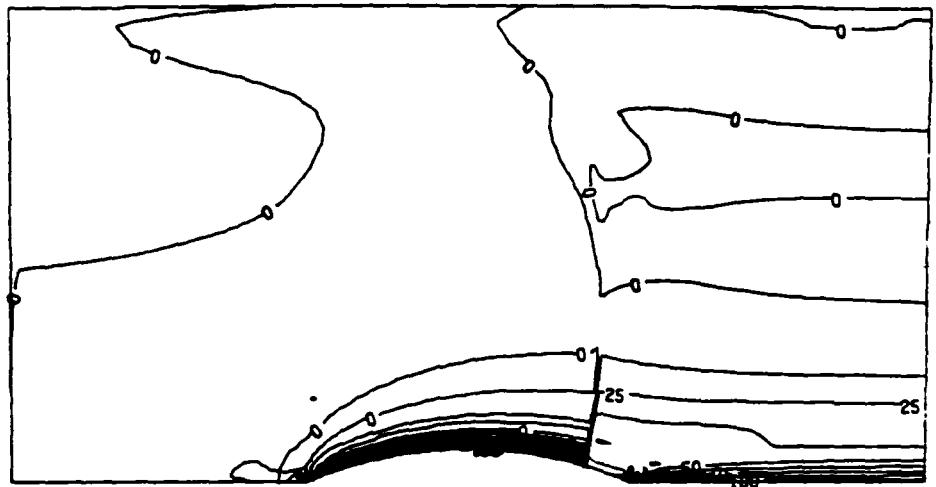
(b) Entropy Contours

Fig. 9.50 Results – Problem 3 (161x81 conformal grid).
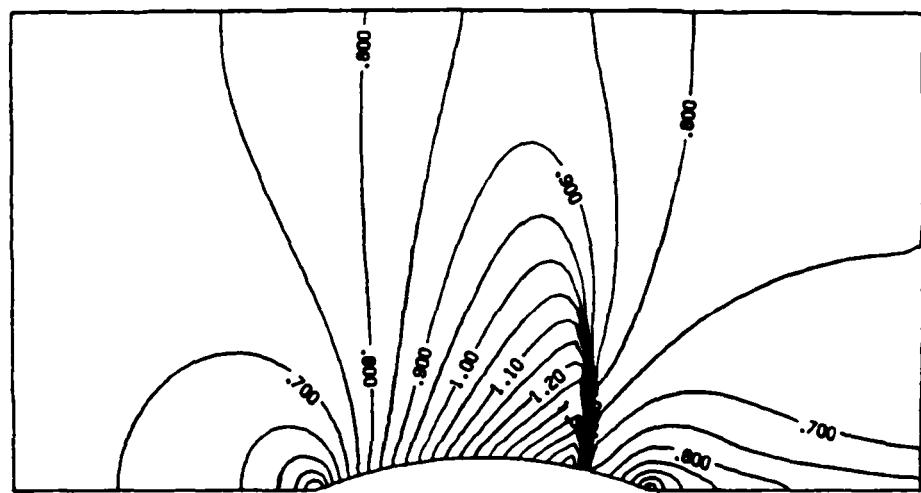
Fig. 9.51 Results - Problem 3 - Scheme 3.
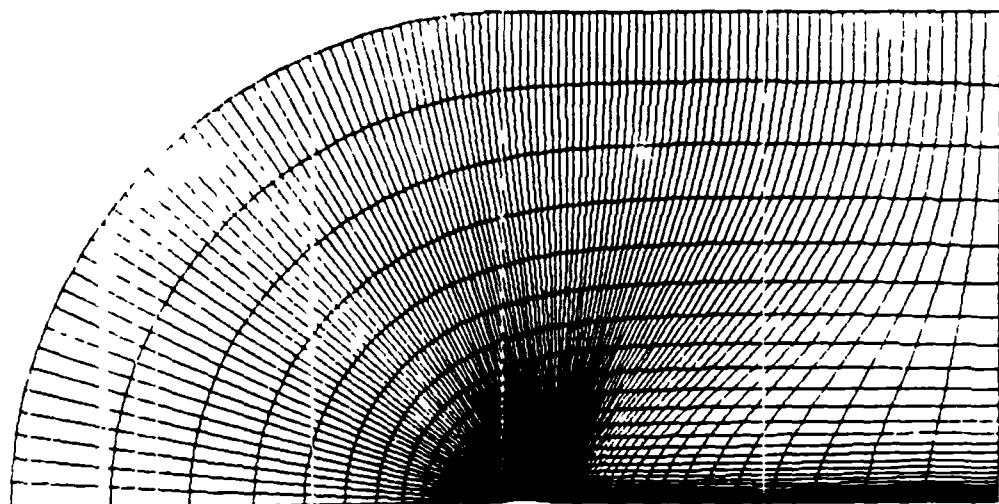
(a) 91x31 C-Grid
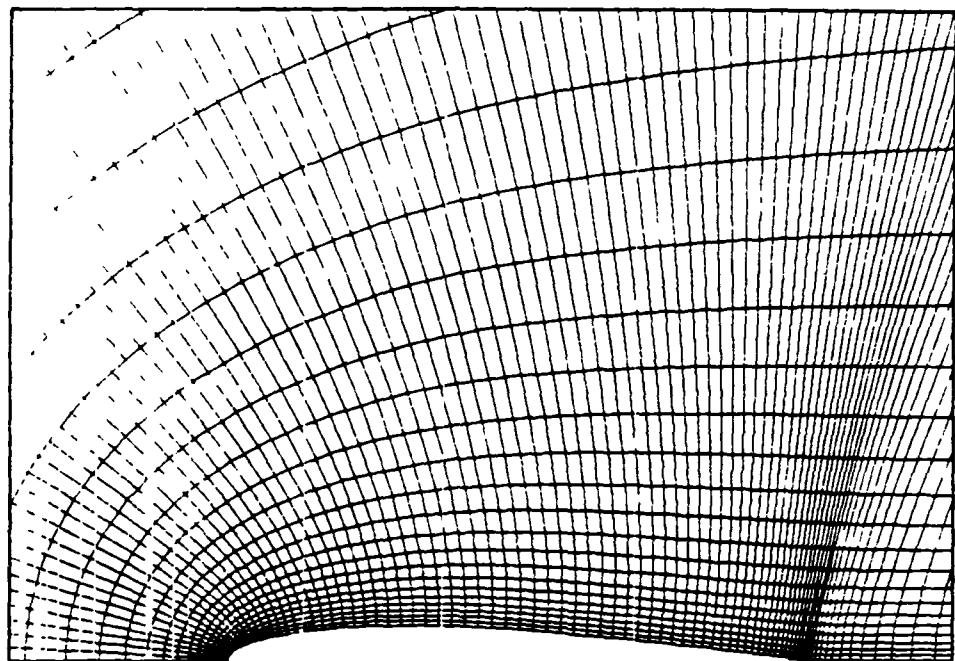
(b) Detail over airfoil

Fig. 9.52 Grid for NACA 0012 Airfoil.

Scheme one was specially modified to run this particular case and the freestream Mach number used was 0.8, as this is a good transonic test case. The scheme was allowed to run for 3000 iterations which resulted a drop in the residual of about 2.5 order of magnitude. The Mach contours are shwon in Fig. 9.53. Although the solution may appear to be reasonable, there are again kinks in the contours near the trailing edge which may be due to lack of grid smoothness. Also, the shock location and strength are not correct. Steger has computed this case and gives the shock location in terms of x/L where L is the chord as being 0.6 and the Mach number just before the shock as 1. The results which were computed using scheme one show the shock at 0.73 of the chord and the Mach number as 1.405. The solution is, therefore, not correct and either shock fitting or the flux vector splitting code is necessary for better results.

The writer modified scheme two to do this case, but it was not stable and the grid developed extreme skewness as a result use of a fifth order polynomial function to distribute the grid points with the shock moving. The writer feels that a shock fitting scheme which has the grid stationary and simply extrapolates to the shock from the flow field would work much better than the existing shock fitting scheme which attempts to adapt the grid to the moving shock. Such a scheme is being developed by the writer but at the time of this writing, it has not yet been completed or tested.
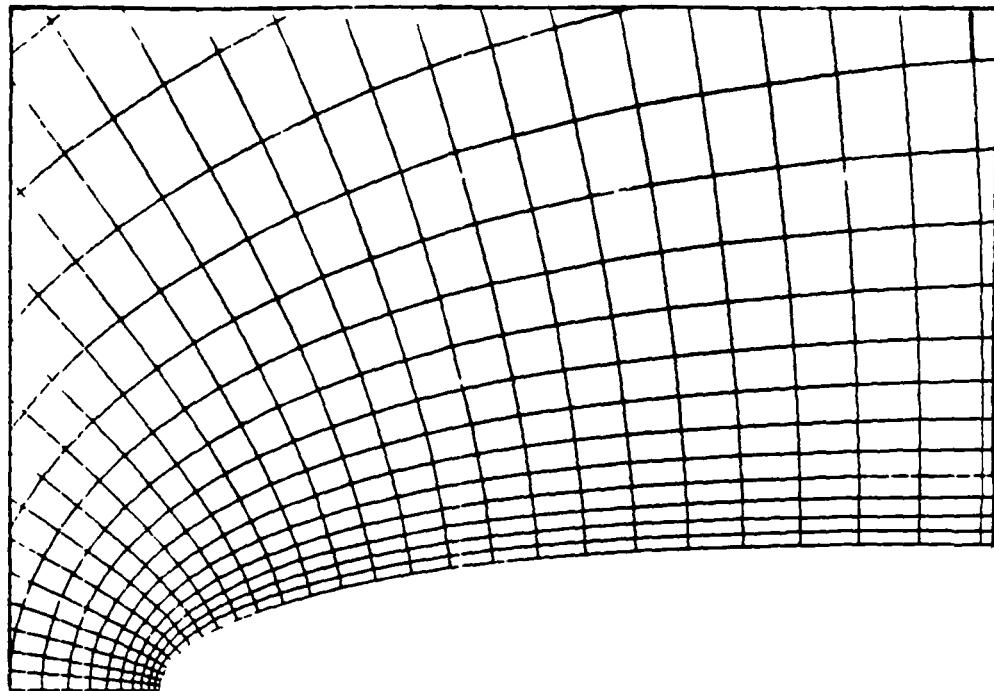
(c) Leading edge detail
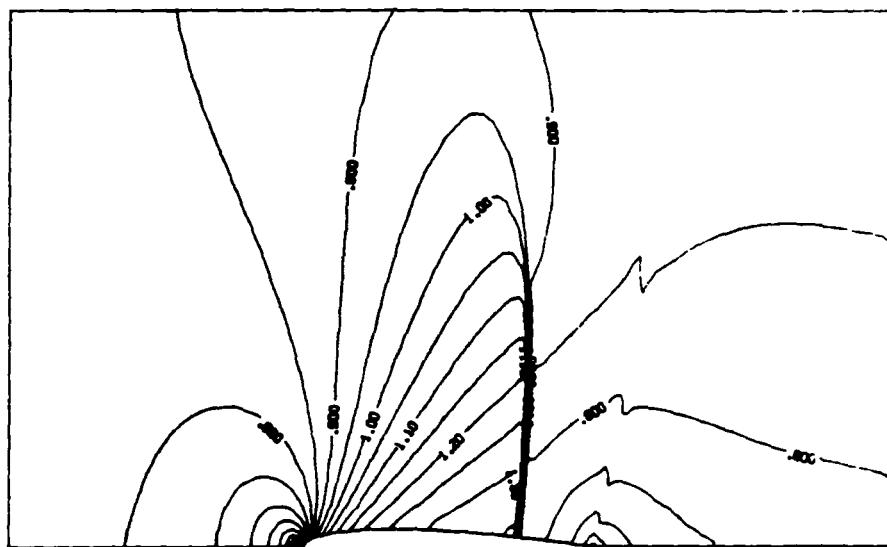
Fig. 9.53 Problem 4 - Mach Contours.

Chapter 10

CONCLUSIONS

This study was originally initiated as an investigation into the
inviscid separation phenomenon. Since that time, there have been
several studies on this topic published and, as yet, reseachers do not
seem to agree on the significance of these inviscid results. The
questions concerning inviscid separation appear to belong to three
separate but related categories which can be stated as:

1. When are numerically computed solutions which exhibit flow
    separation valid solutions to the governing equations and are they
    unique?

2. In the case of computed solutions where closed recirculation regions
    are present, what is the source of the vorticity inside the eddies?

3. What is the physical relevance of an inviscid separated flow to the
    viscous case?

The first question has been investigated by various researchers
either by grid refinement procedures or by careful control of parameters
such as the amount of artificial dissipation which is added to a scheme
to provide stability [15, 17, 18, 20, 22]. In general, it appears that
while in some cases the computed inviscid solutions are valid and
reasonable, it is also possible to produce inviscid separation if
excessive artificial dissipation is present or if very coarse grids are

used. The question of uniqueness has not been adequately examined, although it is known that in some cases nonunique solutions to the Euler equations do occur. Since numerical solutions are by nature approximate solutions and there exists few rigorous proofs that the solutions obtained by any given numerical method are in fact the correct approximations to the problem (including boundary conditions) being solved, it is possible that this issue will never be completely resolved.

There does not, as yet, appear to be any clear answer to the second question. The most common explanation for the presence of vorticity is that flow through curved shock waves results in entropy gradients and thus by Crocco's theorem, vorticity. Also, since in nearly all cases reported, the inviscid separated zone are "captured" during the iterations procedure by the numerical algorithm and the initial assumed flow field is free of such separated zones, it can be argued that the unsteady transient flow leads to entropy and vorticity in the part of the flow field that is eventually "pinched-off" and trapped inside the eddy. It should also be noted that while in theory, there exists a dividing stream line between the trapped eddy and the outside flow field and once formed, vorticity and entropy cannot enter the eddy, in actual numerical computations the flow inside the eddy is coupled to the flow outside the artificial viscosity and the boundary between the two zones (which is smeared) may allow the total amount of entropy and vorticity inside the change.

The third question may be the most important of all, since usually the purpose of doing an inviscid computation is to provide some insight as to how an actual viscous flow would behave without the expense of

actually doing viscous calculations. Since real fluids contain viscosity, the first two questions, while of theoretical interest, do not pertain to the numerical simulation of viscous flows.

This investigation had many different aspects to it, but the primary effort involved an attempt to solve the transonic flow past various two-dimensional configurations using various numerical procedures. The four configurations which were chosen included a rearward facing step, a "bump" in a channel, a circular arc airfoil, and a NACA 0012 airfoil. For the first two configurations, the position of the lower boundary was varied to study the effect of flow separation a the curvature in the expansion region increased. The last two configurations were used to determine how the numerical schemes could handle somewhat more complicated geometries.

The grids for these configurations were produced using either conformal mapping or algebraic and elliptic procedures. The conformal mapping procedure has the advantage that it is fast and straightforward and produces grid which are perfectly orthogonal as well as satisfy the Cauchy-Riemann equations. Also when doing shock fitting, it is necessary to recompute the metric terms each time the grid is moved and this is done very easily if there exists a simple transformation which can be used. The disadvantage is that a different mapping must be found for each configuration which greatly restricts the geometrical versatility of the method. Finally, the method cannot be extended to three-dimensional regions in the general case. The algebraic and elliptic methods were used for the last two problems and worked well.

The numerical schemes which were used included three Euler solvers and a Navier-Stokes solver. The three Euler solvers included an explicit Lambda scheme, a shock fitting version of this scheme and a flux-vector splitting scheme. The first two schemes were coded by the writer and the shock fitting version included some features developed by the writer to enable the code to do imbedded shock fitting for the regions which were considered. These included the use of polynomial functions to smoothly blend the end of the shock to the grid line which extended from the end of the shock to the upper boundary and the use of least squares fitting to smooth the shock acceleration, velocity and position as it was being computed in order to overcome stability problems which were encountered. Even so, the method was not successful in all cases. The first two schemes were also vectorized for the NASA Langley VPS 32 supercomputer which greatly increases their execution speed. The flux vector splitting scheme proved to be the most robust and was easy to use. Generally, the convergence rate was also higher with this code than with the explicit schemes although since it was not vectorized, the overall execution time to get a converged solution was of the same order of magnitude as the explicit schemes. The Navier-Stokes code was also robust and was vectorized for the VPS 32.

The three inviscid schemes were run on configurations one and two under a variety of conditions which were intended to examine the effects of changing the position of the lower boundary (on configuration one the upper boundary was also tested in three positions). The Navier-Stokes was run under more limited sets of conditions since the writer felt that the runs which were conducted were sufficient for comparison purposes.

Schemes one and three were run on configuration four and an attempt was made to do the shock fitting on this configuration but this was unsuccessful. A new way to do the shock fitting, which does not move the grid with the shock, is currently being developed but is not available for use as of this writing. This method was not felt to be necessary when this study was initiated and therefore was not included in the proposal for this research. Scheme one was run on the NACA 0012 configuration four, but the position and strength of the computed shock were not correct. Shock fitting has also been tried on this case but again was not successful. However, the flux vector splitting scheme has been run on this case extensively by von Lavante and the results as reported by this scheme agree well with other reported results.

The major conclusions, which the writer believes can be made from this investigation, are summarized below.

1. Conformal grid generation worked well for the simple two-dimensional configurations which were generated as test cases. It is fast and produced perfectly orthogonal grids.

2. For configurations three and four, algebraic and elliptic grid generation was used successfully. This method has the advantage that a grid can be produced for virtually any configuration. The algebraic method is fairly fast but must be tuned to get good results. The elliptic method will produce good orthogonality at the boundaries provided the source terms are carefully controlled. The elliptic method requires the solution of a coupled set of PDE's and, therefore, results much more computer time than either the algebraic or conformal methods.

3. The shock capturing Lambda scheme is an accurate scheme which was easy to code and is based on characteristic theory. The scheme gave results which were in good qualitative agreement with the other inviscid schemes used. Unfortunately, since the equations are solved in nonconservative form, the results at shocks were generally not correct. Also, the scheme converged very slowly due to the explicit CFL limitation.

4. The shock fitting scheme developed by the writer overcame the disadvantage of the previous scheme by explicitly solving the Rankine-Hugoniot jump relations through the shock. An adaptive grid which moved with the shock was used to obtain a high resolution of the correct shock shape and position. Vectorization of the scheme was fairly straightforward and made the computations fairly efficient despite the restrictive CFL limitation. The major disadvantage is that the scheme (at least as it was used by the writer) requires a conformal transformation to exist to enable a rapid evaluation of the metric terms which must be updated each time the grid is moved. For general configurations where no such transformation exists, shock fitting is still possible but would be more difficult to implement.

5. The flux vector splitting scheme was a robust code and achieved the correct jump relations through the captured shocks without the use of fitting. The scheme converged faster than the explicit codes since the code is implicit which allows a much higher CFL number to be used.

6. Two configurations, a rearward facing step and a bump inside a channel, were studied for flow separation. The inviscid cases were run using various positions of the lower boundary to compare when separation occurred. It was found that when the lower boundaries were such that the channel transition were very gradual, no separation occurred. However, as η_0 was brought closer to zero, flow separation would eventually occur and it appeared to be related to entropy gradients in the flow field downstream of the shock which produced vorticity in the flow.

7. Grid refinement was done using the vectorized shock-fitting scheme and the results did not indicate that the flow was less likely to separate than on the coarse 81x41 grid.

8. As η_0 is reduced to zero in the rearward facing step, it appears form the results using the flux-vector splitting scheme that the shock at the corner in the inviscid cases eventually is reduced to a negligible size and the flow simply separates smoothly from the corner with a single recirculation eddy. This is in agreement with previous results obtained by Jameson [61]. This was not, however, observed with the shock fitting code as it was not possible to get results with lower than 0.4 since the resolution of the shock-fitting grid was not adequate at the corner.

9. The viscous results which were obtained were significantly different from the inviscid results in that flow separation occurred due to the effect of the adverse pressure gradients on the boundary layer and the flow was steady. In the inviscid cases, separation appears to be due to vorticity at the wall produced by

flow through the shock (which was not present in the viscous cases). The viscous results generally showed an unsteady shedding of vorticities from the leeside of the corner or the bump with multiple recirculation zones; whereas, the inviscid results showed no separation for the same position of the lower boundary. When the lower boundary n_0 was reduced, a single recirculation zone formed in the inviscid cases which was steady and was not shed.

10. Two additional configurations were investigated with the shock capturing schemes and an attempt was made to do shock fitting. The first was a simple circular arc airfoil and the second was a NACA 0012 airfoil. The shock fitting scheme was attempted on the circular air airfoil but the conformal grid which was generated had a discontinuity in the metric terms at the corner of the arc with the lower boundaries which resulted in the production of an entropy layer emanating from the front stagnation corner which made the shock fitting Lambda scheme unstable. The flux vector splitting scheme was run successfully on this configuration.

11. The NACA 0012 case was run with the shock capturing scheme one but the shock position and strength were nor correct and shock fitting was tried but so far has not been successful. This is due in part to the need to adjust the grid by a fifth order polynomial to keep adequate resolution at the leading and trailing edges. A different type of shock fitting which holds the grid stationary while the shock is moved may be necessary to avoid this problem.

REFERENCES

1. Courant, R. and Friedrichs, K. O., <u>Supersonic Flow and Shock Waves</u>, Springer-Verlag, New York, 1976.

2. Lax, P. D., <u>Hyperbolic Systems of Conservation Laws and the Mathematical Theory of Shock Waves</u>, Soc. for Industrial and Applied Mathematics, 1973.

3. Richtmeyer, R. D. and Morton, K. W., <u>Difference Methods for Initial Value Problems</u>, Interscience, New York, 1967.

4. Smoller, J., <u>Shock Waves and Reaction-Diffusion Equations</u>, Springer-Verlag, New York, 1982.

5. Majda, A., <u>Compressible Fluid Flow and System of Conservation Laws in Several Space Dimensions</u>, Springer-Verlag, New York, 1984.

6. Anderson, D. A., Tannehill, J. C., and Pletcher, R. H., <u>Computational Fluid Mechanics and Heat Transfer</u>, McGraw Hill, New York, 1984.

7. Roe, P. L., "Characteristic Based Schemes for the Euler Equations," <u>Annual Review of Fluid Mechanics</u>, Annual Reviews, Inc., Palo Alto, California, 1986.

8. Lax, P. D. and Wendroff, B., "Systems of Conservation Laws," <u>Communications on Pure and Applied Mathematics</u>, Vol. 13, 1960, pp. 217-237.

9. MacCormack, R. W., "The Effect of Viscosity in Hypervelocity Impact Cratering," AIAA Paper 69-354, January 1969.

10. Courant, R., Isaacson, E. and Rees, M., "On the Solution of Non-Linear Hyperbolic Differential Equations by Finite Differences," <u>Communication on Pure Applied Mathematics</u>, Vol. 5, 1952, pp. 243-249.

11. Godunov, S. K., "A Finite Difference Method for the Numerical Computational of Discontinuous Solutions of the Equations of Fluid Dynamics," <u>Materialovy Sbornik</u>, Vol. 47, 1959, pp. 271-306.

12. Pulliam, T. J., "Artificial Dissipation Models for the Euler Equations," AIAA Paper 85-0438, January 1985.

13. Jameson, A., Schmidt, W. and Turkel, E., "Numerical Solutions of the Eule Equations by Finite-Volume Methods Using Runge-Kutta Time-Stepping," AIAA Paper 81-1259.

14. Beam, R. M. and Warming, R. F., "An Implicit Finite-Difference Algorithm for Hyperbolic Systems in Conservation Law Form," Journal of Computational Physics, Vol. 22, September 1976, pp. 87-110.

15. Salas, M. D., "Recent Developments in Transonic Euler Flow Over a Circular Cylinder," Mathematics and Computers in Simulation, Vol. XXV, 1983, pp. 232-236.

16. Fraenkel, L. E., "On Corner Eddies in Plane Inviscid Shear Flow," Journal of Fluid Mechanics, Vol. 11, November 1961, pp. 400-406.

17. Kumar, A. and Salas, M. D., "Euler and Navier-Stokes Solutions for Supersonic Shear Flow Past a Circular Cylinder," AIAA Journal, Vol. 23, No. 4, April 1985, pp. 583-587.

18. Barton, J. T. and Pulliam, T. H., "Airfoil Computations at High Angles of Attack, Inviscid and Viscous Phenomenon," AIAA Paper 84-0524, January 1984.

19. Marconi, F., "Supersonic Conical Separation Due to Shock Vorticity," AIAA Journal, Vol. 22, No. 8, August 1984, pp. 1048-1055.

20. Newsome, R. W. and Thomas, J. L., "Computations of Leading Edge Vortex Flows," private communications.

21. Chakravarthy, S. R., "Numerical Issues in Computing Inviscid Supersonic Flow Over Conical Delta Wings," AIAA Paper 86-0440, January 1986.

22. Kandil, O. A. and Chuang, A. "Influence of Numerical Dissipation in Computing Supersonic Vortex-Dominated Flows," AIAA Paper 86-1073, May 1986.

23. Honji, H., "The Starting Flow Down a Step," Journal of Fluid Mechanics, Vol. 69, May 1975, pp. 229-240.

24. Westphal, R. V., Johnston, J. P., and Eaton, J. K., "Experimental Study of Flow Reattachment in a Single-Sided Sudden Expansion," NASA CR 3765, January 1984.

25. Morgan, K., Periaux, J., and Thomasset, F., "Analysis of Laminar Flow Over a Backward Facing Step," Vieweg, Braunschweig, pp. 420, 1984.

26. Schmidt, W. and Jameson, A., "Euler Solutions as Limit of Infinite Reynolds Number for Separation Flows and Flows with Vorticies," Lecture Notes in Physics, Vol. 170, Springer-Verlag, New York, 1982.

27. Gabutti, B., "On Two Upwind Finite-Difference Schemes for Hyperbolic Equations in Non-Conservation Form," _Computers and Fluids_, Vol. 11, No. 3, 1983, pp. 207-230.

28. Moretti, G., "The λ-Scheme," _Computers and Fluids_, Vol. 7, No. 3, September 1979, pp. 191-205.

29. Rumsey, C., "Time-Dependent Navier-Stokes Computations of Separated Flows Over Airfoils," AIAA Paper 85-1684, January 1985.

30. Churchill, R. V., Brown, J. W., and Verhey, R. F., _Complex Variables and Applications_, 3rd Edition, McGraw Hill, New York, 1976.

31. Karamcheti, K., _Principles of Ideal-Fluid Aerodynamics_, Krieger, Malabar, Florida, 1980.

32. Gordon, W. J. and Thiel, L. C., "Transfinite Mappings and Their Applications to Grid Generation," _Numerical Good Generation_, ed. by Thompson, J. F., North Holland.

33. Smith, R. E. and Wiese, R. E., "Interactive Algebraic Grid-Generation Technique," NASA Technical Paper 2533, March 1983.

34. North Atlantic Treaty Organization, Advisory Group for Aerospace Research and Development, AGARD-AR-211, "Test Cases for Inviscid Flow Field Methods," May 1985.

35. Thomas, P. D. and Middlecoff, J. F., "Direct Control of Grid Point Distribution in Meshes Generated by Elliptic Equations," AIAA Journal, Vol. 18, No. 6, June 1980, pp. 652-711.

36. Batchelor, G. K. _An Inroduction of Fluid Dynamics_, Cambridge-Verlage, New York, 1982.

37. John, F., _Partial Differential Equations_, 4th Ed., Springer-Verlag, New York, 1982.

38. Roach, P. J., _Computational Fluid Dynamics_, Hermosa, Albuquerque, New Mexico, 1982.

39. Smith, G. D., _Numerical Solution of Partial Differential Equations: Finite Difference Methods_, Oxford, 1978.

40. Moretti, G., "An Efficient Euler Solver, With Many Applications," AIAA Paper 87-0352, January 1987.

41. McBryan, Oliver A., "Computational Methods for Discontinuities in Fluids," _Lectures in Applied Mathematics_, Vol. 22, American Mathematical Society, 1985.

42. Conte, S. D. and DeBoor, Carl, _Elementary Numerical Analysis, an Algorithmic Approach_, 3rd Ed., McGraw-Hill, New York, 1980.

43. Dadone, A. and Napolitano, M., "An Implicit Lambda Scheme," <u>AIAA Journal</u>, Vol. 21, October 1983, pp 1391-1399.

44. Dadone, A. and Magi, U., "A Quasi-Conservative Lambda Formulation," AIAA Paper 85-0088, January 1985.

45. von Lavante, E., Claes, D., and Anderson, W. K., "The Effects of Various Implicit Operators on a Flux Vector Splitting Method," AIAA Paper 86-0273, January 1986.

46. von Lavante, E. and Trevino, J., "Numerical Predictions of Internal Flows Using a Diagonalized Vector Splitting Algorithm," AIAA Paper 84-1246, June 1984.

47. von Lavante, E. and Haertl, A., "Numerical Solutions of Euler Equations Using Simplified Flux Vector Splitting," AIAA Paper 85-1333, July 1985.

48. Van Leer, B., "Flux-Vector Splitting for the Euler Equations," ICASE Report No. 82-30, September 1982; also: <u>Lecture Notes in Physics</u>, Vol. 170, 1982, pp. 507-512.

49. Van Leer, B., "Towards the Ultimate Conservative Difference Scheme, V. A Second-Order Sequel to Godunou's Method," <u>Journal of Computational Physics</u>, Vol. 32, July 1979, pp. 101-136.

50. Rumsey, C. L., Thomas, J. L., Warren, G. P. and Liu, G. C., "Upwind Navier-Stokes Solutions for Separated Periodic Flows," AIAA Paper 86-0247, January 1986.

51. Steger, J. L., "Implicit Finite Difference Simulation of Flow About Arbitrary Two Dimensional Geometries," <u>AIAA Journal</u>, Vol. 16, No. 7, July 1978, pp. 679-686.

52. Baldwin, B. S. and Lomax, H., "Thin Layer Approximation and Algebraic Model for Separated Turbulent Flows," AIAA Paper 78-257, January 1978.

53. Cebeci, T., "Calculation of Compressible Turbulent Boundary Layers with Heat and Mass Transfer," <u>AIAA Journal</u>, Vol. 9, No. 6, June 1971, pp. 1091-1097.

54. Kreiss, H.-O., "Difference Approximations for the Initial-Boundary Value Problem for Hyperbolic Differential Equations," Numerical Solutions of Nonlinear Differential Equations, D. Greenspan, Ed., Wiley, New York, 1966, pp. 41-166.

55. Tong, S. S., "Time-Split Inflow Boundary Condition," ASME Paper 85-GT-165, March 1985.

56. Rudy, D.H. and Strikwerda, J. C., "A Nonreflecting Outflow Boundary Condition for Subsonic Navier-Stokes Calculations," <u>Journal of Computational Physics</u>, Vol. 36, June 1980, pp. 55-70.

57. Enquist, E. and Majda, A., "Absorbing Boundary Conditions for the Numerical Simulation of Waves," Mathematics of Computation, Vol. 31, No. 139, July 1977, pp. 629-651.

58. Thomas, J. L. and Salas, M. D., "Far-Field Boundary Conditions for Transonic Lifting Solutions to the Euler Equations," AIAA Paper 85-0020, January 1985.

59. Roe, P. L., "Remote Boundary Conditions for Unsteady Multidimensional Aerodynamic Computations," ICASE Report 86-75, November 1986.

60. Liepmann, H. W. and Roshko, A., Elements of Gasdynamics, Wiley, New York, 1957.

61. Schmidt, W., and Jameson, A., "Euler Solutions as Limit of Infinite Reynolds Number for Separation Flows and Flows with Vorticies," Lecture Notes in Physics, Vol. 170, Springer-Verlag, New York, 1982.

End of Document